VORTEX LATTICE THEORY: A LINEAR ALGEBRA APPROACH

by

George C. Chamoun

A Dissertation Presented to the
FACULTY OF THE GRADUATE SCHOOL
UNIVERSITY OF SOUTHERN CALIFORNIA
In Partial Fulfillment of the
Requirements for the Degree
DOCTOR OF PHILOSOPHY
(AEROSPACE ENGINEERING)

August 2008

UMI Number: 3325036

INFORMATION TO USERS

The quality of this reproduction is dependent upon the quality of the copy
submitted. Broken or indistinct print, colored or poor quality illustrations and
photographs, print bleed-through, substandard margins, and improper
alignment can adversely affect reproduction.

In the unlikely event that the author did not send a complete manuscript
and there are missing pages, these will be noted. Also, if unauthorized
copyright material had to be removed, a note will indicate the deletion.

UMI®

Dedication

To my parents Chaouki Chamoun, Linda-Rose Myers and Leila Hawi Chamoun.

Acknowledgments

I am grateful and feel fortunate to have had Paul Newton as my advisor, as I have learned from him on both the academic and personal levels. He exudes a positive energy that invigorates scientific research and collaboration, and has been deeply committed to my work and development.

I would also like to thank my co-advisor Eva Kanso for all her academic advice and financial support. Her presence was a motivating factor in taking my research a step further. The lessons I have taken from Paul and Eva will continue to benefit me for life.

In addition, my academic experience has been enriched by several professors. Oussama Safadi has been a mentor to me since the first day I entered USC. Firdaus Udwadia stimulated my interest in dynamical systems. Through Geoffrey Spedding, I learned how to present scientific work in an accessible and concise manner. I would also like to thank my committee members: Igor Kukavica, Fred Browand, Susan Friedlander and Roger Ghanem.

Several graduate students at USC provided me with valuable feedback on my research, and I sincerely thank Fangxu Jing, Babak Oskouei, Korkut Brown and Artan Sheshmani.

I'd like to thank several people that have been a part of my personal life for the past few years and have endured with me the stresses and strains of graduate school: Russell Wald, Sonya Collier, David Crombecque, Valerie Pirktl, Alexandre Cerf, Larry Tsironis and Rachel Elias.

Finally, I would like to thank my parents Chaouki, Linda-Rose and Leila, my grandparents Marvin and Janice, and my sisters Owana, Zara and Oriane for their faith in me and continuous support.

Table of Contents

List of Tables

List of Figures

Abstract

Vortex lattices are prevalent in a large class of physical settings that are characterized by different mathematical models. We present a coherent and generalized Hamiltonian fluid mechanics-based formulation that reduces all vortex lattices into a classic problem in linear algebra for a non-normal matrix A. Via Singular Value Decomposition (SVD), the solution lies in the null space of the matrix (i.e., we require $nullity(A) > 0$) as well as the distribution of its singular values. We demonstrate that this approach provides a good model for various types of vortex lattices, and makes it possible to extract a rich amount of information on them. The contributions of this thesis can be classified into four main points. The first is asymmetric equilibria. A 'Brownian ratchet' construct was used which converged to asymmetric equilibria via a random walk scheme that utilized the smallest singular value of A. Distances between configurations and equilibria were measured using the Frobenius norm $\| \cdot \|_F$ and 2-norm $\| \cdot \|_2$, and conclusions were made on the density of equilibria within the general configuration space. The second contribution used Shannon Entropy, which we interpret as a scalar measure of the robustness, or likelihood of lattices to occur in a physical setting. Third, an analytic model was produced for vortex street patterns on the sphere by using SVD in conjunction with expressions for the center of vorticity vector and angular velocity. Equilibrium curves within the configuration space were presented as a function of the geometry, and pole vortices were shown to have a critical role in the formation and destruction of vortex streets. The fourth contribution entailed a more complete perspective of the streamline topology of vortex streets, linking the bifurcations to critical points on the equilibrium curves.

Chapter 1. Introduction

1.1 Purpose

A vortex lattice is a set of point vortices that are in a state of relative equilibrium. The vortices remain equidistant with time, but the system as a whole can undergo rigid rotations and translations. Vortex lattices have been observed in a variety of physical settings, each characterized by a different mathematical model. These include superconductors ([2], [3], [27]), superfluids ([74]), plasma gases ([23]), milli-sized magnets ([34]), in the wakes of islands ([28]), in geophysical flows ([37], [33], [75], [48], [49], [50], [76]), and in the wakes of other bluff bodies. Vortex lattices observed in nature include highly symmetric ones (in particular: triangular and hexagonal structures ([74], [1])), structures with broken symmetries ([1]), structures that have elastic or periodic inter-vortical dynamics ([17], [25]), and structures that are completely irregular and asymmetric ([26]). Lattices exist throughout a wide range of scales in the physical world including: nano scale (superfluids and superconductors), bacteria scale ([20]), laboratory macro-scale ([18]), planetary scale ([8], [16]), and on the interplanetary scale ([12], [68]). On the sphere, lattices can take the form of periodic vortex streets such as on the surface of Jupiter ([37]). A general coherent theory that describes lattices in all these shapes, sizes and forms does not yet exist, nor does a satisfactory model that describes the formation of irregular patterns. In this thesis, we describe an approach which reduces all of these systems to a classical problem in linear algebra for a non-normal matrix—that of characterizing the null space of the matrix as well as the distribution of singular values. This method opens the door to a series of possible investigations, specifically understanding and controlling properties of the lattices including: the

1

relative vortex strengths, the flow-field's streamline topology, angular & translational velocities, and the *robustness* associated with vortex equilbria.

1.2   Organization

In Chapter **1**, we present the motivation for this thesis. Previous research on vortex lattices will be introduced−with an emphasis on the types of equilibrium geometries found in nature. Numeric and analytic models that have been developed to date will also be mentioned.

The main mathematical techniques used in this thesis are split between Chapters **2** and **3**. In Chapter **2**, a general overview of fluid mechanics is presented that leads to the Hamiltonian point vortex model. The derivations for relative point vortex equilibria on the plane and sphere are presented in this chapter as well. In Chapter **3**, the main tools from linear algebra that are implemented in the analysis are introduced. The first tool is Singular Value Decomposition (SVD), which provides rich geometric information for non-normal matrices, such as the null space and singular values. The next tool is the Shannon Entropy, which provides a scalar measure of a configuration's *robustness*. The third tool is matrix approximation, which is used to measure the *distance* to equilibrium.

Chapters **4**, **5** and **6** contain the results of this thesis, with Chapter **4** addressing configurations on the plane, while Chapters **5** and **6** deal with those on the sphere. The contributions of this thesis can be classified into four main points. First, we present a model that describes the properties and formation of asymmetric vortex equilibria (i.e., lacking any discrete symmetries. See Chapter **4**). Second, we implement 'Shannon Entropy', which we describe in Section **3.2**, and interpret as a scalar measure of disorder, or *likelihood* that a lattice configuration will exist in a physical setting (see Chapters **4**, **5** and **6**). Third, we provide a means of deriving a fully analytic expression for the solution of vortex streets on the sphere (in Chapters **5** and **6**), and highlight the importance of pole vortices in the formation and destruction of the streets. Fourth, we study the streamline topology of vortex streets on the sphere, and propose an analytic way of classifying bifurcations in the topology (in Chapters **5** and **6**).
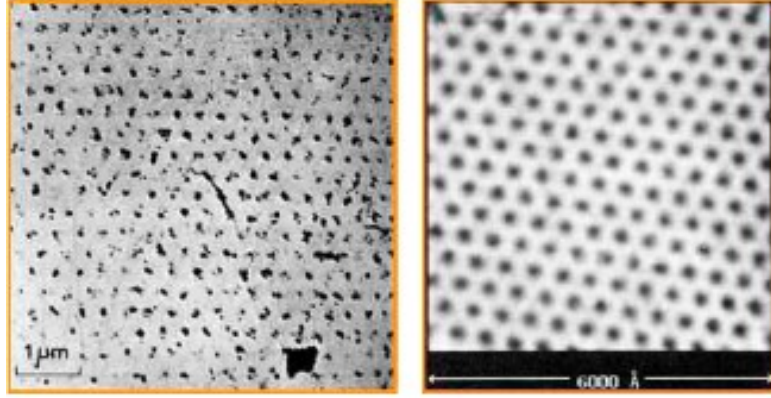
Figure 1.1: Left: the first Abrikosov triangular lattice image by [27], on the order of 1 micron. Black dots represent cylindrical magnetic flux tubes. Right: Image from [36] of an $NbSe_2$ triangular lattice made using scanning-tunneling microscope imaging, showing high degree of symmetry, on the order of several thousand angstroms.
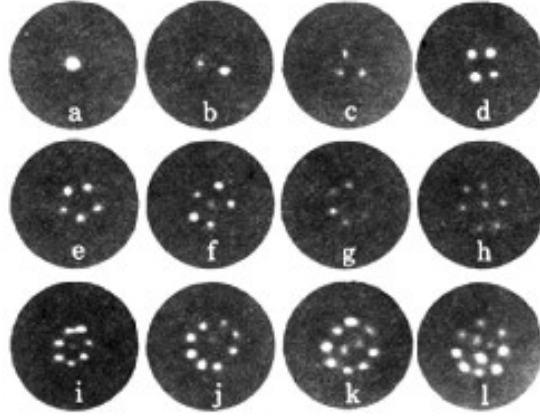
Figure 1.2: Image from [74] of superfluid Helium lattices. Images contain 1-11 equal-circulation vortices, with the vortex number depending on system parameters (rotational speed of capsule, etc.).

In the next section, we will introduce several examples of vortex lattices and highlight their relevance to our work.
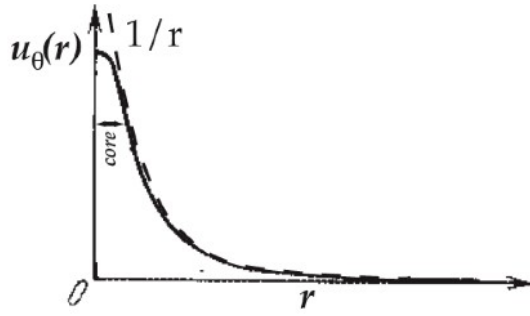
Figure 1.3: Image from Abrikosov's Nobel Prize Lecture ([3]) of velocity vs. distance from vortex center. The solid line represents the velocity flow around an isolated lattice site. The plot's features include a potential vortex core, and constant decay proportional to the distance from the site. The curve-fitted dashed line $1/r$ demonstrates that the point vortex model makes a good fit for sufficiently spaced vortices.

1.3 Vortex Lattices

1.3.1 Symmetric Lattices: Superconductors and Superfluids

We will now outline several lattices that possess a high degree a symmetry. Triangular lattice structures were first predicted to exist by Abrikosov in 1957 (see [2]) during his research on a class of superconductors that are now referred to as type II superconductors. A study of superconductivity, previously published by Ginzburg & Landau ([32]), used a wave-based theory to study phase transitions. An order parameter, now referred to as the Ginzburg-Landau parameter, was used to quantify the phase transitions in which the energy of the fluid became negative. When the parameter reached a critical value, Abrikosov then predicted the formation of quantized periodic arrays consisting of individual cylindrical magnetic flux tubes, and argued that the geometric structure which minimized the free energy should be triangular. The existence of these structures was not taken seriously until 10 years later, when the first image of a superconductor triangular lattice was observed and published by Essmann & Trauble ([27]), see Figure 1.1. The second image in Figure 1.1 from Hess *et al.* ([36]) was made using scanning-tunneling microscope imaging on a much smaller length scale.

Feymann then published a study in 1955 ([29]) on superfluid helium vortex tubes with quantized circulations $\Gamma = \hbar/m \approx 0.001 cm^2/s$, where $\hbar$ is Plank's constant and m is the mass of a
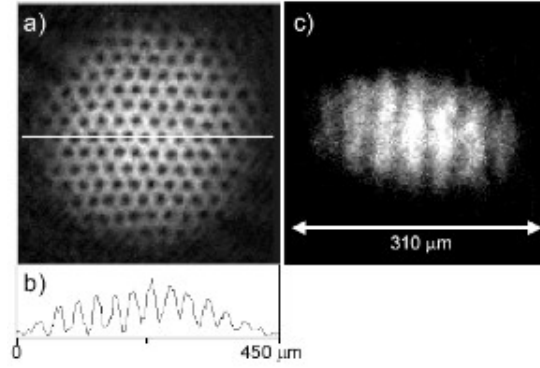
Figure 1.4: Images from [25] showing that lattices possess a nearly two-dimensional structure. (a) is a top view, (b) is cross-sectional intensity reading and (c) is a sideview of the lattice.

[4]He atom. The first good set of images of superfluid Helium lattices obtained by Yarmchuck *et al.* ([74]) is shown in Figure 1.2.

The model used in this thesis is one based on a collection of interacting point vortices. The vorticity at individual lattice sites is localized at a point in $\mathbb{R}^2$, and is purely radial (with no azimuthal component). The 'core size' of a vortex is measured by its visible diameter d (the spots), divided by the intervortical spacing, l. This ratio d/l must be sufficiently small ($\ll 1$). In the lattice structures mentioned, the ratio is on the order of $10^{-2} - 10^{-4}$. Abrikosov's lecture, [3], displayed two important features. First, the vortices have a core region in which the vortex has a flattened maximal strength. Second, the field exhibits a monotonic decay (inversely proportional to the distance from the vortex site), and the velocity tends to zero with increasing distance (see Figure 1.3). Since the vortices are sufficiently spaced, the behavior immediately inside the core is treated as unimportant. Therefore, the flow in an Abrikosov vortex lattice can be approximated quite well with the fluid mechanics model of point vortices presented in Chapter **2**.

1.3.2 Asymmetric Lattices: Bose Einstein Condensates

We now shift our focus to Bose-Einstein condensates, which in recent years have been the subject of intensive focus. The image in Figure 1.4(c) (from [1]) shows that BEC (Bose-Einstein condensates) possess a nearly two-dimensional structure based on the fact that the vortex tubes are
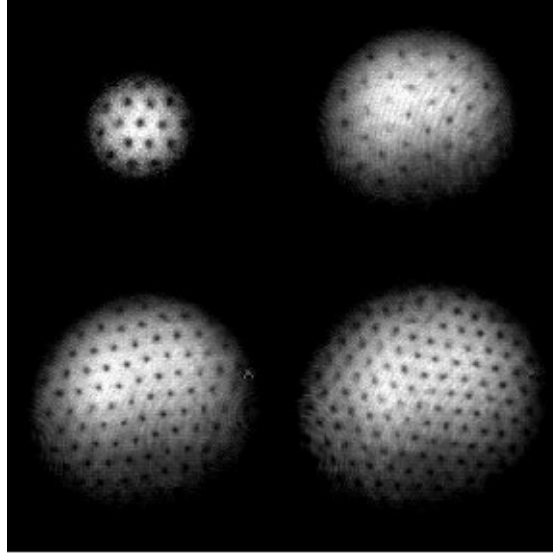
Figure 1.5: Bose Einstein condensate image from [1]. Lattices include 16, 32, 80, 130 vortices, with the vortices being the dark spots.
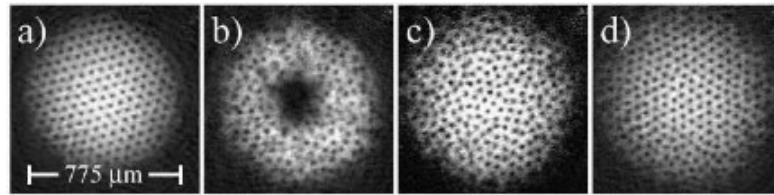
Figure 1.6: Image from [26] of (a) an initially regular triangular lattice, (b) getting blasted by a laser, (c) resulting in a perturbed configuration that undergoes cooling, and the vortices exhibit random motion before (d) the vortices settle into a new irregular equilibrium.

nearly parallel. Figures 1.4 and 1.5 are excellent examples of the kind of imaging now available to study those lattices. The main feature of interest to us in these lattices is that some underlying structures exhibit broken symmetries, or entirely irregular patterns. These findings have exposed the current lack of knowledge on the formation of such configurations or of their robustness, dynamics and stability. Previous analytic and computational work that describes vortex lattice structures focused almost solely on highly symmetric geometries such as those of section **1.3.1**.

An interesting study in which a regular triangle lattice was blasted by a laser demonstrates that completely irregular equilibrium configurations can result—see the work done by Engels *et*
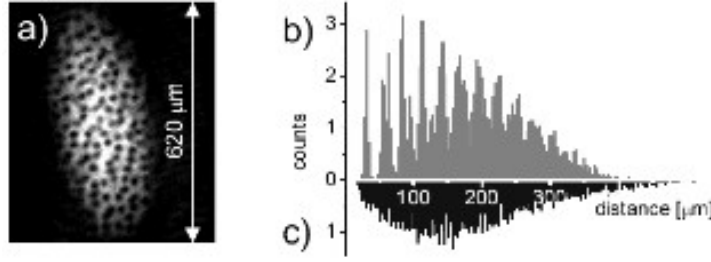
Figure 1.7: Another image from [26] of (a) an asymmetric equilibrium lattice configuration. (b) Cross-section image of vortex intensity; lattice was initially symmetric before being blasted by laser, and settling into a final asymmetric configuration after cooling and random motion had settled. (c) Cross-sectional intensity reading showing the irregular distribution after the 'random' motion has settled.
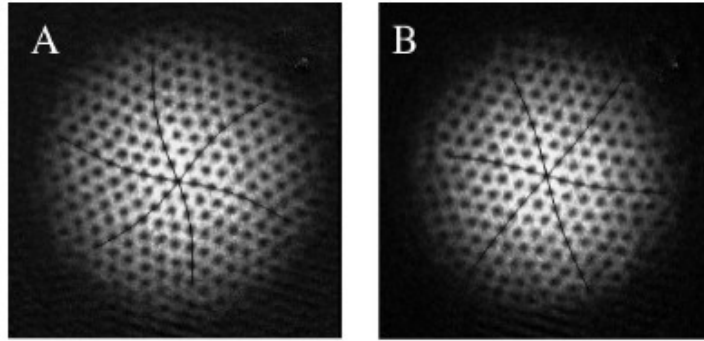
Figure 1.8: Rapidly rotating BEC lattice perturbed by a laser-induced perturbation at the center of the lattice supports small sinusoidal waves referred to '$Tykachenco\ oscillations$' ([17]).

$al.$ ([26]). From Figure 1.6, the vortex lattice begins as a highly symmetric triangular configuration (in subfigure 1.6(a)). The lattice is then blasted by a laser (in 1.6(b)), and appears to follow a random motion after the blast, (in 1.6(c)). As the cooling process takes place, the vortices seem to *thermally fluctuate* towards a final irregular pattern (see Figures 1.6(d) and 1.7). In Chapter **4**, we introduce a Brownian ratchet method ([55]) which uses a random walk algorithm to mimic the process described in Figure 1.6 in order to find asymmetric equilibria.

Two interesting studies have demonstrated shearing effects on lattices. In [25], Engels $et\ al.$ showed that adding external forces to a lattice can change its shape and size (see Figure 1.9). In a related work by Coddington $et\ al.$ ([17]), it was shown that a controlled laser blast to
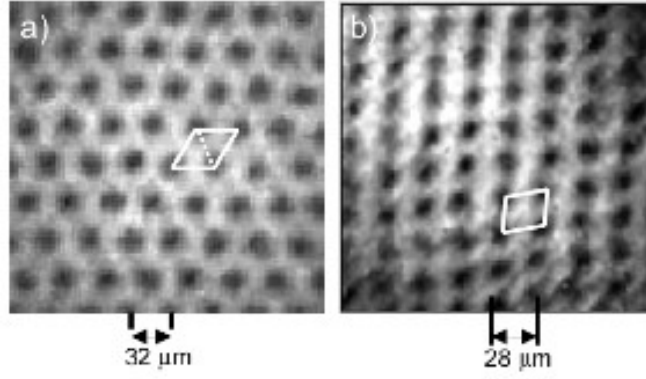
Figure 1.9: Images from [25] showing that external forces on a lattice can change its shape and size.

the center of a rapidly rotating BEC lattice resulted in the removal of an atom from the center of the lattice, which can be interpreted as a change in the *circulation* of the central vortex. This perturbation triggers the propagation of small amplitude sinusoidal waves referred to as 'Tykachenko oscillations' (see Figure 1.8). Tykachenko oscillations appear to have a shearing effect on the angular velocity of the lattice. This phenomenon is explored in Chapter **6**.

In summary, Bose Einstein condensates produce the need for a mathematical model that describes asymmetric lattices in addition to symmetric ones, and one that can analyze shearing effects.

1.3.3 Lattices in Other Physical Systems

Thus far, vortex lattices have solely been referenced in the context of superfluids and superconductors. In this section, we highlight lattices that form in a variety of other physical settings. Grzybowski *et al.* ([34]) demonstrated lattices resulting from millimeter-sized magnetic structures on an air-liquid interface. As shown in Figure 1.10, floating magnetic disks were rotated by a spinning magnet underneath the tank of water, and the disks interacted as particles with fluid ($1/r$ velocity field) and magnetic interactions. Tests were done for a different number of magnets, each of which yielded a symmetric equilibrium configuration. Some of the systems have two resultant equilibrium configurations for a given number of magnets between which

8
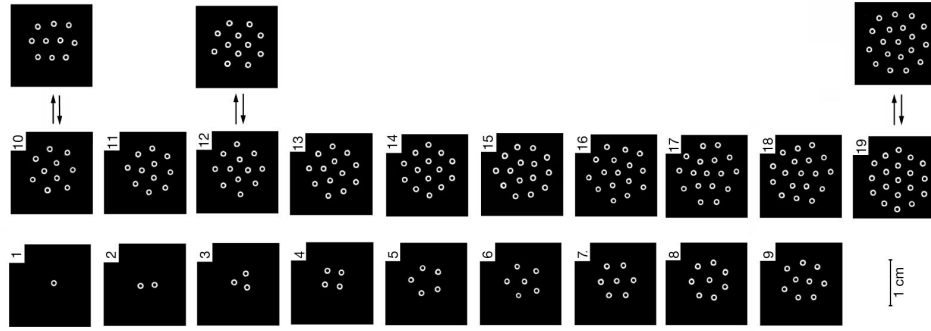
Figure 1.10: Milli-sized magnetic structures floating on a rotating fluid. Magnets form lattice-like structures. Images above are for different numbers of magnets, from [34].
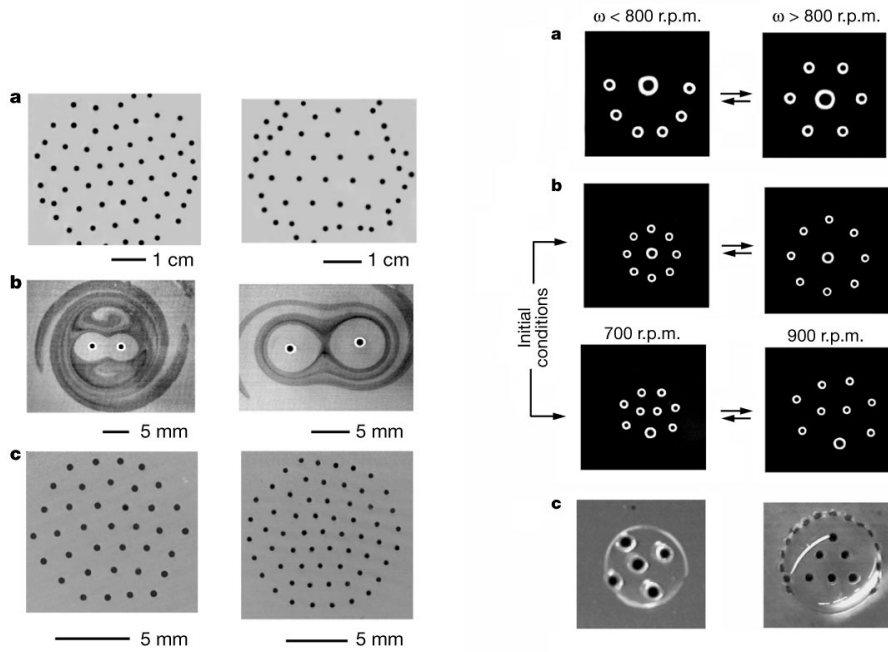
(a) Fluid Dye demonstrates rotation about magnets

(b) Variable-sized magnets and surfaces

Figure 1.11: Left, (a): magnets far from center of rotation possess asymmetric structure; and dye injected into fluid shows that magnets are themselves rotating, and form a prototype of point vortex equilibria. Right, (b): Subplots **a**, **b**: Lattices formed by variable-sized lattices. Interchangeable arrows indicate that system switches between the two configurations. Subplot **c**: Lattices formed on the curved surface of a drop. These configuration types never formed on the flat water-air interface. Images from [34].
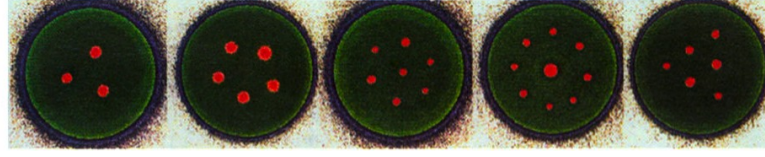
Figure 1.12: Trapped plasma in a cylindrical structure with a spiral electron source. Vortex lattice tubes form with different vortex numbers and configurations. Image from [30].
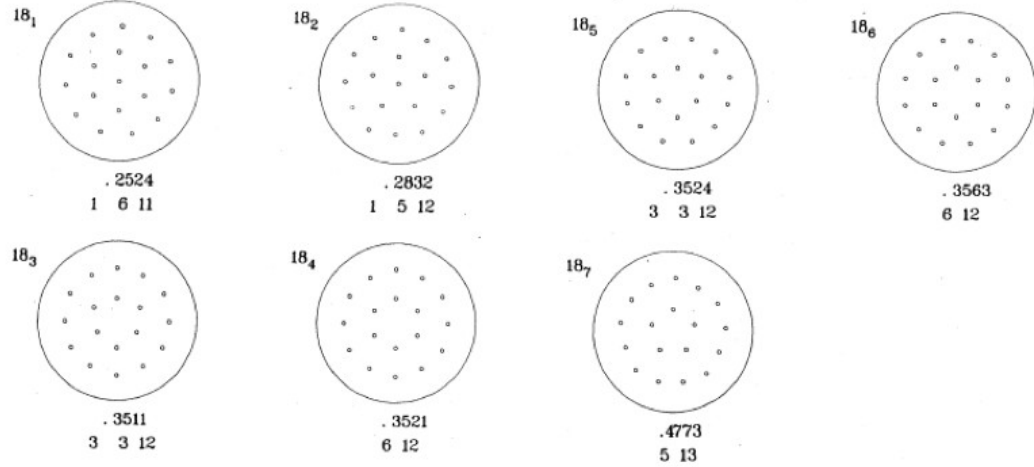
Figure 1.13: An image from the Los Alamos 2-dimensional vortex lattice catalogue of [14]. $N = 18$ vortices for all the configurations above, energies and vortex strengths are labeled below with the first (1 6 11) having the lowest energy.

the system sporadically switched. Tests were also done with different-sized magnets, which can be interpreted as point vortices with different relative strengths. Figure 1.11(a) shows that the magnets themselves rotated since the dye injected into the fluid was advected around the magnets in a manner consistent with the streamline topology of point vortices ([53]). Figure 1.11(b) demonstrated two things. First, equilibria from different-sized magnets were investigated, and in the context of vortices, the size of the magnets can be interpreted as the strength of their circulation. Second, equilibria on the non-flat surface of a drop demonstrated that different equilibrium geometries can result on different-shaped surfaces. In a study from a different physical setting, vortex lattice formation in a confined cylindrical plasma tube (see Figure 1.12) was published by

Fine *et al.* in [30]. Again, depending on system parameters, different lattice patterns emerge. In the case of a central vortex, it occasionally had a larger diameter than the outer vortices.

Campbell & Ziff ([14]) compiled the Los Alamos catalogue of equilibria for systems of equal strength vortices made up of circular, concentric vortex patterns along with their properties, particularly the Hamiltonian energy. They showed that for the same number of vortices, there exist multiple equilibria, each of which generally has a different energy. The symmetric lattices in [14] can be found with classic gradient methods since the energy landscape associated with such structured configurations is generally not complex. But for large numbers of vortices ($N > 100$) or for asymmetric equilibria, classical gradients techniques become inconvenient since their associated energy landscapes are far more complex. Thus, the works cited in this section illustrate that vortex lattices exist in a variety of physical settings. Note that in [14], it was illustrated that more than one geometry is possible for the same number of vortices. Furthermore, certain geometry types appear to be more prevalent than others on a given surface. In the next section of this chapter, we move our discussion to vortex streets, which are an important kind of vortex lattice that are prevalent in a variety of physical settings.
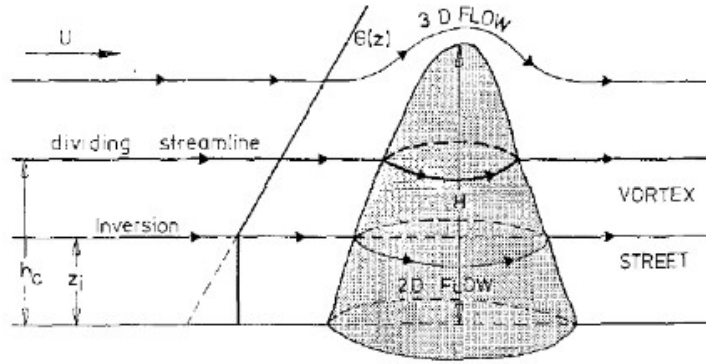
Figure 1.14: Side view schematic of vortex wake formation. The critical height, h_c, above which air passes over island, and below which the flow separates around the island and forms the vortex street. Image from [28].

1.4 Von Kármán Vortex Streets

The motivation for studying vortex streets is because of their presence in the physical world, their role in geophysical climates, and their possible usefulness in engineering applications. On the plane, idealized vortex streets are thought of as two infinite lines of evenly spaced vortices, where one line is shifted by a half-wavelength (skewed). The vortices in each line are equal in strength and opposite to those in the other line. Thus, the full system of $N = 2n$ vortices has vanishing circulation. Generally, they exist in nature as a dissipative set of vortices that remain in approximate relative equilibrium for a finite period of time. On the sphere, a street is formed by a closed set of two parallel skewed rings—with each ring having an equal number of vortices (see Figure 1.16 from [49]). The following section summarizes the most common physical settings in which vortex streets exist.

1.4.1 Where They Exist

One place where vortex streets form is in the wake of bluff bodies due to the viscous boundary layer—a process that is well understood. In Figure 1.14 (from [28]), the island is modeled as a conic-shaped body. Above a critical altitude, the flow simply rises above the island and passes over it without separation or the formation of eddies. Below this altitude, the flow separates
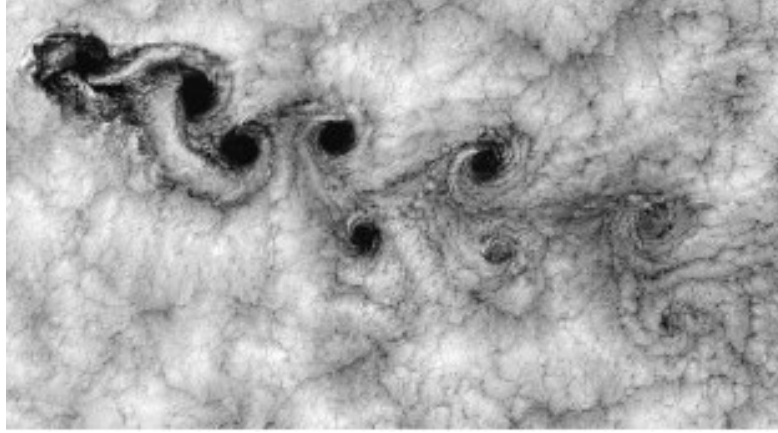
Figure 1.15: Juan Fernandez islands off the coast of Chile. Island's geophysical wake forms a vortex street.

and goes around the island. Behind the island, the separated flow does not reconnect, and it is in this region that the vortex street is formed. See Figure 1.15 for a satellite image of a vortex street in the wake of an island. The wake as a function of the Reynolds number is a well-studied problem−for a thorough overview see [72]. Vortex shedding only commences when the Reynolds number $Re > 45$, and there are three different *shedding regimes*, characterized by different shedding frequencies, see [65] for a thorough empirical analysis of this problem. For a rationale of the relation between the Reynolds number and shedding frequency, see [62].

Vortex streets also affect aquatic life, and a recent study by Liao *et al.* ([47]) showed its potential usefulness by fish swimming in a stream. The study showed that the trout swimming in the wake of the cylinder (and interacting with a vortex street) modified their body motion, and that they used less locomotive energy than did the fish swimming in the free-stream. Therefore, fish can benefit from the presence of vortices in their ambient fluid. In the context of point vortex lattices, the methods described in Chapters **2** and **3** are applicable to point vortex equilibria in the absence of solid bodies. If one wishes to solve for lattices that contain solid bodies (such as a fish), it would be possible to expand the techniques in those chapters by using the method of images.

In this thesis, we will be addressing vortex streets that appear in geophysical flows in the complete absence of bluff bodies, as is the case with Jupiter (see Figure 1.16). According to
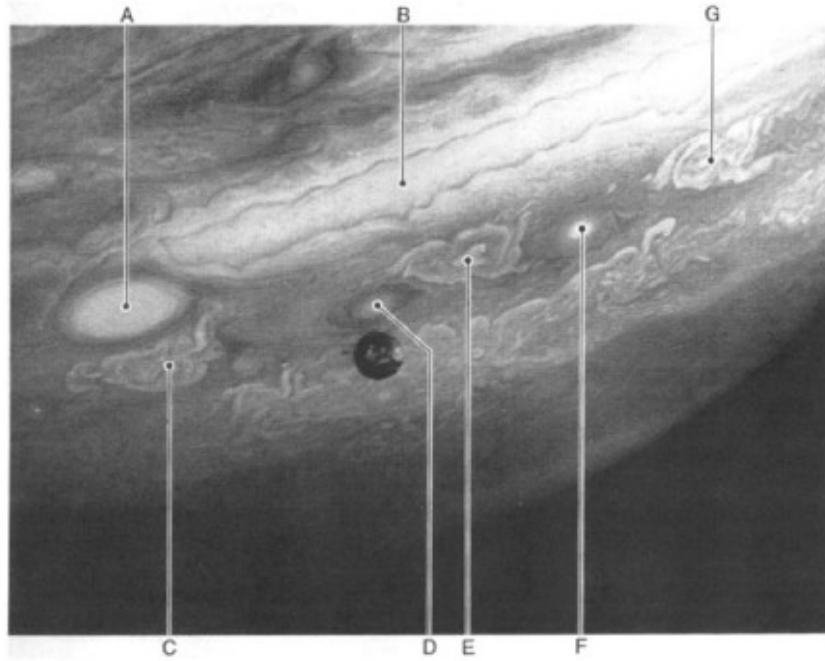
Figure 1.16: Vortex street on Jupiter. Points labeled C, E and G are cyclones while points D and F are anti-cyclones. These are part of a set of twelve cyclones coupled with twelve staggered anti-cyclones forming a loop about Jupiter. Image from [49].

Humphreys & Marcus ([37]), a very clear vortex street that wraps around Jupiter was first formed around the year 1939, remained steady until around 1998, at which point it began to disintegrate. In the Jovian atmosphere, the full atmospheric layer consists of 12 major zonal jet streams and an additional 80 easily visible vortices, with the largest of these being the well-known Great Red Spot [48]. The physical mechanisms and processes which set the scale for the spacing and core size of vortex streets are less understood. The topic of 'pattern formation' is addressed in [37]. In Chapters **5** and **6**, we propose that Shannon Entropy (defined in Section **3.2**) can be used as a means to predict what street parameters are most likely (i.e, number of vortices per street, angle between the streets' rings).

(a) Symmetric   (b) Staggered
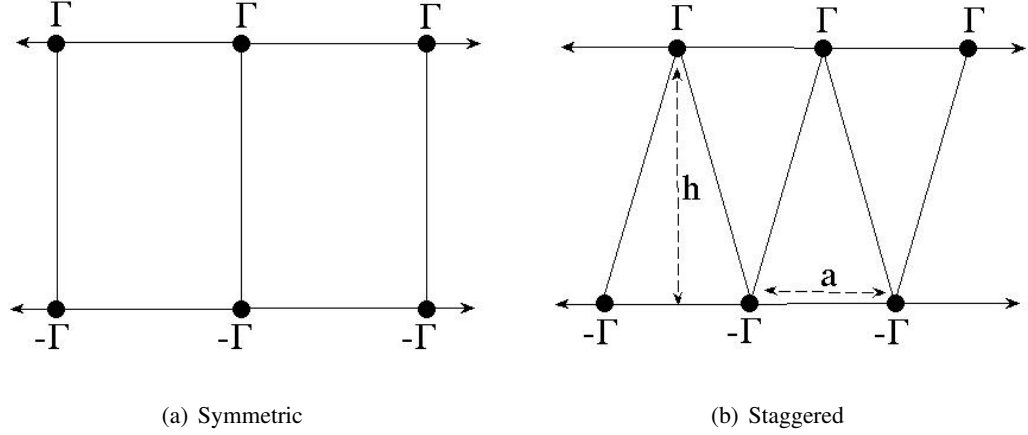
Figure 1.17: Symmetric and Staggered configurations for a vortex street with two vortices per periodic strip. Definition of vortex spacing for a staggered von Kármán street is present in (b).

1.4.2 History of the Vortex Street Model

The first known result that described a vortex street appeared in 1928 ([31]). The authors' result was that the constant velocity of N repeating vortices is given by

$$\dot{z_\alpha}^* = U - iV = \frac{1}{2Li} \sum_{\beta=1}^{N} \Gamma_\beta \cot(\frac{\pi}{L}(z_\alpha - z_\beta)), \tag{1.1}$$

where U, V are the Cartesian velocity components of the system, Γ_β is the strength of the βth vortex, L is the width of the periodic strip, N is the number of vortices in the periodic strip, and $z_\beta = x_\beta + iy_\beta$ is the complex coordinate of vortex β (see [45] for a comprehensive overview of von Kármán's work). Von Kármán used this idea for a strip with $N = 2$ and with the strengths of the two vortices being $\Gamma_1 = -\Gamma_2 = \Gamma$. The street then propagates with velocity

$$U - iV = \frac{-\Gamma}{2Li} \cot(\frac{\pi}{L}(z_+ - z_-)), \tag{1.2}$$

where z_+ and z_- are the complex locations of any two vortices in the same period. For a street that moves along the real axis, $V = 0$, which implies that the cotangent portion of Equation (1.2)

15

must be purely imaginary. For this condition, the requirement is that $\mathbb{R}(z_+ - z_-) = 0$ or $L/2$, which corresponds to symmetric and staggered configurations respectively (see Figure 1.17).

Von Kármán then performed a linear stability analysis on the streets. He did so by perturbing the position of one vortex. The result was that the symmetric configuration was always linearly unstable, and that the staggered configuration was linearly stable for a specific ratio of the spacing for the two vortices in each strip, namely that

$$\sinh \frac{\pi a}{h} = 1, \tag{1.3}$$

where a and h are defined in Figure 1.17(b). Domm went on to show that even streets satisfying this special aspect ratio failed the stability test in second order perturbation theory ([21]). Although this thesis will not be addressing the issue of stability of either vortex streets or of vortex lattices, we will direct the reader in the next paragraph to several references that do.

Both linear and non-linear studies have been made for evenly distributed vortex cores in rectilinear planar settings (see [66]). This problem is reasonably well understood and used as a basis to predict the persistence and lifetimes of vortex streets found in physical systems. The stability of more general point vortex configurations on the sphere is not a very well studied or understood problem, but there is presently a small body of work available on the subject. One study can be found in Laurent-Polz *et al.* ([46]). Pekarsky & Marsden ([61]) studied the nonlinear stability of three point vortices on the sphere by considering the momentum map (i.e., center of vorticity vector in Equation (2.53)), and referred to their technique as the energy-momentum method. Studies on the nonlinear stability of N evenly distributed point vortices on the same latitude can be found in the works of [13], [10] and [44].

1.4.3 Bifurcation Problems and Streamline Topology

The observed vortex street patterns on Jupiter have had long, but finite lifetimes, and their presence affects the overall mixing regimes on the planet and its climate. Therefore, it is fundamentally important to understand how fluid transport changes with the vortex configuration, and

Figure 1.18: An exotic wake with one singlet (S) and one pair (P) per periodic strip, denoted '$S + P$', from [73].

the associated bifurcations. The techniques presented in Chapters **2** and **3** make it possible to thoroughly and analytically investigate bifurcations in the vortex strengths and streamline topology when smoothly varying a parameter linked with the geometry of the lattice. This analysis is fleshed out in Chapters **5** and **6** in the context of vortex streets on the sphere. In this section, we will reference some of the work that has analyzed bifurcations in the street geometry and streamline topology. The references will include both streets formed in the wake of a bluff body, and streets in the absence of a bluff body. Although our work deals exclusively with vortex equilibria formed in the absence of solid bodies, we reference bluff body wakes in order to fully understand the mechanisms creating vortex streets. Furthermore, we focus on the geometry of the street itself, and ignore the presence of the bluff body by confining our analysis to the vortex street pattern that lies sufficiently far from the bluff body.

Computational models of different shedding regimes in the wake behind a stationary cylinder can be found in the works of [38], [64], [77], [24], [58], [59], and most recently by [11]. Vortex shedding also takes place behind non-stationary bluff bodies. When the cylinder in the flow is allowed to oscillate, an "exotic" wake results, which consists of both single shed vortices 'S'−also referred to as singlets, and vortex pairs 'P'. For instance, in Figure 1.18, the wake is labeled '$S + P$', for one singlet and one doublet. The wake is affected by two parameters: the amplitude (normal to the free stream) and wavelength of oscillation, with the wavelength compensating for both the frequency of oscillation and the free stream velocity. For an empirical
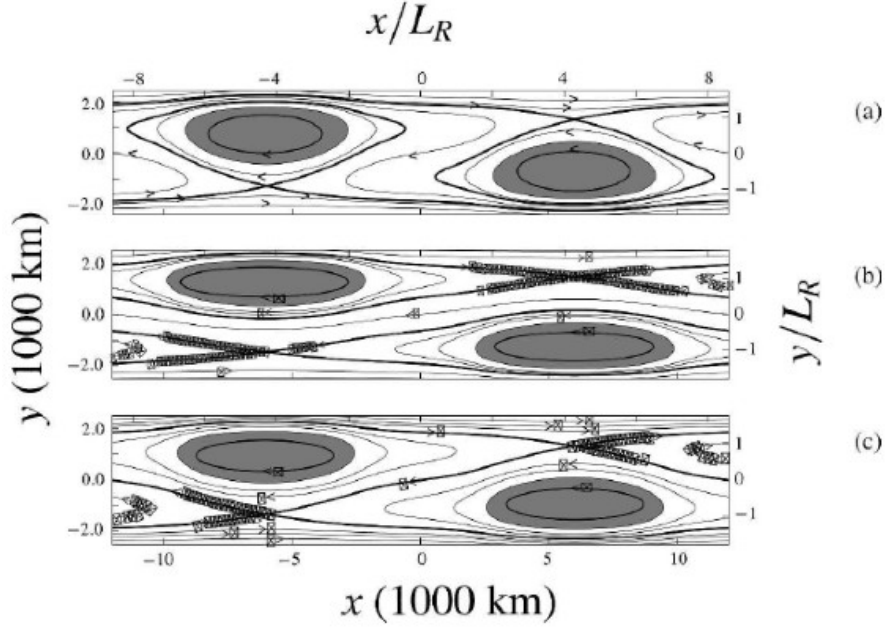
Figure 1.19: Three different streamline topology types for Jovian vortex streets (JVS) on the sphere identified in [37], labeled as (a) Type I, (b) Type II, and (c) Type III. In Type III, the sets of separatrices collapse, which entails that the region of flow that travels across the street disappears. Different types correspond to different parameter values.

study of all the different possible exotic wakes, see [73]. In [63], a rationale for how the exotic wake changes with the parameters of oscillation was formulated.

In Chapters **5** and **6**, two sets of analytic *equilibrium curves* for vortex streets on the sphere that undergo bifurcations are derived. The first set (Figures 6.52, 6.57) illustrates the relative vortex strengths of the streets' vortices as a function of the vortex street's geometry (i.e., angle between the rings, or number of vortices per ring). The second set (Figures 5.45, 6.53) represents the rigid rotational velocity as a function of its geometry. The analogy is made to the bifurcations encountered in the aforementioned experiments of this section, in which shedding regimes (or street geometries) encounter bifurcations and change with the system parameters—just as the exotic wake changes with the parameters of oscillation (Figure 1.18).

Next, we consider bifurcations in the streamline topology of vortex streets. In Figure 1.19 from [37], three different topology types for a vortex street are identified and labeled, each corresponding to different parameters. In our work (see Figures 5.46, 6.56 and 6.58), we identify
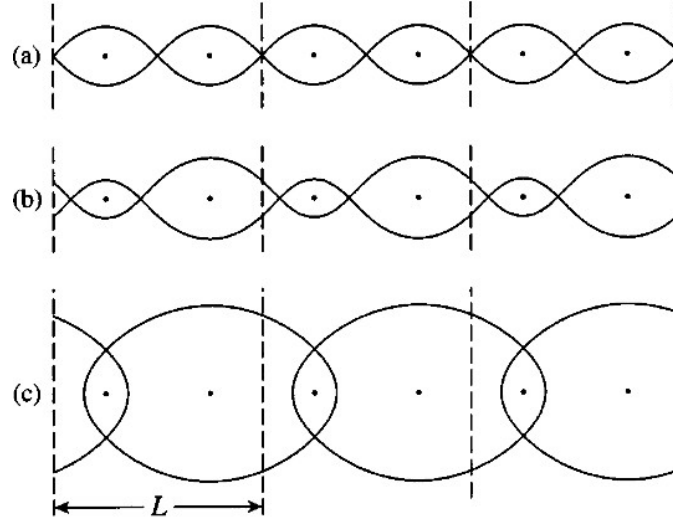
Figure 1.20: Streamline topology for 2 vortices per periodic strip and velocity $V = 0$ (see Equation (1.1)). The images are for the strength ratios (a) 1:1 (b) 1:3 (c) (-1):3, from [69].

a broader class of topology types corresponding to single and double vortex streets on the sphere, and note that any two topology types are separated by a bifurcation topology point. In addition, we show that the topology type in Figure 1.19(c) corresponds only to a bifurcation point within the configuration space, and not to that of a range of parameters. In a second relevant study for inviscid point vortex streets by Stremler ([69]), the streamlines of vortex streets on the plane containing 2 and 3 vortices per periodic strip are studied. Using Equation (1.1) for N repeated vortices per strip, and multiplying both sides by Γ_α, the author derives

$$\frac{1}{2Li} \sum_{\beta=1}^{N} \Gamma_\alpha \Gamma_\beta \cot\left(\frac{\pi}{L}(z_\alpha - z_\beta)\right) = SV^* = 0, \tag{1.4}$$

where

$$S = \sum_{\alpha=1}^{N} \Gamma_\alpha. \tag{1.5}$$

Therefore, the vortex street is in equilibrium (i.e., all vortices remain equidistant) if either $V = 0$ (the street has no velocity) or $S = 0$ (the strengths of the vortices in each street sum to zero). Revisiting von Kármán's configuration for the case of two vortices per periodic strip ($N = 2$):

19
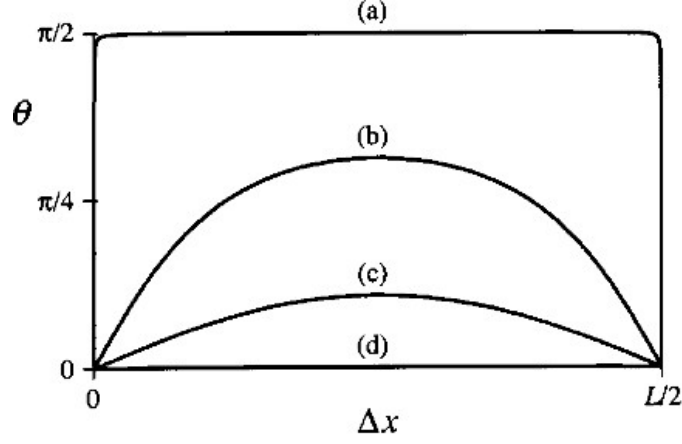
Figure 1.21: Propagation angle θ vs. horizontal spacing (see Equation (1.6)) for (a) $\Delta y = L/10,000$, (b) $\Delta y = L/10$, (c) $\Delta y = L \sinh^{-1}(1/\pi)$ and (d) $\Delta y = L$. From [69].

if $V = 0$ and for any S, the cotangent must be zero which requires that all vortices are collinear on the real line (see Figure 1.20). For the case $S = 0$, this implies that the two vortices have equal and opposite strength (i.e., $\Gamma_1 = -\Gamma_2 = \Gamma$). For this case, any choice of vortex positions results in an equilibrium configuration that is translating with a constant velocity. The angle of propagation of the street (from the real axis) is determined from the ratio

$$\mathbb{R}(V) = \sinh\left(\frac{2\pi \Delta y}{L}\right), \quad \mathbb{I}(V) = \sin\left(\frac{2\pi \Delta x}{L}\right), \tag{1.6}$$

where Δx and Δy are the Cartesian distances between the two vortices in each periodic strip. Off-axis propagation occurs unless the spacing $\Delta x = 0$ or $L/2$. Figure 1.21 illustrates the propagation angle as a function of vortex spacing. Furthermore, from [51], the vortex street is linearly stable if it satisfies the criterion

$$\sinh\left(\frac{2\pi \Delta y}{L}\right) = \sin\left(\frac{2\pi \Delta x}{L}\right). \tag{1.7}$$

An interesting observation for the case of two vortices per strip is the existence of heteroclinic orbits that connect different stagnation points. In Figure 1.22, two such configurations are presented. In the first, a heteroclinic orbit connects stagnation points from two adjacent periodic

20
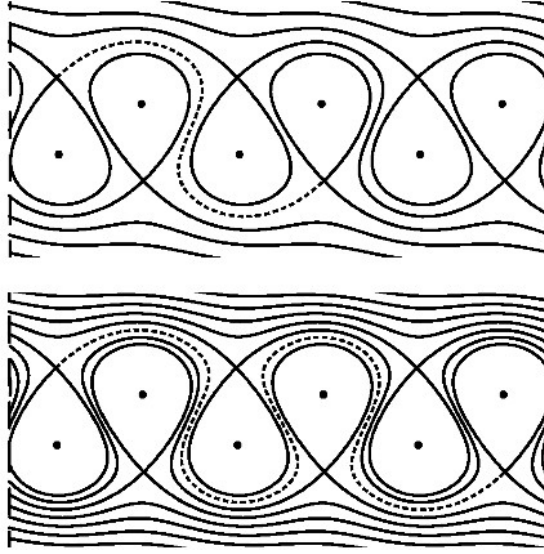
Figure 1.22: Heteroclinic orbits are presented as dashed lines, vortex streets with two opposite-strength vortices per strip. Upper subplot has $n = 1$, lower has $n = 2$, where n denotes how many strips are passed with each heteroclinic connection. From [69].
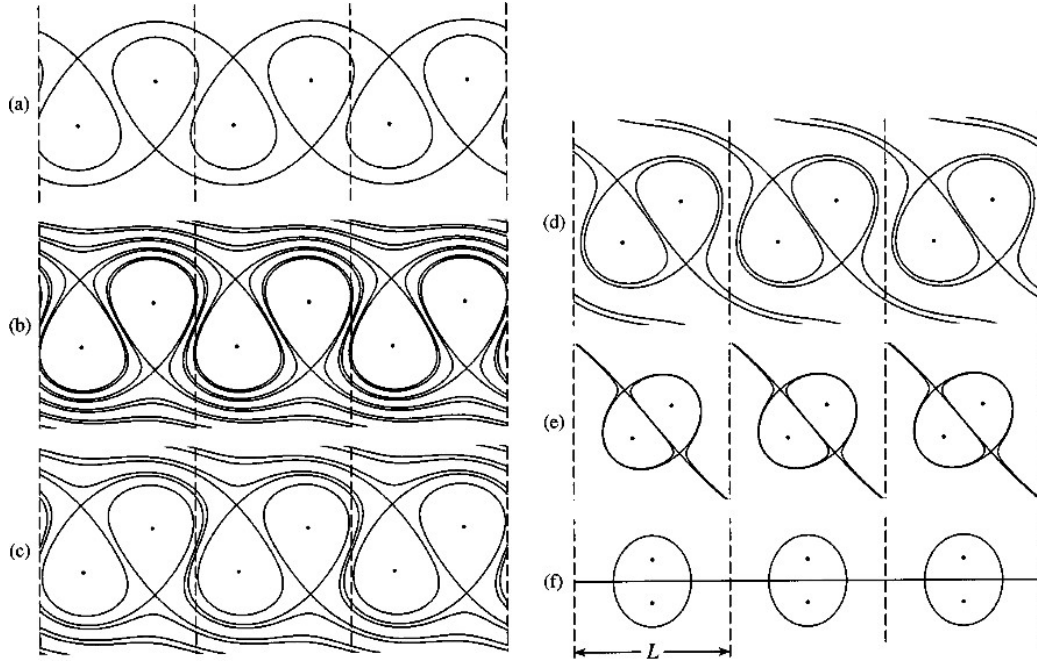
Figure 1.23: Streamline topology for two vortices per periodic strip, and with $\Gamma_1 = \Gamma_2 = \Gamma$. Configurations (a) - (e) are linearly stable. Δy is determined for (a) $\Delta x = L/2$, (b) $\Delta x = 6L/13$, (c) $\Delta x = 4L/9$, (d) $\Delta x = 3L/8$, (e) $\Delta x = L/4$ and (f) $\Delta x = 0$ with $\Delta y = \sinh^{-1}(1/\pi)$, from [69].
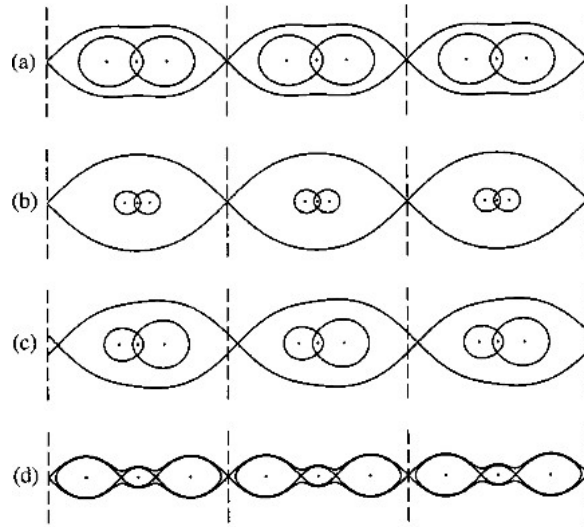
Figure 1.24: Three vortex streets per period with $V = 0$ and $G > 0$. The vortex strengths of the above configurations are (a) 3:(-1):3, (b) (21/10):(-1):(21/10), (c) 2:(-1):3 and (d) 3:1:3. Image from [69].
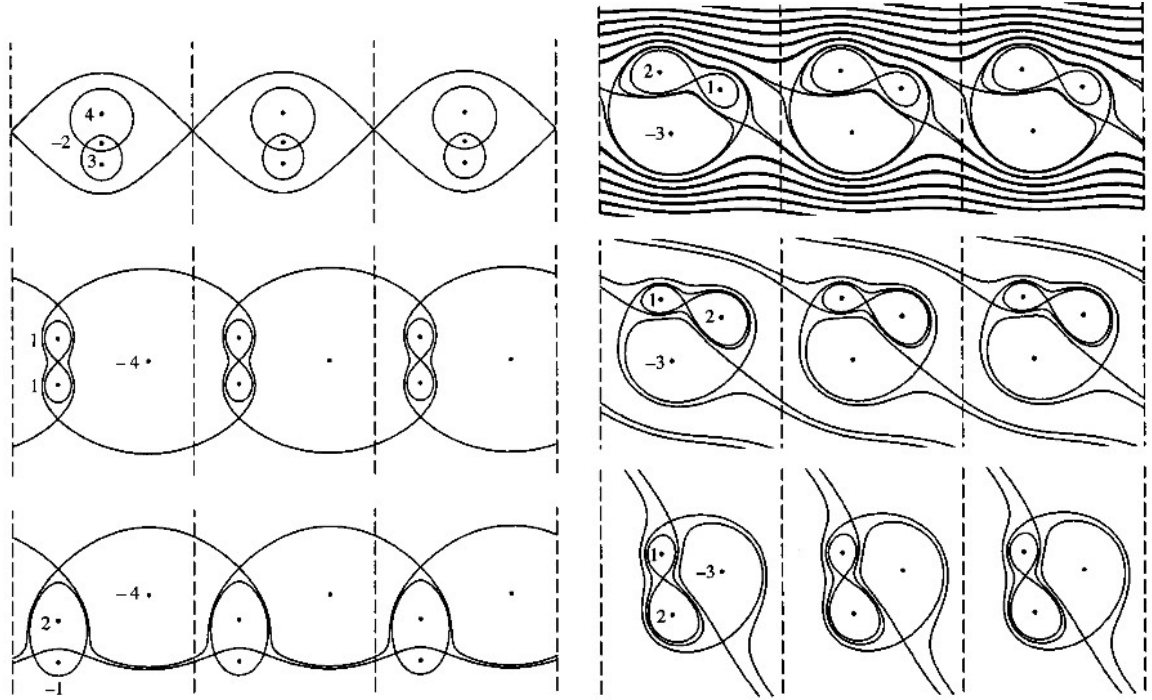
Figure 1.25: Left: Vortex positions and streamlines for three vortices with $V = 0$ and $G < 0$. Images above correspond to (from top to bottom) (a) $\Gamma_j{}^2 > |G| = 2$, (b) $\Gamma_1{}^2 = 1 < |G| = 7$, (c) $\Gamma_1{}^2 = 1 < |G| = 6$. Right: Three vortices per strip with $S = 0$, configurations have the strength ratio 1:2:(-3). From [69].

strips, and this configuration is denoted $n = 1$. In the lower subplot, a heteroclinic orbit connects stagnation points from two periodic strips that are two strips apart (i.e., separated by a single strip), and this configuration is denoted as $n = 2$. Heteroclinic orbits have interesting implications for mixing. Fluid in these configurations passes from above the street, swirls through it and exits below. As n increases, less fluid passes through the street until finally, when $n \equiv \infty$, no fluid passes through the street at all, and the configuration for $n \equiv \infty$ can be found in Figure 1.23(a).

For the case of three repeated vortices per periodic strip, a similar analysis was conducted, and highlights of the results will be mentioned here. An important quantity for these configurations is the geometric strength sum

$$G = \Gamma_1\Gamma_2 + \Gamma_2\Gamma_3 + \Gamma_1\Gamma_3. \tag{1.8}$$

For the static case $V = 0$, if $G > 0$, all three vortices lie on the real line, and the relative positions depend on the vortex strengths (see Figure 1.24). If $V = 0$ and $G < 0$, either all three vortices lie on a vertical line if $\Gamma_\alpha{}^2 > |G|$, or two lie on a vertical line while the third satisfies the condition $\Gamma_\alpha{}^2 > |G|$ and is offset by $L/2$ (see Figure 1.25). In the second case when $S = 0$ (i.e., $\Gamma_1 + \Gamma_2 + \Gamma_3 = 0$), two of the vortex positions can be chosen arbitrarily while the third is determined analytically (Figure 1.25). Furthermore, these configurations will, in general, translate with a constant speed V. Configurations can be chosen to have a particular speed.

To summarize, the works that have been referenced in this chapter presented several important features that describe vortex lattices: prevalent configuration geometry types, relative vortex strengths, and bifurcations−specifically within the streamline topology. The methods (Chapters **2** & **3**) and results (Chapters **4**, **5** & **6**) presented in the remainder of this thesis provide a thorough, and unified approach to the aforementioned problems referenced in this chapter.

Chapter 2. Fluid Mechanics Formulation

In this chapter, we detail all the required mathematical background that leads to the point vortex model. We begin by introducing the Navier-Stokes equation which is the most general formulation in fluid mechanics, given by

$$\frac{D\mathbf{u}}{Dt} \equiv \mathbf{u}_t + \mathbf{u} \cdot \nabla\mathbf{u} = -\nabla p + \mathbf{f} + \frac{\mu}{\rho}\nabla^2\mathbf{u}, \tag{2.9}$$

where $\mathbf{u}$ is the velocity field. $D(\cdot)/Dt = \partial(\cdot)/\partial t + (\cdot, \nabla\cdot)$ is the absolute derivative with respect to time, $\mathbf{f}$ is a set of conservative external forces, μ is the viscosity of the fluid, and ρ its density. In our work, we will be dealing exclusively with inviscid (i.e., $\mu = 0$), incompressible fluid. The condition for incompressibility is characterized by

$$\nabla \cdot \mathbf{u} = 0, \tag{2.10}$$

and this is referred to as the *continuity equation* for an incompressible fluid. The properties for this class of fluids will be expanded in the following section.

2.5   General Properties of Inviscid, Incompressible Flows

The balance of linear momentum of an inviscid, incompressible fluid acted upon by conservative forces is given by the Euler equation

$$\frac{D\mathbf{u}}{Dt} \equiv \mathbf{u}_t + \mathbf{u} \cdot \nabla \mathbf{u} = -\nabla p + \mathbf{f}, \tag{2.11}$$

where the fluid density ρ is normalized to one. The *vorticity field* $\omega \in \mathbb{R}^3$ associated with a velocity field $\mathbf{u} \in \mathbb{R}^3$ is defined as

$$\omega = \nabla \times \mathbf{u}. \tag{2.12}$$

Substituting Equation (2.12) into (2.11) gives the vorticity equation

$$\frac{D\omega}{Dt} \equiv \omega_t + \omega \cdot \nabla \omega = \omega \cdot \nabla \mathbf{u}. \tag{2.13}$$

The fluid is said to be irrotational if ω is zero. Taking the dot product and curl of Equation (2.12), yields respectively

$$\nabla \cdot \omega = \nabla \cdot (\nabla \times \mathbf{u}) = 0, \tag{2.14}$$

$$\nabla \times \omega = \nabla \times (\nabla \times \mathbf{u}) = -\nabla^2(\mathbf{u}). \tag{2.15}$$

Using Stokes' theorem and integrating the divergence of the vorticity in a finite volume gives

$$\int_V \nabla \cdot \omega \, dV = \int_S \omega \cdot \mathbf{n} \, dS = 0, \tag{2.16}$$

where S is a closed surface with normal vector $\mathbf{n}$ bounding a volume V of fluid with vorticity field ω. This relation tells us that flux of the vorticity across S is zero. The same conclusion can be made regarding the flux of the velocity.

2.5.1 Hodge Decomposition

The velocity field can be decomposed into a superposition of translational and rotational motion components using Helmholtz, or *Hodge Decomposition*, and this is given by

$$\mathbf{u} = \mathbf{u}_\phi + \mathbf{u}_\omega = \nabla\phi + \nabla \times \psi. \tag{2.17}$$

If a fluid is irrotational (i.e., $\nabla \times \mathbf{u} = 0$), the fluid velocity is given solely by $\mathbf{u} \equiv \mathbf{u}_\phi$ and can be derived from the gradient of a scalar field ϕ. Since our velocity field is divergence free, it follows that ϕ satisfies Laplace's equation: $\nabla^2\phi = 0$. If we have a rotational component to the velocity field, we define this as $\mathbf{u}_\omega$, which can be derived from the curl of a vector field ψ. It follows from Equation (2.12) for ψ of Equation (2.17) that the vorticity scalar field is given by the Poisson equation

$$\nabla^2\psi = -\omega. \tag{2.18}$$

A standard solution ([19]) to this Poisson equation in terms of the Green's function for the Laplacian is

$$\psi(\mathbf{x}) = \int G(\mathbf{x} - \mathbf{z})\omega(\mathbf{z})d\mathbf{z}, \tag{2.19}$$

where

$$G(\mathbf{x}) = \begin{cases} -\frac{1}{2\pi}\log\|x\|, & \mathbf{x} \in \mathbb{R}^2 \\ \\ \frac{1}{4\pi}\frac{1}{\|x\|}, & \mathbf{x} \in \mathbb{R}^3 \end{cases}, \tag{2.20}$$

with

$$\nabla^2 G(\mathbf{x}) + \delta(\mathbf{x}) = 0. \tag{2.21}$$

Finally, since $\mathbf{u}_\omega = \nabla \times \psi$, we can substitute into Equation (2.19) to get

$$\begin{aligned} \mathbf{u}_\omega &= \nabla \times \int G(\mathbf{x} - \mathbf{z})\omega(\mathbf{z})d\mathbf{z} \tag{2.22} \\ &= \int K(\mathbf{x} - \mathbf{z})\omega(\mathbf{z})d\mathbf{z}, \tag{2.23} \end{aligned}$$

where K is the singular Biot-Savart kernel defined for $2D$ and $3D$ as

$$K(\mathbf{x}) = \begin{cases} +\frac{1}{2\pi}\frac{1}{\|x\|^2}\begin{pmatrix} -y & x \end{pmatrix}, & \mathbf{x} \in \mathbb{R}^2 \\ \\ \frac{1}{4\pi}\frac{1}{\|x\|^3}\begin{pmatrix} 0 & z & -y \\ -z & 0 & x \\ y & -x & 0 \end{pmatrix}, & \mathbf{x} \in \mathbb{R}^3 \end{cases}. \tag{2.24}$$

2.5.2 Circulation

A fundamental quantity associated with vorticity (and with the point vortex model in the next section) is *circulation*, given by the scalar via Stokes' theorem

$$\Gamma = \oint_C \mathbf{u} \cdot d\mathbf{s} = \int_A \nabla \times \mathbf{u} \cdot \mathbf{n}dS = \int_A \omega \cdot \mathbf{n}dS. \tag{2.25}$$

C is a curve that encloses a surface A. In an ideal, incompressible fluid, the circulation of a body of fluid bounded by its moving material boundary $C(t)$ remains constant (i.e., $d\Gamma/dt = 0 \implies \Gamma(t) = \Gamma_0$). Equation (2.25) can be used to prove that for a point vortex, the circulation is located at a single point (i.e., the vortex site), and remains unchanged for any selection of C or A for the integral in Equation (2.25).

2.5.3 Application of the Cauchy-Riemann Equations

The final definition we will reference is the general Cauchy-Riemann identity for analytic functions ([53]), and we will demonstrate its usefulness in the context of the point vortex model in the following section.

Definition 1. *The complex analytic function*

$$w(z) = \phi + i\psi$$

*is called the **complex potential** for the flow, where $z = x + iy$. The real part, ϕ, is called the*

***velocity potential**, while the imaginary part, ψ, is the **streamfunction**. Since the function $w(z)$*

is analytic, ϕ and ψ are related to each other via the Cauchy-Riemann equations

$$\frac{\partial \phi}{\partial x} = +\frac{\partial \psi}{\partial y},$$
$$\frac{\partial \phi}{\partial y} = -\frac{\partial \psi}{\partial x}.$$

*The **complex velocity** is defined by*

$$\frac{dw}{dz} = u - iv = \dot{x} - i\dot{y} \equiv \dot{z}^*.$$

2.6 Point Vortex Dynamics

2.6.1 Two Dimensions

In deriving an expression for point vortices on the plane, we first consider Equation (2.13) in two dimensions. The right hand side is equal to zero, therefore

$$\frac{D\omega}{Dt} \equiv 0, \tag{2.26}$$

with $\omega = (0, 0, \omega_z)^T \equiv (0, 0, \omega)^T$ and $\mathbf{u} = (u, v, 0)^T = (\dot{x}, \dot{y}, 0)^T$. We now deal with the scalar vorticity

$$\omega = \left(\frac{\partial v}{\partial x} - \frac{\partial u}{\partial y}\right). \tag{2.27}$$

Another key feature is that the vector potential ψ from Equation (2.17) becomes the scalar streamfunction found in Definition **1**. Therefore,

$$\mathbf{u} = \nabla \times \psi \equiv \begin{pmatrix} 0 & 1 \\ -1 & 0 \end{pmatrix} \begin{pmatrix} \partial_x \\ \partial_y \end{pmatrix} \psi = (\psi_y, -\psi_x)^T. \tag{2.28}$$

We now define the Hamiltonian as the streamfunction, $\mathcal{H} \equiv \psi$, since we can write

$$\dot{x} = \frac{\partial \mathcal{H}}{\partial y}(x, y; t), \quad \dot{y} = -\frac{\partial \mathcal{H}}{\partial x}(x, y; t). \tag{2.29}$$

The Cartesian positions (x, y) are the canonical conjugate variables of $\mathcal{H}$. When the flow is time-independent, it is referred to as *steady state*. The streamlines arising from $\mathcal{H}$ are tangent to the velocity lines for all time. The normal component to the velocity field, $\mathbf{n}$, becomes the gradient of the streamfunction, namely that

$$\mathbf{n} = \nabla \psi = \nabla \mathcal{H}. \tag{2.30}$$

Since we can state that $\mathbf{u} \cdot \mathbf{n} = \mathbf{u} \cdot \nabla \psi = 0$, we can conclude that the streamline curves form solid boundaries which the fluid cannot pass. This is the Hamiltonian that is used for the point vortex formulation. In the next section, we will introduce the model for N interacting discrete point vortices.

2.6.2 The Point Vortex Model

For the flowfield around a system of N discrete vortex sources, we assume the vorticity distribution

$$\omega(\mathbf{x}) = \sum_{i=1}^{N} \frac{\Gamma_i}{2\pi} \phi_\epsilon(\mathbf{x} - \mathbf{x}_i),$$

$$\phi_\epsilon(\mathbf{x}) = \frac{1}{\epsilon^2} \phi\left(\frac{\mathbf{x}}{\epsilon}\right).$$

In this definition, ϵ is a small number such that $\epsilon \ll 1$. ϕ is a normalized, radially symmetric function (i.e., $\int \phi d\mathbf{x} = 1$). In taking the limit $\epsilon \to 0$, we generate what is called the **point vortex**, and our ϕ_ϵ function becomes the Dirac delta function (i.e., $\omega(\mathbf{x}) = \phi_\epsilon(\mathbf{x}) \equiv \delta(\mathbf{x})$). Using the

solution to Poisson's equation via Green's function for the Laplacian (Equation (2.19)), we derive that the streamfunction for vortex α with position $\mathbf{x}_\alpha = (x_\alpha(t), y_\alpha(t))$, where $1 \leq \alpha \leq N$ to be

$$\psi_\alpha(\mathbf{x}, t) = -\frac{1}{2\pi} \int \Gamma_\alpha \log(\mathbf{x} - \mathbf{z}) \delta(\mathbf{x} - \mathbf{z}) d\mathbf{z} \tag{2.31}$$

$$= -\frac{\Gamma_\alpha}{2\pi} \log(\mathbf{x} - \mathbf{x}_\alpha). \tag{2.32}$$

The velocity of a passive particle in the fluid that is being advected by N point vortices can be obtained via linear superposition. That is, with the velocity being the curl of the streamfunction as in Equation (2.28), the velocity of a passive particle in the flow becomes

$$\dot{\mathbf{x}} = \sum_{\beta=1}^{N} \nabla \times \psi_\beta(\mathbf{x}, t). \tag{2.33}$$

The net velocity at the site of vortex α therefore is

$$\dot{\mathbf{x}}_\alpha = \sum_{\beta=1}^{N}{}' \nabla \times \psi_\beta(\mathbf{x}_\alpha, t). \tag{2.34}$$

The prime in the summation implies that the terms $\alpha = \beta$ are excluded since a vortex does not advect itself. Plugging Equation (2.32) into (2.34) gives us an expression for the Cartesian velocities in the plane $(\dot{x}_\alpha(t), \dot{y}_\alpha(t))$ as

$$\dot{x}_\alpha = -\frac{1}{2\pi} \sum_{\beta=1}^{N}{}' \frac{\Gamma_\beta(y_\alpha - y_\beta)}{l_{\alpha\beta}^2}, \tag{2.35}$$

and

$$\dot{y}_\alpha = \frac{1}{2\pi} \sum_{\beta=1}^{N}{}' \frac{\Gamma_\beta(x_\alpha - x_\beta)}{l_{\alpha\beta}^2}, \tag{2.36}$$

where $l_{\alpha\beta}^2 = \|\mathbf{x}_\beta - \mathbf{x}_\alpha\|^2$ is the square of the inter-vortical distance of vortices α and β. See Figure 2.26 for an illustration. In more compact form using $z_\alpha = x_\alpha + iy_\alpha$, the equations of motion can be expressed as

$$\dot{z}_\alpha = \frac{i}{2\pi} \sum_{\beta=1}^{N} {}'\Gamma_\beta \frac{z_\alpha - z_\beta}{|z_\alpha - z_\beta|^2}, \quad \beta \neq \alpha, \quad (\beta = 1, \ldots, N), \tag{2.37}$$

or alternately as

$$\dot{z}_\alpha^* = \frac{1}{2\pi i} \sum_{\beta=1}^{N} {}'\frac{\Gamma_\beta}{z_\alpha - z_\beta}, \quad \beta \neq \alpha, \quad (\beta = 1, \ldots, N). \tag{2.38}$$

The result in Equation (2.37) was first presented by Helmholtz in 1857. Kirchhoff in 1887 used Helmholtz's equations of motion to derive the Hamiltonian in canonical form:

$$\Gamma_\alpha \dot{x}_\alpha = \frac{\partial \mathcal{H}}{\partial y_\alpha}, \quad \Gamma_\alpha \dot{y}_\alpha = -\frac{\partial \mathcal{H}}{\partial x_\alpha}, \tag{2.39}$$

where $\mathcal{H}$, the Hamiltonian energy from Equations (2.35) and (2.36) ([53]) is given by

$$\mathcal{H} = \frac{1}{4\pi} \sum_{\beta=1}^{N} \sum_{\alpha=1}^{N} \Gamma_\alpha \Gamma_\beta \log(z_\alpha - z_\beta). \tag{2.40}$$

The Hamiltonian is also referred to as the *interaction energy* in the literature. The phase space, therefore, is described by the Cartesian coordinates with contours corresponding to passive fluid streamlines. The next set of constants for vortex systems is given by

$$Q + iP = \sum_{\alpha=1}^{N} \Gamma_\alpha z_\alpha, \tag{2.41}$$

where the complex quantity $Q + iP$ is also referred to as the *center of vorticity* or *linear impulse*, and for the planar setting defines the complex point about which the system is instantaneously

rotating. This quantity is also the discrete equivalent of the linear momentum for point vortex systems. In vector form, the center of vorticity is commonly written as

$$\mathbf{J} = (Q, P)^T. \tag{2.42}$$

The last conserved quantity is

$$I = \sum_{\alpha=1}^{N} \Gamma_\alpha |z_\alpha|^2, \tag{2.43}$$

where I is referred to in the literature as the *angular impulse*, and is the discrete equivalent of the *angular momentum* for point vortex systems. The next major result for point vortex dynamics was the solution to the three-vortex problem. The results were first published by Gröbli in 1877, but were not given much notice. Fourteen years later, however, Poincaré published his results for the three-vortex problem. For more background on the N-vortex problem, see [53], [5] and [52]. In the following section, we derive the condition for equilibrium on the plane and sphere.

2.7 Condition for Relative Vortex Equilbrium

2.7.1 On the Plane

Several references for vortex equilibria on the plane can be found in [7], [69], [54], [55], [56], [6], and [4]. In this section, the condition of relative vortex equilibria will be derived. We begin with the vector form of Equation (2.37) which is given by

$$\dot{\mathbf{x}}_\alpha = \frac{1}{2\pi} \sum_{\beta=1}^{N} {}' \Gamma_\beta \frac{\hat{e}_z \times (\mathbf{x}_\alpha - \mathbf{x}_\beta)}{l_{\alpha\beta}^2}, \quad (\alpha = 1 \dots N), \tag{2.44}$$

in which $\dot{\mathbf{x}}_\alpha$ is the Cartesian coordinate of vortex α, and $l_{\alpha\beta}^2$ is the square of the distance between vortices α and β, see Figure 2.26. The equilibrium condition, therefore is that these squared distances are invariant with time$-$namely:

$$\frac{d}{dt}(l_{\alpha\beta}^2) = 0 = 2(\mathbf{x}_\alpha - \mathbf{x}_\lambda) \cdot (\dot{\mathbf{x}}_\alpha - \dot{\mathbf{x}}_\lambda). \tag{2.45}$$

32
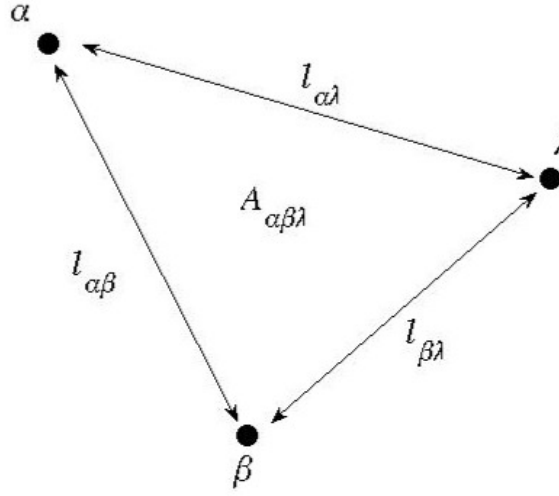
Figure 2.26: Three generic vortices α, β, λ in the plane. The distance between the vortices and the area formed between them are labeled.

Note that net translation and rotation of the system as a whole is allowed. The condition is that the distance between the vortices themselves remains unchanged with time. Rewriting the difference of velocities in terms of summations as in Equation (2.44) and simplifying,

$$
\begin{aligned}
\dot{\mathbf{x}}_\alpha - \dot{\mathbf{x}}_\lambda &= \frac{1}{2\pi} \sum_{\beta=1}^{N} {}'\Gamma_\beta \frac{\hat{e}_z \times (\mathbf{x}_\alpha - \mathbf{x}_\beta)}{l_{\alpha\beta}^2} - \frac{1}{2\pi} \sum_{\beta=1}^{N} {}'\Gamma_\beta \frac{\hat{e}_z \times (\mathbf{x}_\lambda - \mathbf{x}_\beta)}{l_{\lambda\beta}^2} \\
&= \sum_{\beta=1}^{N} {}''\Gamma_\beta \left(\frac{\hat{e}_z \times (\mathbf{x}_\alpha - \mathbf{x}_\beta)}{l_{\alpha\beta}^2} - \frac{\hat{e}_z \times (\mathbf{x}_\lambda - \mathbf{x}_\beta)}{l_{\lambda\beta}^2} \right) \\
&\quad + \frac{\Gamma_\alpha + \Gamma_\lambda}{2\pi} \frac{\hat{e}_z \times (\mathbf{x}_\alpha - \mathbf{x}_\lambda)}{l_{\alpha\lambda}^2}.
\end{aligned}
$$

The first of the two summations on the first RHS of the equation above excludes the $\alpha = \beta$ term, and the second excludes the $\lambda = \beta$ term. When these two summations are combined in the second RHS, an additional term needs to be removed from each summation in order to make the merger possible. This entails removing the β term from the first summation, and the λ term from the second summation. The last quantity in the equation above corresponds to the removed

33

α and β terms, and the double prime implies that $\beta \neq \alpha$ and also that $\beta \neq \lambda$. The next step would be to plug the above result into Equation (2.45):

$$
\begin{aligned}
\frac{d}{dt}(l_{\alpha\beta}^2) &= 2(\mathbf{x}_\alpha - \mathbf{x}_\lambda) \cdot (\dot{\mathbf{x}}_\alpha - \dot{\mathbf{x}}_\lambda) \\
&= \frac{\mathbf{x}_\alpha - \mathbf{x}_\lambda}{\pi} \sum_{\beta=1}^{N} {}''\Gamma_\beta \left(\frac{\hat{e}_z \times (\mathbf{x}_\alpha - \mathbf{x}_\beta)}{l_{\alpha\beta}^2} - \frac{\hat{e}_z \times (\mathbf{x}_\lambda - \mathbf{x}_\beta)}{l_{\lambda\beta}^2} \right) \\
&\quad + \frac{\Gamma_\alpha + \Gamma_\lambda}{\pi}(\mathbf{x}_\alpha - \mathbf{x}_\lambda) \cdot \frac{\hat{e}_z \times (\mathbf{x}_\alpha - \mathbf{x}_\lambda)}{l_{\alpha\lambda}^2} \\
&= \frac{1}{\pi} \sum_{\beta=1}^{N} (\mathbf{x}_\alpha \times \mathbf{x}_\beta + \mathbf{x}_\lambda \times \mathbf{x}_\alpha + \mathbf{x}_\beta \times \mathbf{x}_\lambda) \left(\frac{1}{l_{\alpha\beta}^2} - \frac{1}{l_{\lambda\beta}^2} \right),
\end{aligned}
$$

with

$$
\frac{\Gamma_\alpha + \Gamma_\lambda}{\pi}(\mathbf{x}_\alpha - \mathbf{x}_\lambda) \cdot \frac{\hat{e}_z \times (\mathbf{x}_\alpha - \mathbf{x}_\lambda)}{l_{\alpha\lambda}^2} = 0, \tag{2.46}
$$

since $(\mathbf{x}_\alpha - \mathbf{x}_\lambda)$ is clearly perpendicular to $\hat{e}_z \times (\mathbf{x}_\alpha - \mathbf{x}_\lambda)$. The sum of the three cross products above can be rewritten in the following way:

$$
\begin{aligned}
&(\mathbf{x}_\alpha \times \mathbf{x}_\beta) + (\mathbf{x}_\lambda \times \mathbf{x}_\alpha) + (\mathbf{x}_\beta \times \mathbf{x}_\lambda) \\
&= (\mathbf{x}_\alpha \times \mathbf{x}_\alpha) - (\mathbf{x}_\beta \times \mathbf{x}_\alpha) - (\mathbf{x}_\alpha \times \mathbf{x}_\lambda) + (\mathbf{x}_\beta \times \mathbf{x}_\lambda) \\
&= \mathbf{x}_\alpha \times (\mathbf{x}_\alpha \times \mathbf{x}_\lambda) - \mathbf{x}_\beta \times (\mathbf{x}_\alpha \times \mathbf{x}_\lambda) \\
&= (\mathbf{x}_\alpha \times \mathbf{x}_\beta) \times (\mathbf{x}_\alpha \times \mathbf{x}_\lambda) \\
&= \pm 2 A_{\alpha\beta\lambda} \hat{e}_z \\
&= 2 \epsilon_{\alpha\beta\lambda} A_{\alpha\beta\lambda} \hat{e}_z,
\end{aligned}
$$

where $A_{\alpha\beta\lambda}$ is the area of the parallelogram generated by the cross product of the two vectors (which also corresponds to the sides of the triangle in Figure 2.26. $\epsilon_{\alpha\beta\lambda}$ is the sign of the

expression ($\pm$ 1), which is dictated by the clockwise ($+1$) or counter-clockwise (-1) ordering of vortices α, β and λ. The governing equilibrium condition then becomes

$$\frac{d}{dt}(l_{\alpha\beta}^2) \equiv \sum_{\beta=1}^{N} {}''\Gamma_\beta A_{\alpha\beta\lambda}\epsilon_{\alpha\beta\lambda}\left(\frac{1}{l_{\alpha\beta}^2} - \frac{1}{l_{\lambda\beta}^2}\right), \quad \alpha \neq \beta \neq \lambda, \tag{2.47}$$

or

$$\sum_{\beta=1}^{N} {}''\Gamma_\beta A_{\alpha\beta\lambda}\epsilon_{\alpha\beta\lambda}\left(\frac{1}{l_{\alpha\beta}^2} - \frac{1}{l_{\lambda\beta}^2}\right) \equiv 0. \tag{2.48}$$

The idea is to cycle through all the possible intervortical distances and come up with $N(N-1)/2$ equations, which can be rewritten in matrix form:

$$A\mathbf{\Gamma} = 0, \tag{2.49}$$

where $A \in \mathbb{R}^{N(N-1)/2 \times N}$ is the **configuration matrix** and $\mathbf{\Gamma} \in \mathbb{R}^N$ is a vector containing the vortex strengths of the system. The system has a non-trivial solution if the covariance matrix $A^T A$ is singular, namely that

$$\det\left(A^T A\right) \equiv 0. \tag{2.50}$$

2.7.2   On the Sphere

The equilibrium condition for vortices on the sphere is solved in a similar fashion as that for vortices on the plane. The coupled equations of motion of N vortices on the surface of a unit sphere are given by

$$\dot{\mathbf{x}}_\alpha = \frac{1}{2\pi}\sum_{\beta=1}^{N}{}'\Gamma_\beta \frac{\mathbf{x}_\alpha \times \mathbf{x}_\beta}{1 - \mathbf{x}_\alpha \cdot \mathbf{x}_\beta}, \quad (\alpha = 1\dots N), \tag{2.51}$$

where $\mathbf{x}$ is the three dimensional Cartesian unit vector that points from the center of the sphere to a fluid point on the surface of the sphere and $1 \leq \alpha \leq N$ is the vortex number. The α term is

(a) 3 vortices on sphere　　　　　　　　　(b) Volume view
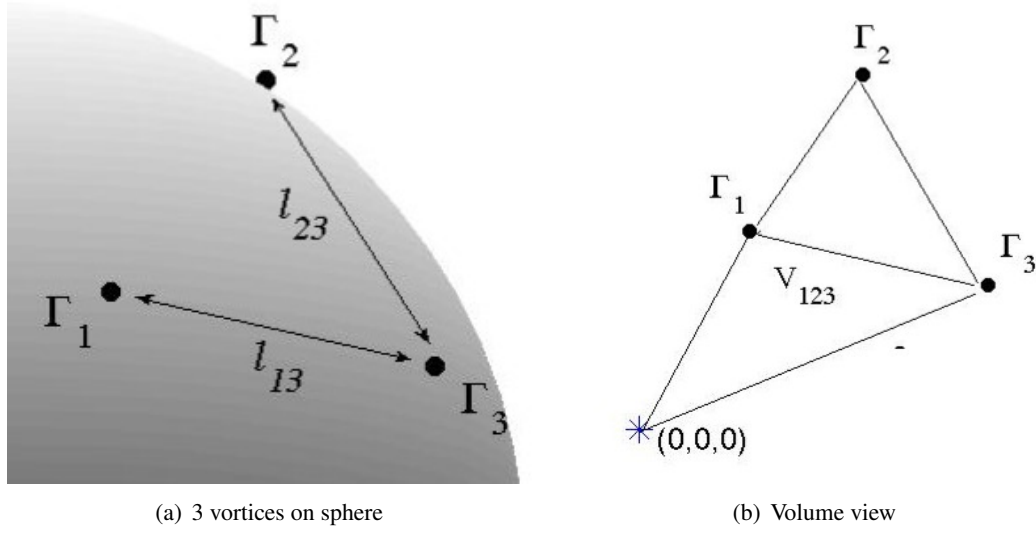
Figure 2.27:　Image of three generic vortices on the sphere that show the definition of vortex strengths (Γ's), intervortical lengths (l_{12}, l_{13}, l_{23}), and volume V_{123}.

excluded from the summation since a vortex does not advect itself. The denominator of Equation (2.51) is the square of the chord distance between vortices α and β:

$$l_{\alpha\beta}^2 = ||\mathbf{x}_\alpha - \mathbf{x}_\beta||^2 = 2(1 - \mathbf{x}_\alpha \cdot \mathbf{x}_\beta). \tag{2.52}$$

Additional relevant formulations for vortex systems on the sphere in our analysis include the center of vorticity vector $\mathbf{J}$ which describes the instantaneous axis about which the system is rigidly rotating, and is given by

$$\mathbf{J} = \sum_{\alpha=1}^{N} \Gamma_\alpha \mathbf{x}_\alpha. \tag{2.53}$$

Furthermore (from [53]), the equations of motion in terms of the longitudinal and latitudinal angles (θ_α and ϕ_α respectively) are given by

$$\dot{\phi}_\alpha = \frac{1}{4\pi} \sum_{\lambda \neq \alpha}^{N} \Gamma_\lambda \frac{\sin \phi_\alpha \sin \phi_\lambda \cos (\theta_\alpha - \theta_\lambda)}{1 - \cos \gamma_{\alpha\lambda}}, \tag{2.54}$$

36

and

$$\dot{\theta}_\alpha = \frac{1}{4\pi \sin \phi_\alpha} \sum_{\lambda \neq \alpha}^{N} \Gamma_\lambda \frac{\sin \phi_\alpha \cos \phi_\lambda - \cos \phi_\alpha \sin \phi_\lambda \cos (\theta_\alpha - \theta_\lambda)}{1 - \cos \gamma_{\alpha\lambda}}, \tag{2.55}$$

with

$$\cos \gamma_{\alpha\lambda} = \cos \phi_\alpha \cos \phi_\lambda + \sin \phi_\alpha \sin \phi_\lambda \cos (\theta_\alpha - \theta_\lambda). \tag{2.56}$$

As for the condition for an equilibrium configuration, as before, is that the distance between the vortices remains equidistant, or that

$$\frac{d}{dt} \left(l_{\alpha\beta}^2 \right) = 2(\mathbf{x}_\alpha - \mathbf{x}_\beta) \cdot (\dot{\mathbf{x}}_\alpha - \dot{\mathbf{x}}_\beta) = 0. \tag{2.57}$$

The difference of velocities can be written as

$$\begin{aligned}
\dot{\mathbf{x}}_\alpha - \dot{\mathbf{x}}_\beta &= \frac{1}{2\pi} \sum_{\lambda \neq \alpha}^{N} {}'\Gamma_\lambda \frac{\mathbf{x}_\alpha \times \mathbf{x}_\lambda}{l_{\alpha\lambda}^2} - \frac{1}{2\pi} \sum_{\lambda \neq \beta}^{N} {}'\Gamma_\lambda \frac{\mathbf{x}_\beta \times \mathbf{x}_\lambda}{l_{\beta\lambda}^2} \\
&= \frac{1}{2\pi} \sum_{\lambda \neq \beta, \lambda \neq \alpha}^{N} {}''\Gamma_\lambda \left(\frac{\mathbf{x}_\alpha \times \mathbf{x}_\lambda}{l_{\alpha\lambda}^2} - \frac{\mathbf{x}_\beta \times \mathbf{x}_\lambda}{l_{\beta\lambda}^2} \right) \\
&\quad - \frac{1}{2\pi} (\Gamma_\beta + \Gamma_\alpha) \frac{\mathbf{x}_\alpha \times \mathbf{x}_\beta}{l_{\alpha\beta}^2}.
\end{aligned}$$

Using this result in Equation 2.57,

$$\begin{aligned}
\frac{d}{dt} \left(l_{\alpha\beta}^2 \right) &= \frac{1}{\pi} (\mathbf{x}_\alpha - \mathbf{x}_\beta) \cdot \sum_{\lambda \neq \beta, \lambda \neq \alpha}^{N} {}''\Gamma_\lambda \left(\frac{\mathbf{x}_\alpha \times \mathbf{x}_\lambda}{l_{\alpha\lambda}^2} - \frac{\mathbf{x}_\beta \times \mathbf{x}_\lambda}{l_{\beta\lambda}^2} \right) \\
&\quad - \frac{1}{\pi} (\Gamma_\beta + \Gamma_\alpha)(\mathbf{x}_\alpha - \mathbf{x}_\beta) \cdot \frac{\mathbf{x}_\alpha \times \mathbf{x}_\beta}{l_{\alpha\beta}^2}.
\end{aligned}$$

The last portion on the second line of the equation above is equivalent to zero since the cross product of $\mathbf{x}_\alpha$ and $\mathbf{x}_\beta$ is perpendicular to the plane containing them (and the inner product is zero). Simplifying, one gets

$$\pi \frac{d}{dt} \left(l_{\alpha\beta}^2 \right) = \sum_{\lambda \neq \beta, \lambda \neq \alpha}^{N} {}''\Gamma_\lambda \left(\frac{\mathbf{x}_\beta \cdot \mathbf{x}_\lambda \times \mathbf{x}_\alpha}{l_{\alpha\lambda}^2} - \frac{\mathbf{x}_\beta \cdot \mathbf{x}_\lambda \times \mathbf{x}_\alpha}{l_{\beta\lambda}^2} \right). \tag{2.58}$$

Note that $\mathbf{x}_\beta \cdot \mathbf{x}_\lambda \times \mathbf{x}_\alpha$ is the scalar triple product that gives the volume of the parallelepiped formed between the three vectors; this volume is denoted as $V_{\alpha\beta\lambda}$. The condition for equilibrium becomes:

$$\frac{d}{dt}\left(l_{\alpha\beta}^2\right) = 0 \equiv \sum_{\lambda\neq\beta,\lambda\neq\alpha}^{N} {}''\Gamma_\lambda \epsilon_{\alpha\beta\lambda} V_{\alpha\beta\lambda}\left(\frac{1}{l_{\alpha\lambda}^2} - \frac{1}{l_{\beta\lambda}^2}\right). \tag{2.59}$$

Using this equation, as before, it is necessary to cycle between all the possible lengths in the configuration. Therefore, we will have a total $N(N-1)/2$ equations. The system can be placed in matrix form:

$$A\mathbf{\Gamma} = 0, \tag{2.60}$$

where A and $\mathbf{\Gamma}$ are synonymous to those of Equation (2.49). The condition for equilibrium is identical to Equation (2.50). More detailed results for vortex equilibria on the sphere can be found in [39] and [15].

Chapter 3. Linear Algebra Methods

In this chapter, three main methods from linear algebra will be discussed. In **3.1**, we will define Singular Value Decomposition. In **3.2**, Shannon Entropy will be introduced, and in **3.3** a matrix approximation technique will be presented. In each section, examples showing either their application to the vortex equilibrium condition in equations (2.49) (on the plane) and (2.60) (on the sphere) or to matrices will be presented.

3.8   Singular Value Decomposition

We begin with Singular Value Decomposition (a definitive reference on this topic can be found in [41]). Now that an equilibrium condition has been formulated (see sections **2.7.1** and **2.7.2**), the solution to the dynamical system has to be found (i.e., the strength of the vortices, or vector Γ from (2.49) and (2.60)).

3.8.1   Definition

Singular Value Decomposition (SVD) is the equivalent of matrix decomposition for non-normal matrices (i.e., $A^T A \neq A A^T$). Instead of having eigenvalues and eigenvectors, SVD has *singular values* and *singular vectors*. SVD is utilized in a variety of applications−from robotics & kinematics, to graphics ([71]), information compression ([22]) and retrieval ([9]), and the following

chapter will illustrate its usefulness in the context of point vortex equilbria. For an $M \times N$ non-normal real rectangular matrix A with $M > N$, the singular values must satisfy the following conditions:

$$A\mathbf{v}^{(i)} = \sigma^{(i)}\mathbf{u}^{(i)}, \quad A^T\mathbf{u}^{(i)} = \sigma^{(i)}\mathbf{v}^{(i)}, \quad i = 1 \cdots N, \tag{3.61}$$

where $\sigma^{(i)}$ is the ith singular value, $\mathbf{u}^{(i)} \in \mathbb{R}^M$ is the ith left singular vector and $\mathbf{v}^{(i)} \in \mathbb{R}^N$ is the ith right singular vector. The decomposition is expressed as

$$A = U\Sigma V^T, \tag{3.62}$$

where U and V are square unitary matrices (i.e., $U^T U = I \in \mathbb{R}^M$, $V^T V = I \in \mathbb{R}^N$) composed of the left and right singular vectors respectively. Σ is an $M \times N$ diagonal matrix containing the singular values in the form

$$\Sigma = \begin{pmatrix} \sigma^{(1)} & 0 & \cdots & 0 & 0 \\ 0 & \sigma^{(2)} & & 0 & 0 \\ \vdots & & \ddots & & \vdots \\ 0 & 0 & \sigma^{(N-1)} & 0 \\ 0 & 0 & \cdots & 0 & \sigma^{(N)} \\ 0 & 0 & \cdots & 0 & 0 \\ \vdots & \vdots & & \vdots & \vdots \\ 0 & 0 & \cdots & 0 & 0 \end{pmatrix}. \tag{3.63}$$

The singular values are ordered diagonally from largest to smallest in the first N rows of Σ, and the remaining $M - N$ rows are zeros. The rank of A is 'r' and is equal to the number of non-zero $\sigma^{(i)}$'s (i.e., $\sigma^{(max)} \equiv \sigma^{(1)} \geq \sigma^{(2)} \geq \cdots \geq \sigma^{(r)} > 0 = \sigma^{(r+1)} = \cdots = \sigma^{(N)}$). As can be seen from multiplying the first equation in Eq. (3.61) by A^T and the second by A, the following relations emerge:

$$(A^T A - \sigma^{(i)2})\mathbf{v}^{(i)} = 0, \quad (AA^T - \sigma^{(i)2})\mathbf{u}^{(i)} = 0, \tag{3.64}$$

40

which indicates that the squares of the singular values of A are also the eigenvalues of the square covariance matrices $A^T A$ and AA^T and their eigenvectors are $\mathbf{v}^{(i)}$ and $\mathbf{u}^{(i)}$ respectively. Note also that the ranks of A, $A^T A$ and AA^T are all the same. With the knowledge that $nullity(A) + rank(A) = N$, a nontrivial solution to Equations (2.49) and (2.60) exists when the rank of A is less than N, which in (3.61) implies that $\sigma^{(i)} = \{0, \quad i > r\}$, and gives

$$A\mathbf{v}^{(i)} = \sigma^{(i)}\mathbf{u}^{(i)} = \mathbf{0}. \tag{3.65}$$

Therefore, the columns of V associated with $\sigma^{(r+1)}, \sigma^{(r+2)}, \cdots, \sigma^{(N)}$ correspond to to the non-trivial solution of the homogeneous system of equations $A\boldsymbol{\Gamma} = 0$, or namely by the linear super-position

$$\boldsymbol{\Gamma} = c_1\mathbf{v}^{(r+1)} + c_2\mathbf{v}^{(r+2)} + \cdots + c_{N-r}\mathbf{v}^{(N)}, \tag{3.66}$$

where $c_1, c_2, \cdots c_{N-r}$ are constants in $\mathbb{R}$ that can be chosen arbitrarily. In the context of point vortex equilibria and with null spaces larger than one, it is desirable to convert the solution in Equation (3.66) into a rational basis of reduced echelon form by using a series of matrix operations. In other words,

$$\begin{pmatrix} \mathbf{v}^{(r+1)} & \mathbf{v}^{(r+2)} & \cdots & \mathbf{v}^{(N)} \end{pmatrix} \begin{pmatrix} c_1 \\ c_2 \\ \vdots \\ c_{N-r} \end{pmatrix} \equiv X \begin{pmatrix} \alpha_1 \\ \alpha_2 \\ \vdots \\ \alpha_{N-r} \end{pmatrix} = \mathbf{0}. \tag{3.67}$$

Matrix $X = \begin{pmatrix} \mathbf{x}^{(r+1)} & \mathbf{x}^{(r+2)} & \cdots & \mathbf{x}^{(N)} \end{pmatrix}$ is in reduced echelon form, $\alpha_1 \cdots \alpha_{N-r}$ are the new arbitrary constants, and the new solution is given by

$$\boldsymbol{\Gamma} = \alpha_1\mathbf{x}^{(r+1)} + \alpha_2\mathbf{x}^{(r+2)} + \cdots + \alpha_{N-r}\mathbf{x}^{(N)}. \tag{3.68}$$

Note that in the event that vectors $\mathbf{v}^{(r+1)}, \mathbf{v}^{(r+2)}, \cdots, \mathbf{v}^{(N)}$ are already in reduced echelon form, no linear transformation needs to be made.

3.8.2 Computation of the SVD

A basic way of computing the singular values is by first forming the square covariance matrices AA^T or $A^T A$, and then solving for their eigenvalues. From Equation (3.64), the singular values of A are then the square root of the eigenvalues. The problem with this approach is that it can be numerically unstable ([70]). From [41], an alternative way of computing the singular values is by solving the left and right singular vectors directly from

$$\begin{pmatrix} \mathbf{0} & A \\ A^T & \mathbf{0} \end{pmatrix} \begin{pmatrix} \mathbf{u}^{(i)} \\ \mathbf{v}^{(i)} \end{pmatrix} = \sigma^{(i)} \begin{pmatrix} \mathbf{u}^{(i)} \\ \mathbf{v}^{(i)} \end{pmatrix} \tag{3.69}$$

The benefit of this approach is that if the matrix A is perturbed by a small amount, it can be shown that the perturbed singular value $\hat{\sigma}^{(i)}$ satisfies

$$|\hat{\sigma}^{(i)} - \sigma^{(i)}| = O(\epsilon \|A\|).$$

For further efficient algorithms for deriving the decomposition, see [60] and [42].

3.8.3 SVD Example

Examples of how this method works in the context of point vortex equilibria will be given for two square configurations with $N = 4$ and $N = 5$.

3.8.3.1 Havelock's Square ($N = 4$)

The square vortex configuration was studied by Havelock ([35]), and was shown to be linearly stable. The configuration contains four vortices placed at the corners of a square (see Figure 3.28). See Figures 1.2 and 1.10 for examples of this lattice configuration in physical settings. Recall that for N vortices, there exist $N(N-1)/2$ intervortical distances. The number of vortices $N = 4$ for this case gives a total of $4(3)/2 = 6$ intervortical distances, and hence there are 6 equations and 4 unknown vortex strengths to be solved. Using equation (2.45), and
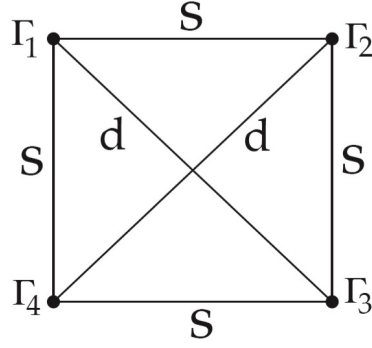
Figure 3.28: Four vortices on the plane in a square configuration, and without loss of generality, with side of unit length $S = 1$.

considering that the sides of the square have unit length, the first of the six equations for this system has the form:

$$
\begin{aligned}
\pi \frac{d}{dt}(l_{12}^2) &= 0 + 0 + \Gamma_3 A_{132}\epsilon_{132}\left(\frac{1}{l_{13}^2} - \frac{1}{l_{23}^2}\right) + \Gamma_4 A_{142}\epsilon_{142}\left(\frac{1}{l_{14}^2} - \frac{1}{l_{24}^2}\right) \\
&= \Gamma_3\left(\frac{1}{2}\right)(-1)\left(\frac{1}{2} - \frac{1}{1}\right) + \Gamma_4\left(\frac{1}{2}\right)(-1)\left(\frac{1}{1} - \frac{1}{2}\right) \\
&= \frac{1}{4}\Gamma_3 - \frac{1}{4}\Gamma_4 \\
&= \frac{1}{4}\begin{pmatrix} 0 & 0 & 1 & -1 \end{pmatrix}\begin{pmatrix} \Gamma_1 \\ \Gamma_2 \\ \Gamma_3 \\ \Gamma_4 \end{pmatrix} \\
&= 0.
\end{aligned}
$$

The next five equations in A, which correspond to rate of change of the squares of the inter-vortical distances l_{13}^2, l_{14}^2, l_{23}^2, l_{24}^2, and l_{34}^2 can be solved in a similar fashion, and placing them

in matrix form (see Equation (2.49)) as well as reordering them diagonally, the configuration matrix for this particular system becomes:

$$
\begin{pmatrix}
A_{341}\left(\frac{1}{l_{31}^2}-\frac{1}{l_{41}^2}\right) & A_{342}\left(\frac{1}{l_{32}^2}-\frac{1}{l_{42}^2}\right) & 0 & 0 \\
A_{241}\left(\frac{1}{l_{21}^2}-\frac{1}{l_{41}^2}\right) & 0 & A_{243}\left(\frac{1}{l_{23}^2}-\frac{1}{l_{43}^2}\right) & 0 \\
A_{231}\left(\frac{1}{l_{21}^2}-\frac{1}{l_{31}^2}\right) & 0 & 0 & A_{234}\left(\frac{1}{l_{24}^2}-\frac{1}{l_{34}^2}\right) \\
0 & A_{142}\left(\frac{1}{l_{12}^2}-\frac{1}{l_{42}^2}\right) & A_{143}\left(\frac{1}{l_{13}^2}-\frac{1}{l_{43}^2}\right) & 0 \\
0 & A_{132}\left(\frac{1}{l_{12}^2}-\frac{1}{l_{32}^2}\right) & 0 & A_{134}\left(\frac{1}{l_{14}^2}-\frac{1}{l_{34}^2}\right) \\
0 & 0 & A_{123}\left(\frac{1}{l_{13}^2}-\frac{1}{l_{23}^2}\right) & A_{124}\left(\frac{1}{l_{14}^2}-\frac{1}{l_{24}^2}\right)
\end{pmatrix}. \quad (3.70)
$$

Replacing all the symbolic forms above with their numerically equivalent results, and placing A in Equation (2.49), we get

$$
A\Gamma = \frac{1}{4}
\begin{pmatrix}
1 & -1 & 0 & 0 \\
0 & 0 & 0 & 0 \\
-1 & 0 & 0 & 1 \\
0 & 1 & -1 & 0 \\
0 & 0 & 0 & 0 \\
0 & 0 & 1 & -1
\end{pmatrix}
\begin{pmatrix}
\Gamma_1 \\ \Gamma_2 \\ \Gamma_3 \\ \Gamma_4
\end{pmatrix}
=
\begin{pmatrix}
0 \\ 0 \\ 0 \\ 0
\end{pmatrix}
\quad (3.71)
$$

As in Equation (3.62), Singular Value Decomposition of A gives the following three matrices:

$$
U =
\begin{pmatrix}
-0.5 & 0.5 & 0.5 & -0.1015 & 0 & 0 \\
0 & 0 & 0 & 0.9792 & 0 & 0 \\
0.5 & -0.5 & 0.5 & -0.1015 & 0 & 0 \\
0.5 & 0.5 & -0.5 & -0.1015 & 0 & 0 \\
0 & 0 & 0 & 0 & 0 & 0 \\
-0.5 & -0.5 & -0.5 & -0.1015 & 0 & 0
\end{pmatrix},
\quad (3.72)
$$

$$\Sigma = \begin{pmatrix} -0.5 & 0 & 0 & 0 \\ 0 & 0.3536 & 0 & 0 \\ 0 & 0 & 0.3536 & 0 \\ 0 & 0 & 0 & 0 \\ 0 & 0 & 0 & 0 \\ 0 & 0 & 0 & 0 \end{pmatrix},$$

(3.73)

$$V = \begin{pmatrix} -0.5 & 0.7071 & 0 & -0.5 \\ 0.5 & 0 & -0.7071 & -0.5 \\ -0.5 & -0.7071 & 0 & -0.5 \\ 0.5 & 0 & 0.7071 & -0.5 \end{pmatrix}.$$

(3.74)

The singular values are $(\sigma^{(1)}, \sigma^{(2)}, \sigma^{(3)}, \sigma^{(4)}) = (1/2, 1/2\sqrt{2}, 1/2\sqrt{2}, 0)$. The 4th singular value in matrix Σ is equal to zero, which indicates that the rank of the configuration matrix A is 3, giving a null space of 1. Using Equation (3.68), the solution of the system lies in the 4th right-most eigenvector $\mathbf{v}^{(4)}$:

$$\mathbf{\Gamma} = \mathbf{v}^{(4)} = \begin{pmatrix} -0.5 \\ -0.5 \\ -0.5 \\ -0.5 \end{pmatrix} \equiv \alpha_1 \begin{pmatrix} 1 \\ 1 \\ 1 \\ 1 \end{pmatrix}, \quad \alpha_1 \in \mathbb{R}.$$

(3.75)

This solution means that the four vortices must all have the same strength for the configuration to remain in equilibrium. Note also that this strength, given by α_1, can be any real number.

3.8.3.2 Havelock's Square Plus Central Vortex ($N = 5$)

We now consider the same square configuration with an additional vortex located at the center of the square, thus having a total of five vortices (see the schematic of the solution in Figure 3.29). This type of configuration appears in the milli-sized magnets lattices from [34], and they appear
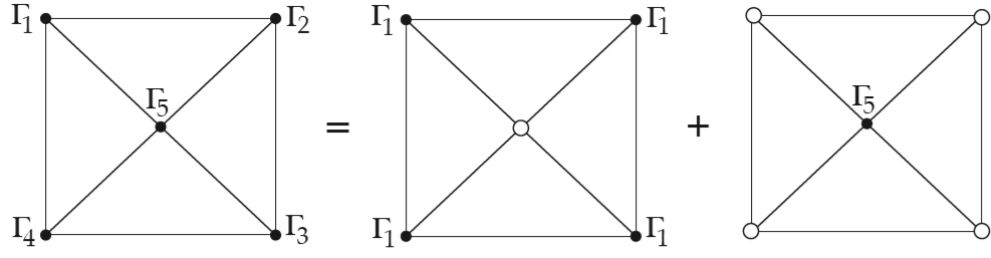
Figure 3.29: Solution to the 5-vortex square lattice configuration. The four outer edge vortices share one common strength, while the central vortex has an independent strength ([56]).

on the curved surface of a water drop in Figure 1.11. The configuration matrix from Equation (2.49) for this case will be of dimension $5(4)/2 \times 5 = 10 \times 5$ and when solved gives

$$
A = \begin{pmatrix}
-1 & 0 & 1 & 0 & 0 \\
0 & 1 & 0 & -1 & 0 \\
1 & -1 & 0 & 0 & 0 \\
1 & 0 & -1 & 0 & 0 \\
0 & 0 & 0 & 0 & 0 \\
-1 & 0 & 0 & 1 & 0 \\
0 & -1 & 0 & 1 & 0 \\
0 & -1 & 0 & 1 & 0 \\
0 & 1 & -1 & 0 & 0 \\
0 & 0 & 1 & -1 & 0
\end{pmatrix} .
\tag{3.76}
$$

Matrix decomposition as in (3.62) for this configuration gives

$$
U = \begin{pmatrix}
-0.5774 & 0 & 0 & -0.2224 & 0 & 0 & 0 & 0 & 0 & 0 \\
0 & 0.5774 & 0 & -0.7195 & 0 & 0 & 0 & 0 & 0 & 0 \\
0.2887 & -0.2887 & -0.5 & -0.0908 & 0 & 0 & 0 & 0 & 0 & 0 \\
0.5774 & 0 & 0 & -0.2993 & 0 & 0 & 0 & 0 & 0 & 0 \\
0 & 0 & 0 & 0 & 1 & 0 & 0 & 0 & 0 & 0 \\
-0.2887 & -0.2887 & 0.5 & -0.1677 & 0 & 0 & 0 & 0 & 0 & 0 \\
0 & -0.5774 & 0 & -0.5481 & 0 & 0 & 0 & 0 & 0 & 0 \\
0.2887 & 0.2887 & 0.5 & 0.0806 & 0 & 0 & 0 & 0 & 0 & 0 \\
0 & 0 & 0 & 0 & 0 & 0 & 0 & 0 & 0 & 0 \\
-0.2887 & 0.2887 & -0.5 & 0.0037 & 0 & 0 & 0 & 0 & 0 & 0
\end{pmatrix},
\tag{3.77}
$$

$$
\Sigma = \begin{pmatrix}
\frac{\sqrt{3}}{2\sqrt{2}} & 0 & 0 & 0 & 0 \\
0 & \frac{\sqrt{3}}{2\sqrt{2}} & 0 & 0 & 0 \\
0 & 0 & 1/2 & 0 & 0 \\
0 & 0 & 0 & 0 & 0 \\
0 & 0 & 0 & 0 & 0 \\
0 & 0 & 0 & 0 & 0 \\
0 & 0 & 0 & 0 & 0 \\
0 & 0 & 0 & 0 & 0 \\
0 & 0 & 0 & 0 & 0 \\
0 & 0 & 0 & 0 & 0
\end{pmatrix},
\tag{3.78}
$$

$$
V = \begin{pmatrix}
0.7071 & 0 & -0.5 & 0.5 & 0 \\
0 & 0.7071 & 0.5 & 0.5 & 0 \\
-0.7071 & 0 & -0.5 & 0.5 & 0 \\
0 & -0.7071 & 0.5 & 0.5 & 0 \\
0 & 0 & 0 & 0 & 1
\end{pmatrix}.
\tag{3.79}
$$

The singular values for this configuration are

$$
\begin{pmatrix} \sigma^{(1)} \\ \sigma^{(2)} \\ \sigma^{(3)} \\ \sigma^{(4)} \\ \sigma^{(5)} \end{pmatrix} = \begin{pmatrix} \frac{\sqrt{3}}{2\sqrt{2}} \\ \frac{\sqrt{3}}{2\sqrt{2}} \\ \frac{1}{2} \\ 0 \\ 0 \end{pmatrix}. \tag{3.80}
$$

The two smallest singular values are zero, which indicates that the dimension of the solution space of this configuration is 2 and is found in the 4th and 5th right singular vectors. The solution, therefore, becomes

$$
\mathbf{\Gamma} = \begin{pmatrix} \Gamma_1 \\ \Gamma_2 \\ \Gamma_3 \\ \Gamma_4 \\ \Gamma_5 \end{pmatrix} = \alpha_1 \mathbf{v}^{(4)} + \alpha_2 \mathbf{v}^{(5)} = \alpha_1 \begin{pmatrix} 1 \\ 1 \\ 1 \\ 1 \\ 0 \end{pmatrix} + \alpha_2 \begin{pmatrix} 0 \\ 0 \\ 0 \\ 0 \\ 1 \end{pmatrix}, \quad \alpha_1, \alpha_2 \in \mathbb{R}, \tag{3.81}
$$

where α_1 and α_2 are arbitrary constants. This implies that the four vortices forming the square have equal strengths ($\Gamma_1 = \Gamma_2 = \Gamma_3 = \Gamma_4 = \alpha_1$), and that the central vortex has a different, independent strength ($\Gamma_5 = \alpha_2$). This 5-vortex configuration can be reduced to the square lattice by choosing $\alpha_2 = 0$.

In this section of this chapter, our focus has solely been on the role of the zero singular values associated with the configuration matrix, as they determined whether a given configuration has a non-trivial solution. In the following two sections, we will look at the information encoded in the *non-zero* singular values.
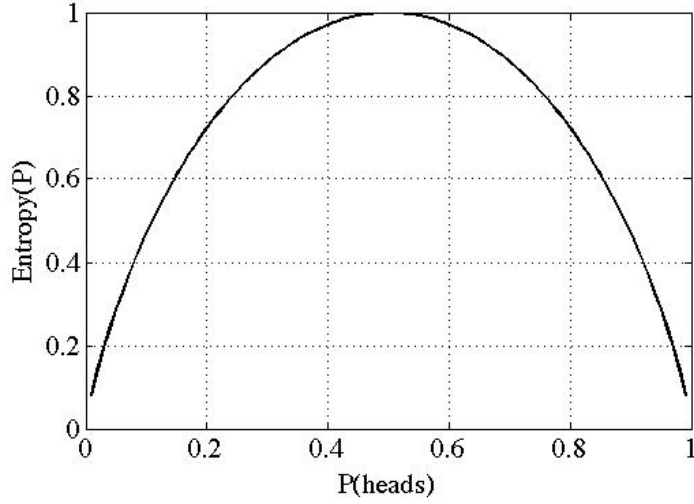
Figure 3.30: Shannon Entropy vs. the probability of getting heads from a dice throw. Maximum entropy occurs when the probability = 1/2, which coincides with the proposition that the probability with the highest Shannon Entropy is also the most likely to occur.

3.9 Shannon Entropy

3.9.1 Definition

Shannon in [67] introduced a scalar measure for entropy, which is referred to as the *Shannon Entropy* 'H'. We describe the entropy, or modal energy distribution of a system $\vec{P}$ with probabilities $(P_1, P_2, \ldots, P_N)$ by

$$H = -\sum_{\alpha=1}^{N} P_\alpha \ln P_\alpha, \quad P_\alpha \neq 0, \quad 0 \leq H \leq \ln N. \tag{3.82}$$

Alternately, to normalize the system, $\log_N$ can be chosen instead of $\ln \equiv \log_e$ in Equation (3.82). In other words, the normalized Shannon Entropy becomes

$$H = -\sum_{\alpha=1}^{N} P_\alpha \log_N (P_\alpha), \quad P_\alpha \neq 0, \quad 0 \leq H \leq 1. \tag{3.83}$$

The Shannon Entropy of a system can be used to determine how likely it is for a certain system $\vec{P}$ to occur. An intuitive example is the throwing of a dice. The system has two likely outcomes,

and is defined as $\vec{P} = (P(heads), P(tails)) = (P_1, P_2)$, where P_1 is the probability of landing heads, and P_2 is the probability of landing tails with $P_1 + P_2 = 1$. Note that we can rewrite the system as $\vec{P} = (P_1, 1 - P_1)$. Intuitively, we know that the most likely outcome of the coin toss would be that we land heads half the time ($P_1 = 1/2$), and tails during the other half. Therefore, we expect the system $\vec{P} = (1/2, 1/2)$ to be the *most likely* or *most robust*, while the systems $\vec{P} = (1, 0)$ and $\vec{P} = (0, 1)$ to be least likely. Since there are only two possible outcomes to the coin toss, we can use $\log_2$ in the formulation, and with Equation (3.83) the Shannon Entropy of our system becomes

$$
\begin{aligned}
H &= -\sum_{\alpha=1}^{N} P_\alpha \log_2 P_\alpha \\
&= -P_1 \log_2 P_1 - (1 - P_1) \log_2 (1 - P_1).
\end{aligned}
$$

Figure 3.30 illustrates H vs. P_1, and shows us that the maximum entropy occurs when $P_1 = 1/2$. This supports the claim that there is a positive correlation between the Shannon Entropy and likelihood of an event to occur.

In the context of a non-normal matrix A, we interpret the normalized eigenvalues of the corresponding covariance matrices AA^T and $A^T A$ from Equation (3.64) as the probabilities, which gives us

$$
P_\alpha = \hat{\lambda}_\alpha = \frac{\lambda_\alpha}{\sum_{\beta=1}^{N} \lambda_\beta} = \frac{\left(\sigma^{(\alpha)}\right)^2}{\sum_{\beta=1}^{N} \left(\sigma^{(\beta)}\right)^2}, \quad \alpha = 1 \cdots N. \tag{3.84}
$$

An alternate way of interpreting the Shannon Entropy is by the *information compression* present in a system, which we will briefly define in the following subsection.

3.9.2   Information Compression

Consider the two general square diagonal matrices of dimension N below:

$$V_{min} = \begin{pmatrix} 1 & & & & \\ & 1 & & & \\ & & \ddots & & \\ & & & 1 & \\ & & & & 1 \end{pmatrix}, \quad V_{max} = \begin{pmatrix} 1 & & & & \\ & 0 & & & \\ & & \ddots & & \\ & & & 0 & \\ & & & & 0 \end{pmatrix}. \tag{3.85}$$

Since both matrices are diagonal, the eigenvalues are simply the diagonal elements. V_{min} has eigenvalues $(1, 1, \ldots, 1, 1)$. All its eigenvalues are equal in magnitude, and the matrix is said to have *minimum information compression* since all its numerical information is equally distributed among its N modes, or eigenvalues. We can also state that the probability for numerical information to lie on any given mode is $(100/N)\%$. Matrix V_{max}'s eigenvalues are $(1, 0, \ldots, 0, 0)$. Since all the numerical information is compressed into its first mode, V_{max} is said to have *maximum information compression*. For this matrix, there is a 100% probability that the numerical information will lie on the first mode, and a 0% probability for it to lie on any of the remaining $(N - 1)$ modes.

If a system has minimum compression, it is said to have *maximum entropy* since its information is as distributed as possible throughout the modes of the system. On the other hand, if a system has maximum compression, it is said to have *minimum entropy* since its information is condensed into a single mode. Referring back to the two matrices V_{min} and V_{max} (which represent the two extreme possible scenarios) defined in Equation (3.85), the probabilities (derived from Equation (3.84)) associated with V_{min} are $(1/N, 1/N, \ldots, 1/N, 1/N)$. Using Equation (3.82),

$$H_{max} = -\frac{1}{N} \ln \frac{1}{N} - \frac{1}{N} \ln \frac{1}{N} - \ldots - \frac{1}{N} \ln \frac{1}{N} = \ln N. \tag{3.86}$$

On the other hand, the minimum possible Shannon Entropy, H_{min} can be derived from $\vec{P}(V_{max}) = \vec{P}(1, 0, \ldots, 0)$. From Equation (3.82), the minimum entropy is simply

$$H_{min} = -\ln 1 = 0. \tag{3.87}$$

This tells us that the entropy H of any system with dimension N is bounded by $0 < H < \ln N$. Therefore, from [67], any system has the following properties:

1. $H = 0$ if and only if all the P_α but one are zero, this one having the value unity. Thus only when we are certain of the outcome does H vanish. Otherwise H is positive

2. For a given N, H is maximum and equal to $\ln N$ when all the P_α are equal (i.e., $\frac{1}{N}$). This is also intuitively the most uncertain situation.

With this in consideration, we can derive an expression for the percentage of information compression in a system as

$$\frac{\ln N - H}{\ln N} \cdot 100\%, \tag{3.88}$$

which for the system $\{V_{max}, H_{min}\}$ is 100%, and 0 % for $\{V_{min}, H_{max}\}$.

3.9.3 Shannon Entropy Examples

Let's now apply the principle of Shannon Entropy to the same vortex lattice examples introduced previously in Section **3.8.3**.

3.9.3.1 Havelock's Square $(N = 4)$

Consider again Havelock's square. The (four) singular values were given as $\left(\sigma^{(1)}, \sigma^{(2)}, \sigma^{(3)}, \sigma^{(4)}\right) = \left(1/2, \sqrt{2}/2, \sqrt{2}/2, 0\right)$. Squaring and normalizing using Equation (3.84) gives us the probabilities of the system

$$(P_1, P_2, P_3, P_4) = \left(\frac{1}{2}, \frac{1}{4}, \frac{1}{4}, 0\right). \tag{3.89}$$

This gives us a Shannon Entropy of

$$H = -\sum_{\alpha=1}^{N} P_\alpha \ln P_\alpha = -\frac{1}{2} \ln \frac{1}{2} - \frac{1}{4} \ln \frac{1}{4} - \frac{1}{4} \ln \frac{1}{4} = 1.0397. \tag{3.90}$$

Note that the maximum possible entropy for $N = 4$ is $\ln 4 = 1.3863$. Using Equation (3.88), the percentage of information compression for this system 25 %.

Remark 1. Note that the Shannon Entropy of point vortex systems is simply a function of their geometry, and is completely unaffected by the allowable choice of the vortex strengths.

3.9.3.2 Havelock's Square Plus Central Vortex $(N = 5)$

The normalized eigenvalues for this configuration are

$$(P_1, P_2, P_3, P_4, P_5) = \left(\frac{3}{8}, \frac{3}{8}, \frac{1}{4}, 0, 0 \right), \tag{3.91}$$

which gives us an entropy of

$$H = -\sum_{\alpha=1}^{N} P_\alpha \ln P_\alpha = -\frac{3}{8} \ln \frac{3}{8} - \frac{3}{8} \ln \frac{3}{8} - \frac{1}{4} \ln \frac{1}{4} = 0.3890. \tag{3.92}$$

Compared to the maximum entropy for $N = 5$, which is $\ln 5 = 1.6094$, Equation (3.88) tells us that the percentage of information compression for this lattice configuration is 76 %. From this, we conclude that the square lattice without the square $(N = 4)$ has a higher entropy than the lattice with the central vortex $(N = 5)$, which means that the energy is more evenly distributed among the modes when there is no central vortex. This also tells us that for vortices on the Cartesian plane, the configuration without the central lattice has a higher likelihood of existing than does the lattice with the central lattice.

An alternative way for comparing two different systems with the same number of particles (or vortices in our case), is by computing the *Kullback-Leibler divergence* given by [43]. Consider two systems with modal probabilities $P = (P_1, \ldots, P_N)$ and $Q = (Q_1, \ldots, Q_N)$. The value is defined as

$$D_{KL}(P, Q) = \sum_{\alpha=1}^{N} P_i \ln \frac{P_\alpha}{Q_\alpha}. \tag{3.93}$$

An equivalent way of writing the equation is

$$
\begin{aligned}
D_{KL}(P, Q) &= \sum_{i=1}^{N} P_i \ln(P_i) - \sum_{i=1}^{N} P_i \ln(Q_i) \\
&= -\sum_{i=1}^{N} P_i \ln(Q_i) + \sum_{i=1}^{N} P_i \ln(P_i) \\
&= H(P, Q) - H(P),
\end{aligned}
$$

where $H(P, Q)$ is defined as the *cross-entropy* between systems P and Q, and $H(P)$ is simply the Shannon Entropy of P. Such a formulation can be used to contrast two configurations with the same number of vortices.

Note that our application of Shannon Entropy was for systems with one set of events, which for our case corresponded to the set of normalized eigenvalues of AA^T (i.e., $H = H(P(\alpha))$, with $\alpha = 1 \cdots N$). The Shannon Entropy formulation, can be extended to systems in which more than one event can occur simultaneously, for instance if two events can occur simultaneously,

$$
\begin{aligned}
H(x, y) &= -\sum_{\alpha, \beta} P(\alpha, \beta) \ln P(\alpha, \beta), \\
H(x) &= -\sum_{\alpha, \beta} P(\alpha, \beta) \sum_{\beta} \ln P(\alpha, \beta), \\
H(y) &= -\sum_{\alpha, \beta} P(\alpha, \beta) \sum_{\alpha} \ln P(\alpha, \beta).
\end{aligned}
$$

3.10 Matrix Approximation

Matrix Approximation is the third linear algebra tool that we use in our analysis. It is primarily used in Chapter **4** when dealing with asymmetric equilibria. We begin this section by introducing the Frobenius norm.

3.10.1 The Frobenius Norm

The Frobenius norm $\|A\|_F$ gives us a measure of the 'size' of a matrix. It is a function of a matrix's singular values, and is given by

$$\|A\|_F^2 = \left(\sigma^{(1)}\right)^2 + \left(\sigma^{(2)}\right)^2 + \ldots + \left(\sigma^{(r)}\right)^2 \equiv trace(A^T A), \tag{3.94}$$

where r is the rank of covariance matrix $A^T A$. Note also that the 2-norm, $\|A\|_2$ is given by

$$\|A\|_2 = \sigma^{(1)}. \tag{3.95}$$

For instance, the size of Havelock's square configuration without a central vortex is given by

$$\|A\|_F^2 = \left(\frac{1}{2}\right)^2 + \left(\frac{1}{2\sqrt{2}}\right)^2 + \left(\frac{1}{2\sqrt{2}}\right)^2 = \frac{1}{2},$$
$$\|A\|_2 = \frac{1}{2}.$$

Upon adding the central vortex, the size the conguration becomes

$$\|A\|_F^2 = \left(\frac{\sqrt{(3)}}{2\sqrt{2}}\right)^2 + \left(\frac{\sqrt{3}}{2\sqrt{2}}\right)^2 + \left(\frac{1}{2}\right)^2 = 1,$$
$$\|A\|_2 = \frac{\sqrt{3}}{2\sqrt{2}}.$$

Clearly, the configuration with the central vortex is larger than the configuration without the central vortex. We can also express the distance between two matrices A and B from (3.94) as $\|A - B\|_F$.

3.10.2 Reduction

For a given matrix, it might be desirable to reduce its size, given by $\|A\|_F$. This is a process commonly done in graphics and information compression ([22]). Since any non-normal matrix $A \in \mathbb{R}^{M \times N}$ with rank r can be decomposed by Equation (3.62), the matrix can equivalently be expressed as the linear sum of sub-matrices given by

$$A = \sigma^{(1)}\mathbf{u}^{(1)}\mathbf{v}^{(1)T} + \sigma^{(2)}\mathbf{u}^{(2)}\mathbf{v}^{(2)T} + \ldots + \sigma^{(r)}\mathbf{u}^{(r)}\mathbf{v}^{(r)T}, \tag{3.96}$$

or alternatively as

$$A = \sum_{\alpha=1}^{r} \sigma^{(\alpha)}\Lambda^{(\alpha)}, \quad \Lambda^{(\alpha)} = \mathbf{u}^{(\alpha)}\mathbf{v}^{(\alpha)T}. \tag{3.97}$$

The sub-matrix $\Lambda^{(\alpha)}$ is scaled with the corresponding α^{th} singular value, which gives a measure of its size relative to A. A rank-1 approximation entails the removal of the rth term from the summation in Equation (3.97). From an information storage perspective, we have effectively reduced the *size* of our matrix. The net size reduction between A and a rank-1 approximation A_1, is given via the Frobenius norm

$$\|A - A_1\|_F^2 = \left(\sigma^{(r)}\right)^2, \tag{3.98}$$

Note that if $\sigma^{(r)}$ is sufficiently small, we have effectively approximated the matrix with a relatively small loss of information. A generalized rank-k approximation is given by

$$\|A - A_k\|_F^2 = \left(\sigma^{(r)}\right)^2 + \ldots + \left(\sigma^{(r-k+1)}\right)^2. \tag{3.99}$$

We can quantify the amount of information reduction with the ratio

$$\frac{\|A - A_k\|_F}{\|A\|_F} \cdot 100\%. \tag{3.100}$$

Example 1. *(From [41]) Find a rank-one approximation to the matrix*

$$A = \begin{pmatrix} 1 & 1 \\ 0 & 1 \\ 1 & 0 \end{pmatrix}.$$

Begin by decomposing the matrix as in (3.62):

$$U = \begin{pmatrix} \mathbf{u}^{(1)} & \mathbf{u}^{(2)} & \mathbf{u}^{(3)} \end{pmatrix} = \begin{pmatrix} 2/\sqrt{6} & 0 & 1/\sqrt{3} \\ 1/\sqrt{6} & 1/\sqrt{2} & -1/\sqrt{3} \\ 1/\sqrt{6} & -1/\sqrt{2} & -1/\sqrt{3} \end{pmatrix},$$

$$V = \begin{pmatrix} \mathbf{v}^{(1)} & \mathbf{v}^{(2)} \end{pmatrix} = \begin{pmatrix} 1/\sqrt{2} & -1/\sqrt{2} \\ 1/\sqrt{2} & 1/\sqrt{2} \end{pmatrix},$$

$$\Sigma = \begin{pmatrix} \sigma^{(1)} & 0 \\ 0 & \sigma^{(2)} \\ 0 & 0 \end{pmatrix} = \begin{pmatrix} \sqrt{3} & 0 \\ 0 & 1 \\ 0 & 0 \end{pmatrix}.$$

Next, decompose the matrix into the form of Equation (3.97), and make the estimation

$$\begin{aligned}
A_1 &\approx \sigma^{(1)}\Lambda^{(1)} \\
&= \sigma^{(1)}\mathbf{u}^{(1)}\mathbf{v}^{(1)T} \\
&= \sqrt{3} \begin{pmatrix} 1/\sqrt{3} & 1/\sqrt{3} \\ 1/2\sqrt{3} & 1/2\sqrt{3} \\ 1/2\sqrt{3} & 1/2\sqrt{3} \end{pmatrix} \\
&= \begin{pmatrix} 1 & 1 \\ 1/2 & 1/2 \\ 1/2 & 1/2 \end{pmatrix}.
\end{aligned}$$

With Equation (3.99), the change between A and A_1 is $\|A - A_1\|_F = \sigma^{(2)} = 1$. The amount of information reduction from (3.100) becomes

$$\frac{\|A - A_1\|_F}{\|A\|_F} \cdot 100\% = \frac{1}{2} \cdot 100\% = 50\%.$$

Chapter 4. Vortex Lattices on the Plane

In this chapter, we apply the tools from Chapters **2** and **3** to systems of N vortices on the Cartesian plane. The first two of the four main contributions of this thesis are presented in this chapter. The first contribution is the study of asymmetric equilibria, and the second is the application of Shannon Entropy on vortex equilibria. Before we proceed to these main results, a few comparisons to physical lattices will be made in the following section, and at the close of this chapter we will address the reverse problem of Equation (2.49).
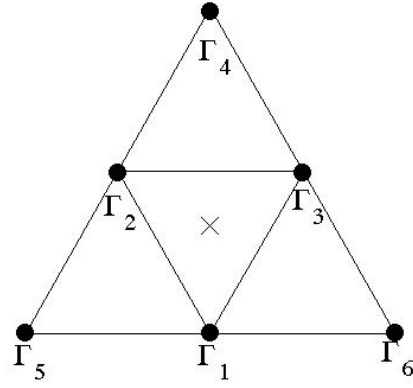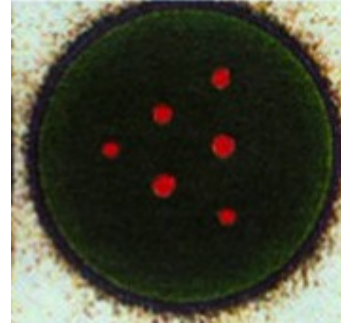
(a) $N = 6$ Triangle Model (b) Plasma Crystal

Figure 4.31: Triangular lattice, $N = 6$. SVD solution produced for configuration was $\mathbf{\Gamma}$ = (-1/4, -1/4, -1/4, 1, 1, 1)^T. System resembles a plasma crystal configuration found in [30]. In (a), center of vorticity is labeled with an $\times$ symbol.

(a) $N = 7$ Semi-circle Model (b) $N = 7$ Hexagon Model

$\omega < 800$ r.p.m. $\omega > 800$ r.p.m.

(c) $N = 7$ Different-Sized Milli-Size Magnets (d) $N = 7$ Uniform-Sized Milli-Size Magnets
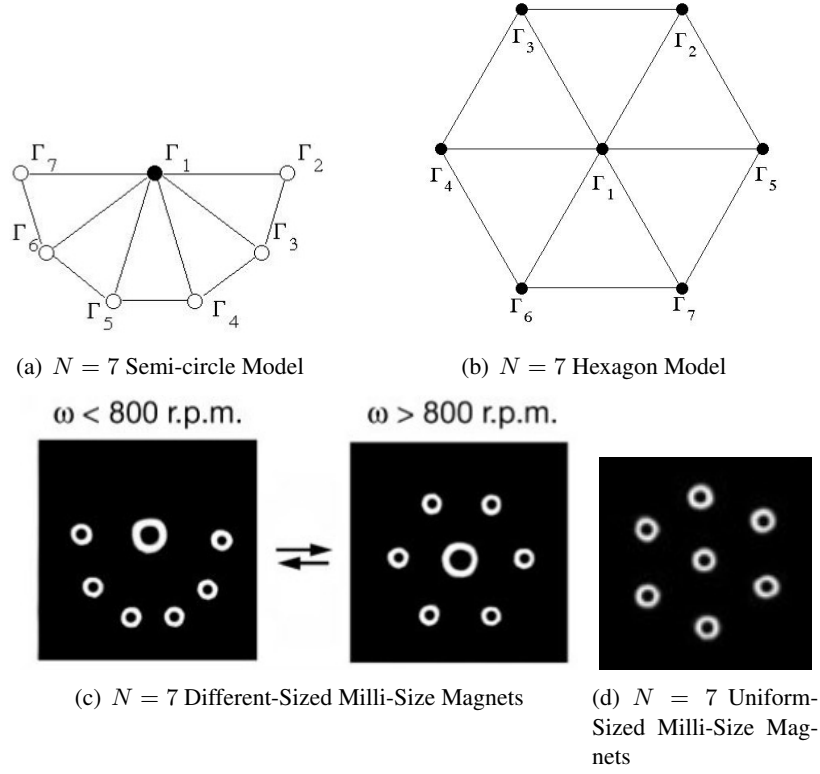
Figure 4.32: Vortex lattices with $N = 7$ vortices. (a) Semi-circle model has null space of one, with $\boldsymbol{\Gamma} = \alpha(1, 0, 0, 0, 0, 0)^T$. This implies that central vortex has arbitrary strength, while remaining 6 vortices on the circle of radius r are stagnation points orbiting the central vortex with velocity $u_\theta = \alpha/2\pi r$. (b) Hexagonal model has non-trivial null space of dimension 2 with $\boldsymbol{\Gamma} = \alpha_1(1,0,0,0,0,0)^T + \alpha_2(0,1,1,1,1,1)^T$ with α_1 and α_2 being unrelated arbitrary constants. This implies that central vortex has one independent strength, while the outer vortices have second independent strengths. (c) Comparison is made to milli-magnetized structures (from [34]) with different-sized magnets. Two configurations arise for different ranges of angular velocity (as denoted in figure), and we compare them to models (a) and (b) which support different-strength vortices with the selection $\alpha_1 \neq \alpha_2 \neq 0$. (d) Uniform-sized milli-magnetized structures. Comparison is made to (b), since the solution to (b) can support uniform-strength vortices with the selection $\alpha_1 = \alpha_2$. Center of vorticity coincides with location of central vortex.

4.11   Comparison to Physical Lattices

Figure 4.31 is a triangular lattice with $N = 6$, and the comparison is made to the plasma lattice in Figure 1.12 ([23]). Note that this configuration also appears in the milli-magnets on the curved water drop surface in Figure 1.11 from [34]. The configuration was formulated as in (2.49), and a solution satisfying (2.50) was found. The dimension of the null space for this configuration is

(a) $N = 19$ Double Hexagon Model

(b) Superfluid lattice
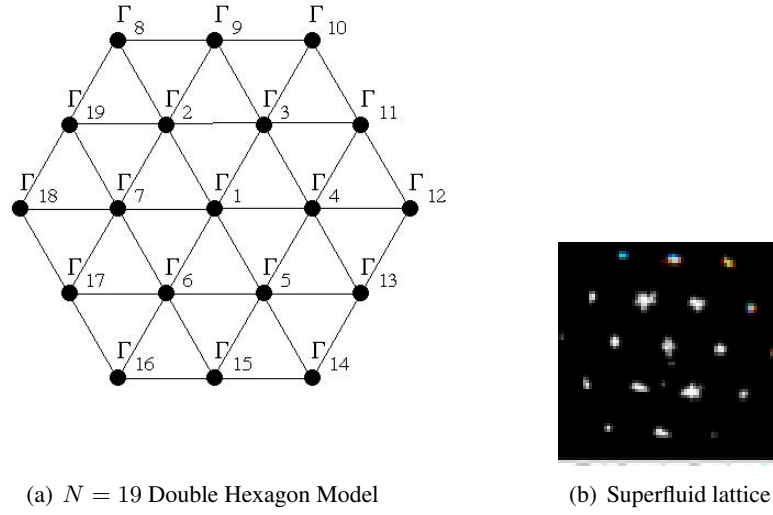
Figure 4.33: Triangular vortex lattice, $N = 19$ with solution. Lattice consists of two concentric hexagonal rings. Solution to system can be found in Equation (4.101).

1 (i.e., $\sigma^{(6)} = 0$). From Equation (3.68), the three outer corner vortices have equal strengths to one another; the three inner vortices have equal strengths to one another and are one-fourth as strong as the outer vortices with opposite circulation.

The milli-sized magnets in Figure 1.11(b) possess two special features ([34]). First, the magnets have different sizes (we interpret different-sized magnets as having different vortex strengths). Second, more than one configuration geometry occurs for the same number of magnets. In Figure 4.32, we specifically modeled the two geometry types for the case $N = 7$, and implemented Equation (2.49). The first model presented in Figure 4.32(a) is of a configuration consisting of a central vortex coupled with six vortices evenly spaced along a semi-circle centered at the central vortex. The SVD solution yields a null space of one for this configuration given by $\mathbf{\Gamma} = \alpha(1, 0, 0, 0, 0, 0)^T$. This tells us that the central vortex has arbitrary strength α, while the six vortices on the semi-circle have zero strength, and are passive non-rotating particles being advected around the central vortex with constant angular speed $u_\theta = \alpha/2\pi r$, where r is the radius of the semi-circle. Note that for any $\alpha \neq 0$, this model's vortex strength distribution agrees with magnet size distribution in Figure 4.32(c) when $\omega < 800$ r.p.m.. The second

geometry type is presented in 4.32(b). It consists of a central vortex and six vortices distributed evenly about a full circle around the central vortex, resulting in a hexagonal structure. The SVD solution to this model returns a solution with a null space of two with Equation (3.68), being $\Gamma = \alpha_1(1,0,0,0,0,0)^T + \alpha_2(0,1,1,1,1,1)^T$, where α_1 and α_2 are independent and unrelated arbitrary constants. This model agrees with the different-sized magnetic system of Figure 4.32(c) ($\omega > 800$ r.p.m) for the selection $\alpha_1 \neq \alpha_2$, as well as the uniform-sized magnet system illustrated in 4.32(d) for the selection $\alpha_1 = \alpha_2$.

In Figure 4.33, we have a full numerical solution to a configuration with two radially concentric hexagonal rings−containing 19 vortices in total (1 central vortex, 6 vortices in the inner hexagonal ring, and 12 in the outer hexagonal ring). The SVD method's solution found that the null space of this configuration is 2. In Equation (4.101) below, horizontal lines in the vector distinguish the central vortex (top-most entry), the inner-hexagon vortices (next set of six entries), and the outer-hexagon vortices (remaining twelve entries). The solution is given by

$$\mathbf{\Gamma} = \begin{pmatrix} \Gamma_1 \\ \Gamma_2 \\ \vdots \\ \Gamma_7 \\ \hline \Gamma_8 \\ \Gamma_9 \\ \Gamma_{10} \\ \Gamma_{11} \\ \Gamma_{12} \\ \Gamma_{13} \\ \Gamma_{14} \\ \Gamma_{15} \\ \Gamma_{16} \\ \Gamma_{17} \\ \Gamma_{18} \\ \Gamma_{19} \end{pmatrix} = \alpha_1 \begin{pmatrix} +7/6 \\ -1/6 \\ \vdots \\ -1/6 \\ \hline 1 \\ 0 \\ 1 \\ 0 \\ 1 \\ 0 \\ 1 \\ 0 \\ 1 \\ 0 \\ 1 \\ 0 \end{pmatrix} + \alpha_2 \begin{pmatrix} 5/9 \\ 3/7 \\ \vdots \\ 3/7 \\ \hline 0 \\ 1 \\ 0 \\ 1 \\ 0 \\ 1 \\ 0 \\ 1 \\ 0 \\ 1 \\ 0 \\ 1 \end{pmatrix} . \tag{4.101}$$

The corner vortices of the outer ring share a common strength of α_1; the mid-edge vortices of the outer ring share a different common strength of α_2; the vortices of the inner ring all share a single strength which is a linear combination of the strength of the outer ring's corner and mid-edge vortices $((-1/6)\alpha_1 + (3/7)\alpha_2)$. Finally, the strength of the central vortex is also a linear combination of the strength of the outer ring's corner and mid-edge vortices $((7/6)\alpha_1 + (5/9)\alpha_2)$. The micro-scale image in the figure is of a superfluid vortex crystal that possesses the same type of radial hexagonal structure.
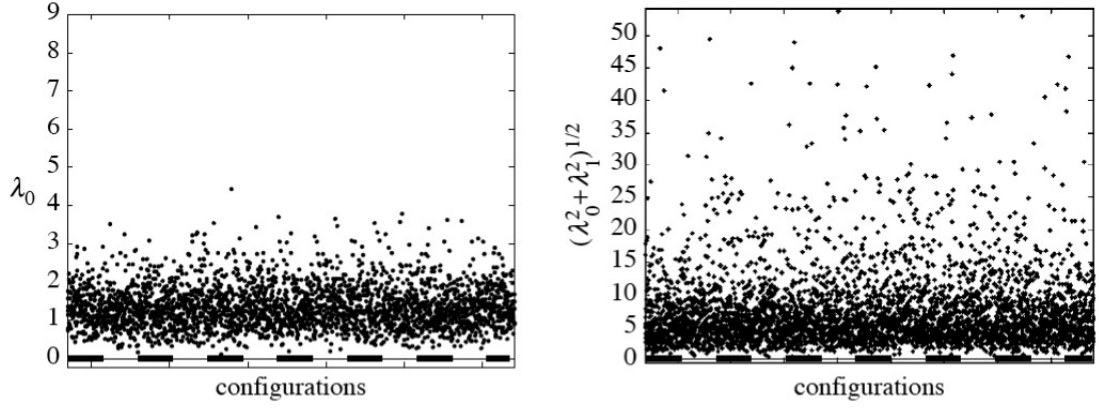
Figure 4.34: Left: minimum eigenvalues of 10^6 random configurations, $N = 10$ (None are in equilibrium). Right: square root of sum of the squares of two smallest eigenvalues of 10^6 random configurations, $N = 10$ (None have a null-space of two).

4.12 Asymmetric Equilibria

The study of asymmetric equilibria corresponds to the first main contribution of this thesis, which will be fleshed out in the following subsections.

4.12.1 Existence

In the former section, we only made comparisons to symmetric lattices. As was discussed in Section **1.3.2** of the introduction (see Figures 1.6 and 1.7), vortex lattices with broken symmetries also exist in nature, see Figure 4.35 from [1]. In the investigation asymmetric equilibria, we began by depositing a finite number of point vortices at random from a uniform distribution in the compact planar region $x \in (-1, 1), y \in (-1, 1)$. Next, the configuration matrix from Equation (2.49) was derived, and the minimum eigenvalue of the covariance square matrix $A^T A$ satisfying (3.64) was found. If the smallest eigenvalue is a non-zero number, then the matrix A has full rank and (2.50) is not satisfied. This implies that the configuration has only a trivial equilibrium solution (i.e., $\mathbf{\Gamma} = \mathbf{0}$).
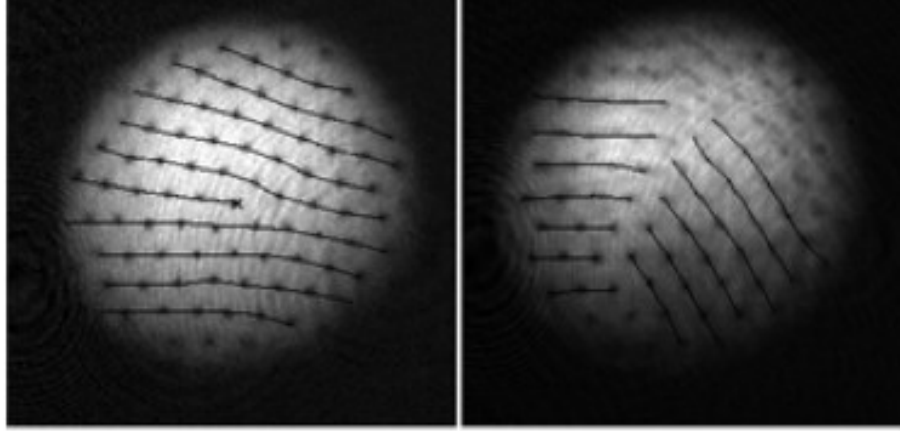
Figure 4.35: Broken symmetries in triangular lattices of Bose Einstein Condensates. Left: Line defect. Right: Grain boundary defect (from [1]).

A million random configurations containing $N = 10$ vortices were generated, and their covariance matrices' minimum eigenvalues were computed. Figure 4.34 shows that the minimum eigenvalue associated with all 10^6 random configuration is *always* non-zero, indicating that an asymmetric configuration with a non-trivial equilibrium cannot be chosen at random, and these configurations form a set of measure zero in the space of all possible configurations. Also from Figure 4.34, we conclude that a configuration with a null space of two is even less likely to be chosen at random. In the next section, an algorithm that utilizes the minimum singular value as a scaling factor to drive the random asymmetric configuration to a converged non-trivial equilibrium is introduced.

4.12.2 The Brownian Ratchet

Recall from Figures 1.6 and 1.7 from Section **1.3.2**, that when a regular triangular lattice was blasted by a laser, the vortices exhibited an apparently random motion that resembled a thermal cooling process which eventually homed in on a new irregular / asymmetric equilibrium configuration ([26]). (Another good example with lattices with broken symmetries is illustrated in Figure 4.35). The Brownian ratchet method starts off with a random configuration of N vortices. Using the SVD method, the ratchet process has the following algorithm:
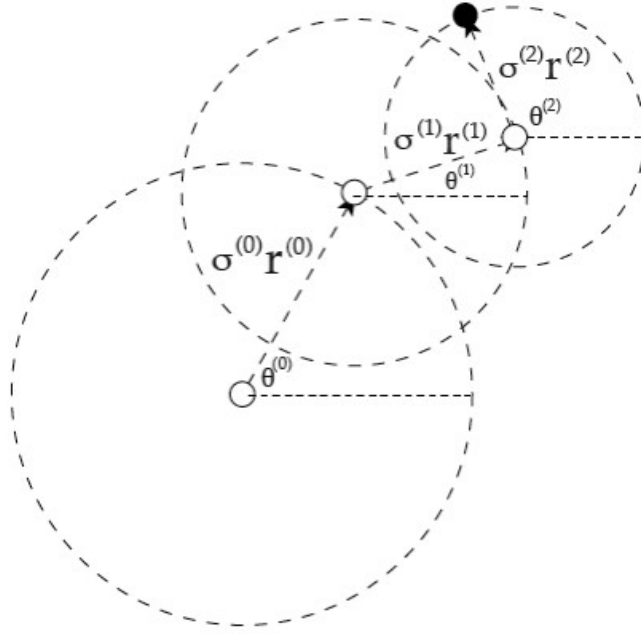
Figure 4.36: Schematic of the Brownian ratchet method. The vortices take a random walk, each within a circle scaled with the smallest singular value, $\sigma^{(0)}$ associated with its configuration matrix until the smallest singular value gets smaller , $\sigma^{(1)}$. The vortices continue to take random walks in circles of ever decreasing radius until the smallest singular value drops below a prescribed threshold.
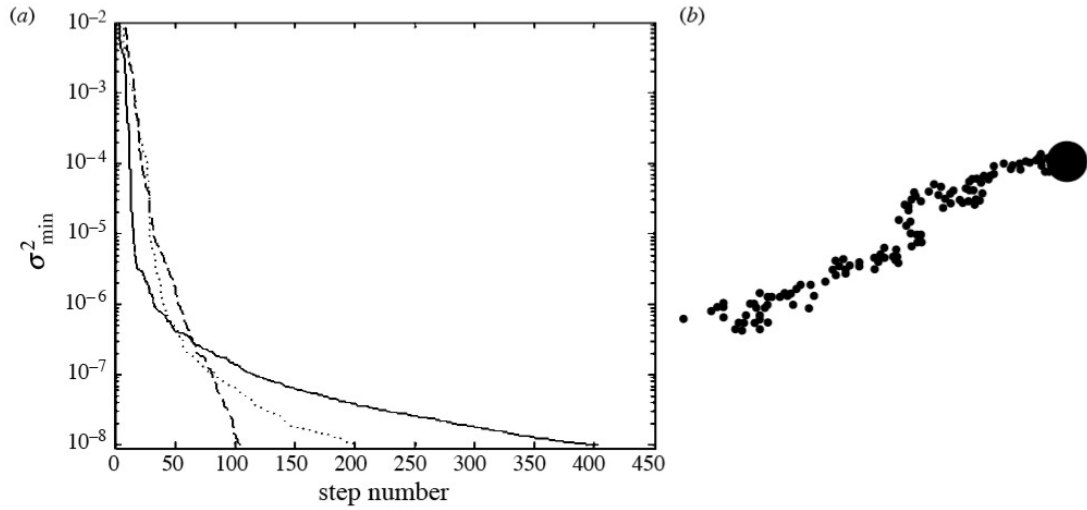
Figure 4.37: (a): Smallest singular value squared vs. Brownian ratchet step number on lin-log scale for $N = 6, 8, 10$. The smallest singular value converges continuously to zero. (b): Close-up view of a vortex converging to an equilibrium point, scale is magnified $\times 10^6$ the scale of configuration.
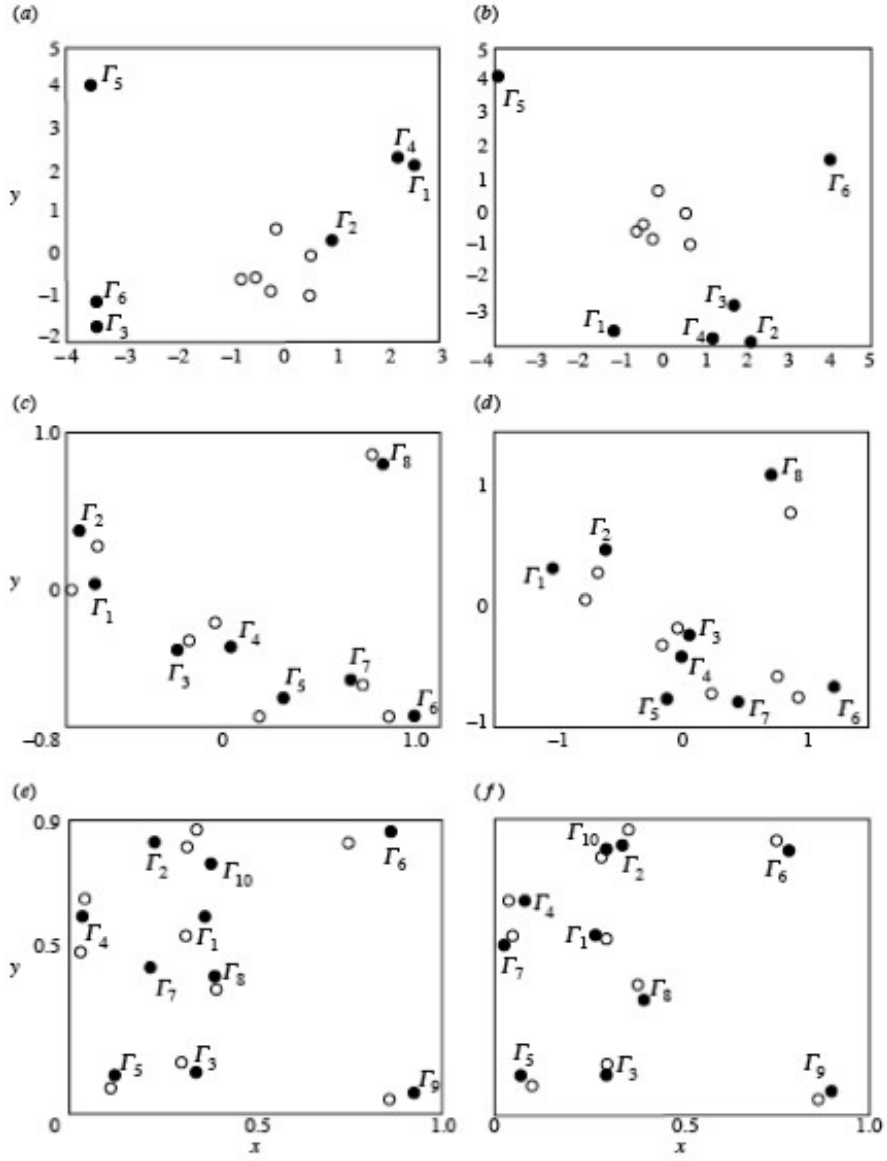
Figure 4.38: Examples of converged asymmetric equilibrium configurations with one-dimensional null spaces using Brownian ratchet method. Total of six plots for 6, 8, 10 vortices, with one initial configuration (unfilled circles) and two corresponding final converged states (filled circles) with smallest singular value on the order of 10^{-6}. (a) $N = 6$, $\Gamma = (0.0040, -0.0033, -0.0254, -0.0079, -0.9996, -0.0001)^T$; (b) $N = 6$, $\Gamma = (-0.2394, -0.1049, 0.1078, 0.0314, 0.7461, -0.6020)^T$; (c) $N = 8$, $\Gamma = (0.0064, -0.0221, -0.0743, 0.0456, 0.1197, -0.1380, 0.0751, -0.9761)^T$; (d) $N = 8$, $\Gamma = (0.0040, -0.0033, -0.0254, -0.0079, -0.9996, -0.0001)^T$; (e) $N = 10$, $\Gamma = (-0.0364, -0.0666, -0.0253, -0.0335, -0.1392, -0.5016, -0.0716, 0.0163, -0.8462, 0)^T$; and (f) $N = 10$, $\Gamma = (0.1561, 0.0048, 0.0970, -0.0078, 0.1108, 0.2844, -0.0047, -0.0410, 0.9334, 0.0004)^T$.
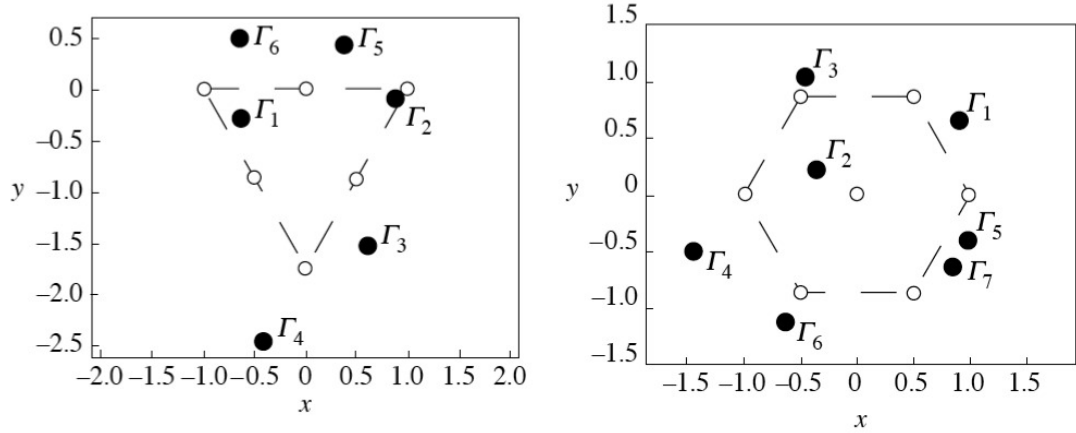
Figure 4.39: Reverse Brownian ratchet scheme used to derive initial random configuration not in equilibrium from symmetric equilibrium configurations. (a) $N = 6$ triangular configuration with null-space 1 in open circles, with random non-equilibrium configuration that converges to it. (b) $N = 7$ hexagonal equilibrium configuration with null space 2 in open circles, with random non-equilibrium configuration that converges to it.

1. We identify the smallest singular value $\sigma_{min}^{(0)}$ associated with A.

2. The vortices are then randomly fluctuated—each within a circle that is scaled with $\sigma_{min}^{(0)}$. During this fluctuation, the singular values of the 'fluctuated' configuration also fluctuate, and we continuously monitor the smallest singular value associated with the fluctuated configuration, σ'_{min}.

3. As soon as σ'_{min} becomes smaller than $\sigma_{min}^{(0)}$, we consider that we have converged one step closer to an equilibrium, and the fluctuation is paused. The current configuration is saved as the new one, and the smallest singular value now becomes $\sigma_{min}^{(1)} = \sigma'_{min}$.

4. The random fluctuation recommences, and is repeated for each of the vortices, but this time within a *smaller* circle scaled with the new smallest singular value $\sigma_{min}^{(1)}$. This process is repeated K times until $\sigma_{min}^{(K)}$ drops below a prescribed threshold $\delta_{thresh} \approx 10^{-6}$.

Figure 4.36 provides a schematic of the Brownian ratchet's convergence process. In Figure 4.37, we track the square of the smallest singular value of A as the Brownian ratchet step number increases, and we show that it converges continuously to zero. Also in that figure, a close-up

image that is magnified to a millionth the area of the overall configuration shows the convergence process of a single vortex with individual ratchet steps. Figure 4.38 illustrates configurations of vortices that converged to an asymmetric equilibrium with a null space of 1. The important results here are that

1. Asymmetric equilibria do exist.

2. An initial configuration not in equilibrium will converge to completely different asymmetric equilibrium configurations each time the ratchet is repeated (i.e., there are many neighboring equilibrium configurations, possibly lying arbitrarily close to one another).

3. It is quite curious that configurations always numerically converge to purely asymmetric patterns as did the Bose-Einstein condensates upon being blasted by a laser. Hence, the Brownian ratchet scheme appears to have a convergence bias towards asymmetric, rather than symmetric configurations.

Figure 4.39 uses a reverse Brownian ratchet process to show that a configuration can in theory converge to a symmetric configuration, and can also converge to a configuration with a null space greater than one.

4.12.3   Distance to Equilibrium

The next natural question to ask is: how close is the nearest equilibrium to a random configuration? In other words, the question is whether the set of asymmetric equilibrium configurations is dense in the broader set of asymmetric configurations. The comparison is made to rational and irrational numbers on the real line. Both rational and irrational numbers are dense in the sense that a rational number exists between any two irrational ones, and an irrational number exists between any two rational ones. That is, a rational number is arbitrarily close to an irrational one. The difference between the two is that, if a number is picked at random from the real number line, it will always be an irrational number. Therefore, irrational numbers form a full-measure set, while the rational numbers have measure zero on the real line. The question now

Table 4.1: Converged Brownian ratchet configurations of Figure 4.38 with (i) the Frobenius size of the converged equilibrium configuration, (ii) distance to exact equilibrium, (iii) Hamiltonian energy and (iv) the distance between the two converged configurations that had the same initial conditions.

N	$\|A_{final}\|_F$	$\|A_{init} - A_{final}\|_F$	$\mathcal{H}$	$\|A_1 - A_2\|_F$
$N = 6(a)$	53.6412	3.15×10^{-05}	-0.0047	59.0357
$N = 6(b)$	23.4493	6.14×10^{-06}	0.0816	59.0357
$N = 8(a)$	22.0578	1.00×10^{-05}	-0.0104	55.5116
$N = 8(b)$	51.4244	9.99×10^{-06}	-0.05100	55.5116
$N = 10(a)$	22.0578	9.96×10^{-06}	0.0166	51.0580
$N = 10(b)$	44.6184	9.99×10^{-06}	0.0157	51.0580

is whether randomly deposited vortices (that are always not in equilibrium) can be compared to the irrational numbers, while the converged asymmetric configurations (with null space one) can be compared to rational numbers. The answer to this question is no. The 'minimum distance' between a rectangular matrix A_0 with full rank to a rank-1 deficient matrix A_1 (i.e., the smallest singular value is zero) is given via the Frobenius norm in (3.94) as equal to the smallest singular value $\sigma(N)$: Since A_0 is not rank deficient, this distance is not arbitrarily small. The Frobenius norm tells us that an asymmetric equilibrium configuration does not lie arbitrarily close to a random configuration, but rather has a minimum and finite distance to it, namely $\sigma_{min} \equiv \sigma(N)$. In other words, the rank-1 deficient matrix A_1 is also the *closest* equilibrium to full rank matrix A_0.

Tables 4.1 and 4.2 contain a set of numerical information associated with the converged equilibria of Figure 4.38. The matrix A_{init} corresponds to the converged configuration, A_{final} corresponds to the equilibrium approximation, and $\|A_{init} - A_{final}\|_F$ is the converged configuration's closest distance to a configuration whose minimum singular value is exactly zero.

Remark 2. Consider two configuration matrices A and B such that their dimensions are the same. If $\|A\|_F = \|B\|_F$, we conclude that A and B correspond to configurations of the same *size*, but in general the configurations can foreseeably have different locations, or even different geometries, whereas if $\|A - B\|_F = 0$, we conclude that the two matrices have the same size

Table 4.2: Singular values of converged Brownian ratchet configuration of Figure 4.38.

N	σ's
$N = 6(a)$	$(36.8899, 34.0091, 16.8357, 8.0756, 3.3529, 3.15 \times 10^{-05})$
$N = 6(b)$	$(16.4495, 15.1967, 6.6437, 2.0431, 0.1741, 6.42 \times 10^{-06})$
$N = 8(a)$	$(11.8714, 11.344, 9.347, 8.4775,$ $5.43, 4.5957, 2.6626, 1.00 \times 10^{-05})$
$N = 8(b)$	$(34.6657, 34.5454, 11.1811, 9.6584,$ $4.1464, 2.9317, 2.2993, 9.99 \times 10^{-06})$
$N = 10(a)$	$(13.2665, 12.1482, 10.7102, 8.7633, 7.4807,$ $5.1647, 4.7517, 2.4412, 0.8549, 9.96 \times 10^{-06})$
$N = 10(b)$	$(28.3155, 27.8314, 12.5556, 10.5146, 7.3477,$ $7.1772, 5.1661, 3.6358, 0.9141, 9.99 \times 10^{-06})$

and, if each configuration matrix corresponds to a single unique configuration, that the vortices of A and B have the same relative locations as well, with respect to rotations and translations.

4.13   Shannon Entropy

We now move our focus to the second main contribution of this thesis: Shannon Entropy. We claim that this measure can predict the likelihood of formation for a given lattice geometry in the physical systems referenced in the introduction (plasma lattices, magnetic lattices, helium lattices). We begin the analysis by comparing two configurations that have the same number of vortices, but different inter-vortical distances.

For four-vortex equilibra, we compare the square configuration in Section **3.8.3.1** to an equilateral triangle lattice with a central vortex. The square configuration is more prevalent than the equilateral triangle configuration (Figures 1.2 and 1.10). As it turns out, the Shannon Entropy from Equation (3.82) of the square configuration is $H \approx 1.0397$, while that of the triangle is $H \approx 0.6931$. Therefore, the square configuration has a higher entropy, and arguably, a higher *likelihood* to exist. Note also that from Equations (2.40) and (3.68) that the square configuration has a lower Hamiltonian energy. For five-vortex equilbria, consider the pentagon configuration (5 vortices evenly distributed on a circle) and the Havelock's square with a central vortex (see

(a) Normalized eigenvalues of $A^T A$ (b) Shannon Entropy
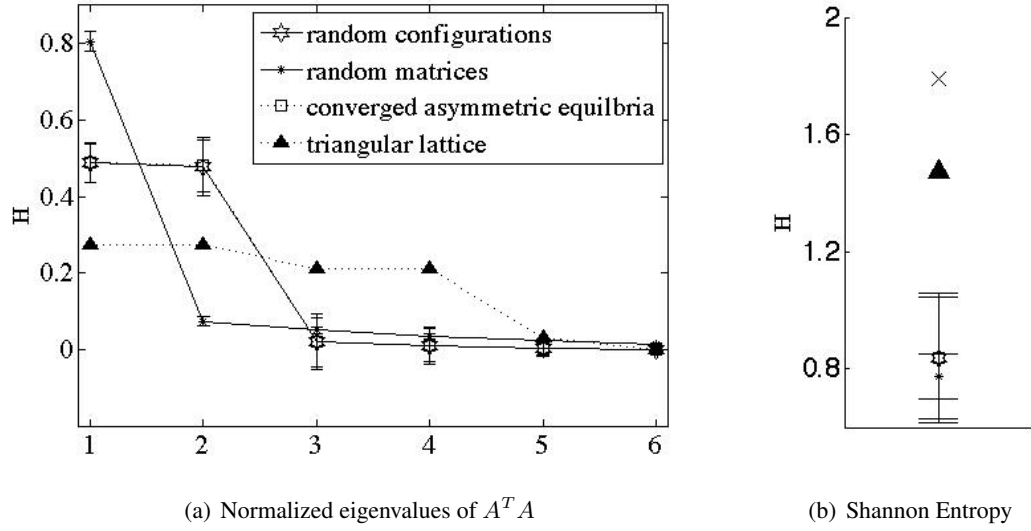
Figure 4.40: Averaged 250 times + standard deviation. Comparison of Shannon Entropy associated with: random asymmetric configurations (not in equilibrium), random matrices (all entries are random numbers), converged asymmetric equilibria with null space 1, and the triangle lattice from Figure 4.31. Triangle lattice has significantly higher entropy than asymmetric equilbria, with entropy of asymmetric configurations not in equilibrium and in equilibrium being indistinguishable from one another within standard deviation. Random matrices have substantially lower entropy than any configuration matrix.

the example in Section **3.8.3.2**). The pentagon configuration is more prevalent in the referenced physical systems than the square lattice with a central vortex (Figures 1.2, 1.10 and 1.12). The Shannon Entropy of the pentagon configuration is $H \approx 1.3662$, while that of the square configuration is $H \approx 0.3890$. Again, the configuration that is more prevalent in physical systems has the higher entropy. Comparing the Hamiltonian of these two configurations is not as clear-cut, since the dimension of the null space for the square lattice with a central vortex is two. This makes the Shannon Entropy analysis more definitive in this case since it relies solely on the system's geometry, and not its null space (i.e., relative vortex strengths). An interesting observation is that the square lattice with a central vortex appears to be the most likely geometry type on the curved surface in Figure 1.11. This tells us that the entropy of a given configuration may change with its surface's curvature.

In Figure 4.40, four sets of matrix modal probabilities (i.e., normalized squared eigenvalues of $A^T A$) corresponding to different geometry types are computed and compared. Namely

these four include: averaged probabilities of 250 random configurations (not in equilibrium), averaged probabilities from random matrices (all elements chosen from uniform distribution), probabilities of 250 converged asymmetric equilibria (via the Brownian ratchet), and the probabilities of the triangular lattice from Figure 4.31. The triangular lattice comparatively had the highest entropy of all. This supports the claim that higher entropy equates to higher likelihood for existence, since triangular geometries are the most common configuration types found in many different lattice types (specifically in Figure 1.12). It is important to note that asymmetric configurations both in equilibrium and not in equilibrium had indistinguishable entropies. This could be due to the fact that the Brownian ratchet searches for equilibria in the vicinity of the initial configuration, and can in theory, home in on a configuration within the same entropy range. In the context of Figure 1.6, in which a regular triangle lattice converged to an asymmetric equilibrium after the blast, it is foreseeable from the distribution in Figure 4.40, that the Shannon Entropy is *quantized*. In other words, after the laser blast the entropy of the system changed. The Brownian ratchet's search can be broadened or condensed (i.e., the vortices can be controlled to fluctuate within circles of variable radius), and this potentially could have an effect on the standard deviation of the entropy when averaged over many runs. We will revisit Shannon Entropy in Chapters **5** and **6** in the context of vortex streets on the sphere.

4.14   The Reverse Problem

With the closing of this chapter, we pose the question: can a single configuration matrix correspond to more than one configuration? Moreover, looking at the problem in reverse: can a configuration be derived from a configuration matrix? And if so, can a single configuration matrix correspond to more than one configuration? A scenario in which the answer to the latter is yes was found. For the case $N = 3$, the associated configuration matrix has three columns and $3(2)/2 = 3$ rows. Consider a zero matrix A_0 with the same dimensions as a system with $N = 3$ vortices (i.e., $A_0 \in \mathbb{R}^{3 \times 3}$). This implies that either (a) all the intervortical distances are equal, or that (b) the intervortical area is zero. The first corresponds to an equilateral triangle,

and the second corresponds to three collinear vortices. Therefore, it was possible to identify two configurations that correspond to a single configuration matrix. This can be thought of as a degenerate scenario, so in the next subsections, the combinatorial structures of the configuration and configuration matrices will be studied and compared in order to provide a more general answer for non-degenerate scenarios.

4.14.1   Configuration Construction With and Without a Coordinate System

In the presence of a coordinate system, a minimum of $2N$ values are required to fully characterize a system of N points in the plane (i.e., (x_α, y_α) or $(r_\alpha, \theta_\alpha)$, where $\alpha = \{1, \ldots, N\}$). In the absence of a coordinate system, one way to construct a configuration is with the use of relative distances $l_{\alpha\beta}$ ($\alpha = \{1, \ldots, N-1\}$ and $\beta = \{\alpha + 1, \ldots, N\}$) and relative orientations $\epsilon_{\alpha\beta\lambda}$ ($\alpha = \{1, \ldots, N-2\}, \beta = \{\alpha + 1, \ldots, N-1\}$ and $\lambda = \{\beta + 1, \ldots, N\}$) .

Let's begin by choosing the relative distances between point 1 and points $\alpha = \{2, \ldots, N\}$. These distances can be chosen arbitrarily such that $l_{1\alpha} > 0$, and this gives us a total of $N-1$ independent values (Figure 4.41(a)). Next, we consider the distances $l_{2\beta}$ between point 2 and the remaining $N-2$ points defined as $\beta = \{3, \ldots, N\}$. Since l_{12} and $l_{1\beta}$ have already been defined, the distance $l_{2\beta}$ is constrained by $|l_{12} - l_{1\beta}| < l_{2\beta} < |l_{12} + l_{1\beta}|$, see Figure 4.41(b) for an illustration of this constraint. This gives us an additional $N-2$ values. Finally, the relative orientation between vortices 1, 2 and β ($\beta = \{3, \ldots, N\}$) can be chosen to be $\epsilon_{12\beta} = \pm 1$; this gives us an additional $N-2$ values. Note that a triangle with lengths l_{12}, l_{13}, l_{23} can either have relative orientation $\epsilon_{123} = +1$ or $\epsilon_{123} = -1$. The two possible orientations give us two geometrically different triangles with respect to rigid rotations—see Figure 4.41(c) for a schematic of this.

The remaining relatives distances $l_{\alpha\beta}$ with $\alpha = \{3, \ldots N-1\}$ and $\beta = \{\alpha + 1, \ldots N\}$, and orientations ($\epsilon_{\alpha\beta\lambda}, \alpha = \{1, \ldots, N-2\}, \beta = \{3, \ldots, N-1\}$ (with $\beta > \alpha$), and $\lambda = \{\beta + 1, \ldots, N\}$) between the points are *fully determined*. The area between any three points in the configurations ($A_{\alpha\beta\lambda}$) can then be solved using the relative distances and orientations.

Table 4.3: Comparison of the minimum number of data points required to construct a configuration of N points in the plane in: (a) the presence of a coordinate system, and (b) in the absence of a coordinate system. Note that for $N < 5$, less values are required to construct the system in the absence of a coordinate system, for $N = 5$ the number of values is the same, and for $N > 5$, less values are required in the presence of a coordinate. The last column demonstrates the number of non-trivial entries in configuration matrix A associated with different N.

Number of points	With coordinate system	Without coordinate system	Non-trival entries in A
N	$2N$	$3N - 5$	$N(N-1)(N-2)/2$
$N = 2$	2	1	0
$N = 3$	6	4	2
$N = 4$	8	7	8
$N = 5$	10	10	20
$N = 6$	12	13	40
$N = 7$	14	16	70
$N = 8$	16	19	168

Therefore, in the absence of a coordinate system, a total of $3N - 5$ values are required to fully characterize the system, see Table 4.3.

4.14.2 Number of Elements in the Configuration Matrix

For a general configuration, A has $N - 2$ non-trivial entries per row (recall that each row is associated with the rate of change of the relative distance between two unique vortices $\alpha = \{1, \ldots, N-1\}$ and $\beta = \{\alpha + 1, \ldots, N\}$, and the non-trivial entries correspond to the entries where $\lambda \neq \alpha, \lambda \neq \beta$). With $N - 2$ non-trivial entries per row and a total of $N(N-1)/2$ rows, in general we will have a total of $N(N-1)(N-2)/2$ non-trivial matrix entries. The non-trivial entries of A are a function of the configuration's intervortical lengths, orientations and areas. As described in the previous section, there are $3N - 5$ unique independent values that describe the coordinate-free configuration. The reverse problem remains an open question since the analysis in this section is not fully conclusive. However, using the information presented, we can conclude whether the configuration matrix is over-determined or under-determined for different values of N (Table 4.3).
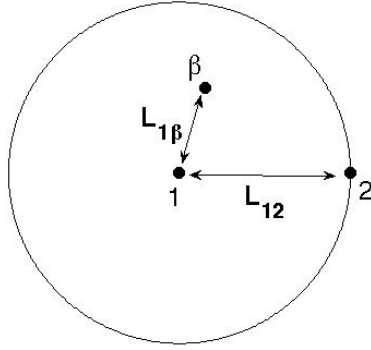
(a) Relative Distances $l_{12}, \ldots, l_{1\beta}$
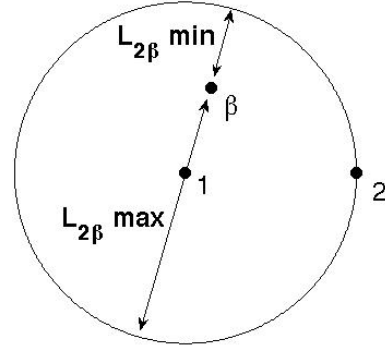
(b) Relative Distance $l_{2\beta}(\min) < l_{2\beta} < l_{2\beta}(\max)$
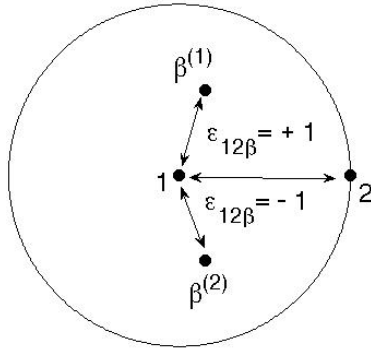
(c) Relative Orientation $\epsilon_{12\beta} = \pm 1$
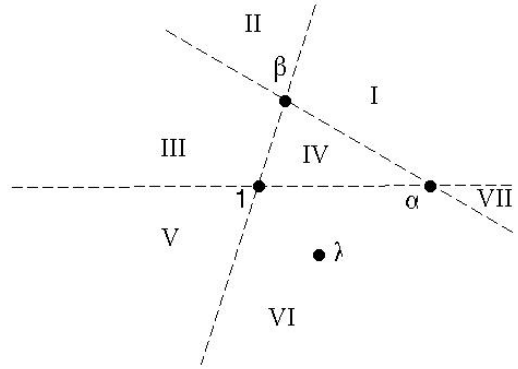
(d) Identification of Remaining Points

Figure 4.41: Configuration Construction of N points in the plane in the absence of a coordinate system. (a) $N - 1$ relative distances from point 1 can all be chosen independently from $\mathbb{R}^+$, (b) $N - 2$ relative distances from point 2 to $\beta = \{3, \ldots, N\}$ can be chosen from the constricted range $|l_{12} - l_{1\beta}| < l_{2\beta} < |l_{12} + l_{1\beta}|$, (c) $N - 2$ Relative orientations between points 1, 2 and $\beta = \{3, \ldots, N\}$ can be chosen to be $\epsilon_{12\beta} = \pm 1$. This subfigure highlights the fact that the two possible choices for $\epsilon_{12\beta}$ result in two geometrically unique configurations (i.e., one configuration cannot be obtained from the other via rigid body rotations and translations), with vortex β either having the relative position $\beta^{(1)}$ or $\beta^{(2)}$, (d) The information corresponding to the remaining points, labeled $\lambda = \{\beta + 1, \ldots, N\}$, can be solved analytically by identifying their locations (in Regions I - VII) relative to three preceding fully-solved points $\{1, \alpha, \beta\}$, such that $\alpha < \beta$, $\beta < \lambda$ and $\lambda \leq N$.

Chapter 5. Single Von Kármán Streets on the Sphere

In this chapter, we move our focus to single vortex streets on the sphere. From the four main contributions of this thesis (outlined in Section **1.2** of the introduction), three are present in this chapter. First, this chapter includes a derivation of the analytic solution to the single street using the center of vorticity and angular velocity equations. Second, we will flesh out the streamline topology and bifurcations for this class of configurations, and third, we will apply the Shannon Entropy formulation. The analysis is repeated for configurations with and without vortices at the poles.

5.15   Construction and SVD Solution

5.15.1   Without Pole Vortices

In this subsection, we investigate the existence of single von Kármán streets (VKS) consisting of two symmetrically skewed n-vortex rings without pole vortices. That is, we write (2.60) for a total of $N = 2n$ vortices on the sphere as illustrated in Figure 5.42, and seek configurations satisfying (2.50). Admissible solutions are those that also satisfy the VKS requirement, that is, two rings of vortices with equal and opposite strength that rotate rigidly about a fixed center of vorticity axis.
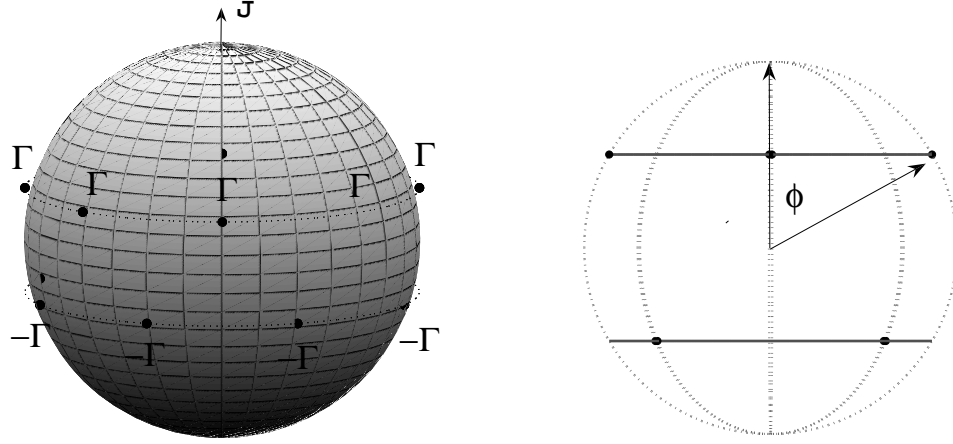
Figure 5.42: Schematic of a single von Kármán street on the sphere with an illustration of the vorticity vector **J** and the angle ϕ.

5.15.1.1   Number of Vortices Per Ring: $n \neq 3$

We first consider configurations containing $n = 2, 4, 5, 6, 7, \dots$ (excluding 3) vortices per ring. As an example, the configuration matrix for the case $n = 2$, using Equation (2.49) becomes

$$
A_2 = \begin{pmatrix}
a_2 & 0 & a_2 & 0 \\
-a_2 & 0 & 0 & -a_2 \\
0 & -a_2 & -a_2 & 0 \\
0 & a_2 & 0 & a_2 \\
0 & 0 & 0 & 0 \\
0 & 0 & 0 & 0
\end{pmatrix},
\tag{5.102}
$$

where $a_2 = a_2(\phi)$, and ϕ is the co-latitude of the ring in the Northern hemisphere (Figure 5.42). In our notation, the subscript associated with a configuration matrix and its entries' names corresponds to n. The entry a_2 is given by

$$
a_2 = -\frac{\cos\phi \left(3\cos^2\phi - 1\right)}{2(\cos^2\phi + 1)}.
\tag{5.103}
$$

Note that a_2 is the only unique non-trivial entry in A_2 associated with the case $n = 2$ (In general, there are multiple distinct non-trivial entries when $n \geq 4$ in the configuration matrix. For example, in the configuration matrix associated with $n = 4$, one finds 9 distinct entries which would be labeled $a_4, b_4, c_4, \ldots, i_4$.). From (3.62), the singular values of (5.102) are

$$\sigma_2 = \begin{pmatrix} 2\sqrt{2}a_2, & 2\sqrt{2}a_2, & 2a_2, & 0 \end{pmatrix}^T . \tag{5.104}$$

Since one of the singular values is zero, the null space of this configuration is one (i.e., $nullity(A_2) = 1$). From (3.68) the solution to this configuration has the general form

$$\boldsymbol{\Gamma} = \Gamma \begin{pmatrix} 1, & 1, & -1, & -1 \end{pmatrix}^T . \tag{5.105}$$

This solution can be generalized, and the general form of $\boldsymbol{\Gamma}$ for any $n \neq 3$ becomes

$$\boldsymbol{\Gamma} = \Gamma \begin{pmatrix} 1, & \ldots, & 1, & -1, & \ldots, & -1 \end{pmatrix}^T , \tag{5.106}$$

where $\boldsymbol{\Gamma}$ has length $2n$, with the first and second set of n vortices corresponding to upper (northern) and lower (southern) vortex rings respectively, see Figure 5.42. Therefore, the general solution to the SVD problem is that the two rings have equal and opposite strengths. For these configurations, the center of vorticity given by Equation (2.53), is aligned with the z-axis,

$$\mathbf{J} = 2n\Gamma \begin{pmatrix} 0 \\ 0 \\ \cos\phi \end{pmatrix} . \tag{5.107}$$
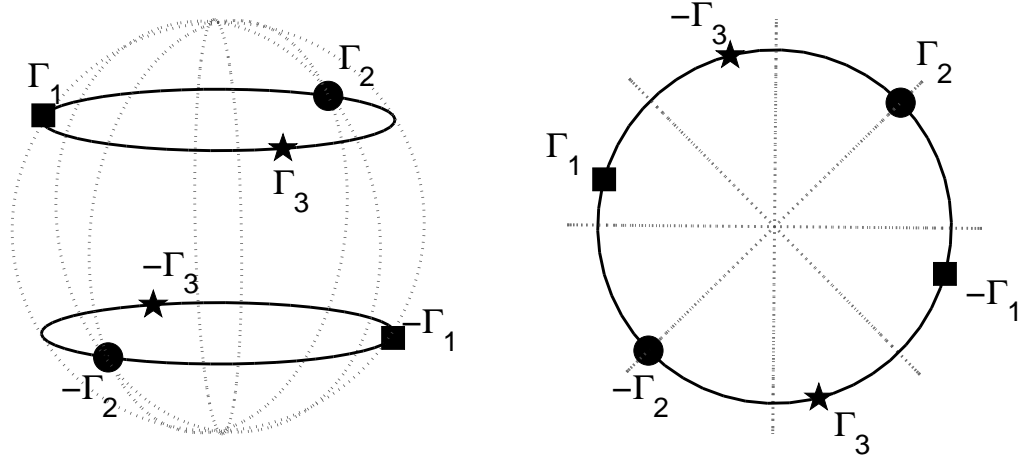
Figure 5.43: Top and oblique view. Solution using SVD of single von Kármán street on the sphere for $n = 3$. Dimension of null space is three with same-shape vortices having equal and opposite strength.

5.15.1.2 Number of Vortices Per Ring: $n = 3$

The case of 3 vortices per ring ($n = 3$) is a special degenerate case worthy of separate treatment.

For this case, the configuration matrix from Equation (2.49) takes on the form

$$
A_3 = \left(
\begin{array}{ccc|ccc}
a_3 & 0 & 0 & 0 & a_3 & 0 \\
-a_3 & 0 & 0 & 0 & -a_3 & 0 \\
\hline
0 & a_3 & 0 & 0 & 0 & a_3 \\
0 & -a_3 & 0 & 0 & 0 & -a_3 \\
\hline
0 & 0 & a_3 & a_3 & 0 & 0 \\
0 & 0 & -a_3 & -a_3 & 0 & 0 \\
\hline
0 & 0 & 0 & 0 & 0 & 0 \\
\vdots & \vdots & \vdots & \vdots & \vdots & \vdots \\
0 & 0 & 0 & 0 & 0 & 0
\end{array}
\right) ,
\tag{5.108}
$$

where the lower 9 rows are all zeros rows, and, a_3 is given by

$$a_3 = -\frac{3\sqrt{3}}{2}\sin^2\phi\cos\phi(\frac{1}{\sin^2\phi + 4\cos^2\phi} - \frac{1}{3\sin^2\phi}). \tag{5.109}$$

From (3.62), the singular values of A_3 are

$$\sigma_3 = \left(\begin{array}{cccccc} 2a_3, & 2a_3, & 2a_3, & 0, & 0, & 0 \end{array}\right)^T. \tag{5.110}$$

Clearly, the nullspace of the configuration matrix has dimension 3 and the corresponding $\boldsymbol{\Gamma}$ vector from Equation (3.68) has the form

$$\vec{\Gamma} = \Gamma_1 \begin{pmatrix} 1 \\ 0 \\ 0 \\ -1 \\ 0 \\ 0 \end{pmatrix} + \Gamma_2 \begin{pmatrix} 0 \\ 1 \\ 0 \\ 0 \\ 0 \\ -1 \end{pmatrix} + \Gamma_3 \begin{pmatrix} 0 \\ 0 \\ 1 \\ -1 \\ 0 \\ 0 \end{pmatrix}, \tag{5.111}$$

where Γ_1, Γ_2, and Γ_3 are three independent constants. One vortex in the northern ring is equal and opposite to the vortex in the southern ring that subtends it longitudinally by an angle equal to π (see Figure 5.43 for an illustration). With (2.53), the center of vorticity of the system satisfies

$$\mathbf{J} = \begin{pmatrix} \sin\phi & 0 & 0 \\ 0 & \sin\phi & 0 \\ 0 & 0 & \cos\phi \end{pmatrix} \left(\Gamma_1 \begin{pmatrix} 2 \\ 0 \\ 2 \end{pmatrix} + \Gamma_2 \begin{pmatrix} -1 \\ \sqrt{3} \\ 2 \end{pmatrix} + \Gamma_3 \begin{pmatrix} -1 \\ -\sqrt{3} \\ 2 \end{pmatrix} \right), \tag{5.112}$$

which, in general, does not align with the z-axis, hence does not correspond to a von Kármán street (i.e., the street was constructed about the polar axis, and we require the center of vorticity to be aligned with the polar axis). One obtains a von Kármán street only when $\Gamma_1 = \Gamma_2 = \Gamma_3$ ($= \Gamma$, say) in which case $\boldsymbol{\Gamma} = \Gamma(1, 1, 1, -1, -1, -1)^T$ and the center of vorticity aligns with the
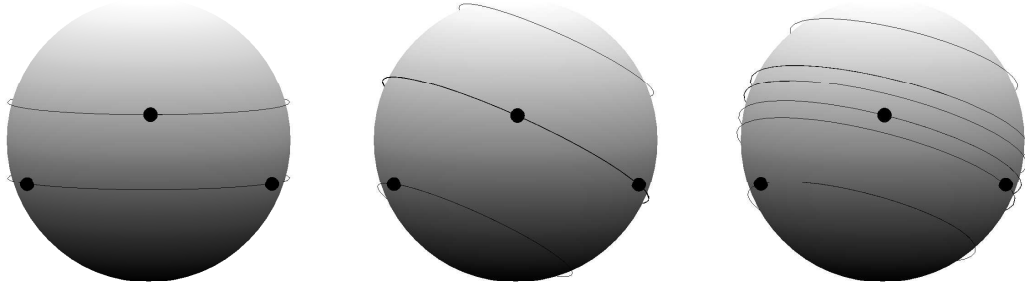
Figure 5.44: Computational result of time evolution of 6 vortices on the sphere with $\phi = 5\pi/12$. The initial configuration is the same as that defined in the previous figure. Images of the first column represent degenerate case with single VKS VKS and vortex strengths $[\Gamma_1, \Gamma_2, \Gamma_3] = [1, 1, 1]$. Second column has strengths $[\Gamma_1, \Gamma_2, \Gamma_3] = [1, 1.5, 1]$ with no resultant VKS, third case is $[\Gamma_1, \Gamma_2, \Gamma_3] = [1, 1.5, 1.2]$, also with no resultant VKS.

z-axis. In this case, when integrating (2.51), the vortices evolve as a single VKS (maintaining constant latitudes), see Figure 5.44. Whereas for $\Gamma_1 = \Gamma_3 \neq \Gamma_2$, the vortices no longer evolve as a von Kármán Street (do not maintain constant latitude) and move on three orbits about a common axis that is not aligned with the z-axis. When $\Gamma_1 \neq \Gamma_2 \neq \Gamma_3$, each vortex rotates about its own orbit (total of six).

5.15.2   With Pole Vortices

Pole vortices exist in geophysical flows, such as on the surface of Jupiter, and have been shown to play a critical role in the stability of co-latitudinal vortex rings on the sphere ([13], [10] and [44]).

5.15.2.1   Example: $n = 2$

As an example, for a configuation with two vortices per ring ($n = 2$), there will be a total of $N = 2(2) + 2 = 6$ vortices in the system. The configuration matrix in (2.60) has dimension

$\mathbb{R}^{(6 \cdot 5/2) \times 6} = \mathbb{R}^{15 \times 6}$. We label this configuration matrix $\hat{A}_2$ (i.e., In our notation, the overhead $\hat{\,}$ symbol indicates the addition of pole vortices) and it has the form

$$
\hat{A}_2 =
\left(
\begin{array}{cc|cc|cc}
\hat{d}_2 & -\hat{d}_2 & 0 & 0 & 0 & 0 \\
\hat{c}_2 & -\hat{c}_2 & 0 & 0 & 0 & 0 \\
-\hat{d}_2 & \hat{d}_2 & 0 & 0 & 0 & 0 \\
-\hat{c}_2 & \hat{c}_2 & 0 & 0 & 0 & 0 \\
\hat{a}_2 & 0 & \hat{a}_2 & 0 & -\hat{b}_2 & -\hat{b}_2 \\
-\hat{a}_2 & 0 & 0 & -\hat{a}_2 & \hat{b}_2 & \hat{b}_2 \\
0 & -\hat{a}_2 & -\hat{a}_2 & 0 & \hat{b}_2 & -\hat{b}_2 \\
0 & \hat{a}_2 & 0 & \hat{a}_2 & -\hat{b}_2 & -\hat{b}_2 \\
0 & 0 & \hat{c}_2 & -\hat{c}_2 & 0 & 0 \\
0 & 0 & \hat{d}_2 & -\hat{d}_2 & 0 & 0 \\
0 & 0 & -\hat{c}_2 & \hat{c}_2 & 0 & 0 \\
0 & 0 & -\hat{d}_2 & \hat{a}_4 & 0 & 0 \\
0 & 0 & 0 & 0 & 0 & 0 \\
0 & 0 & 0 & 0 & 0 & 0 \\
0 & 0 & 0 & 0 & 0 & 0
\end{array}
\right) ,
\tag{5.113}
$$

with

$$
\hat{a}_2 = -\frac{\cos\phi(3\cos^2\phi - 1)}{2(\cos^2\phi + 1)},
\tag{5.114}
$$

$$
\hat{b}_2 = \cos\phi,
\tag{5.115}
$$

$$
\hat{c}_2 = \frac{\cos\phi(\cos^2\phi + 2\cos\phi - 1)}{2(\cos^2\phi + 1)},
\tag{5.116}
$$

and

$$\hat{d}_2 = \frac{\cos\phi(\cos^2\phi + 2\cos\phi + 1)}{2(\cos^2\phi + 1)}. \tag{5.117}$$

In the state representation of $\hat{A}_2$, the first (second) two elements correspond to the northern (southern) street's vortices, and the last two elements correspond to the north and south pole vortices respectively. From (3.62), the singular values of this configuration are

$$\hat{\sigma}_2 = \begin{pmatrix} 2\sqrt{\hat{a}_2^2 + 2\hat{b}_2^2} \\ \sqrt{2\hat{a}_2^2 + 4\hat{c}_2^2 + 4\hat{d}_2^2} \\ \sqrt{2\hat{a}_2^2 + 4\hat{c}_2^2 + 4\hat{d}_2^2} \\ 0 \\ 0 \\ 0 \end{pmatrix}. \tag{5.118}$$

Since three of the singular values are zero, the dimension of the null space is three (i.e., $nullity(\hat{A}_2) = 3$). The solution to $\mathbf{\Gamma}$ is at best numeric for this class of configurations when using SVD. In the next subsection, we will highlight the general numeric solution for single vortex streets with pole vortices for any n.

5.15.2.2 General Numeric Solution

For a general single vortex with n vortices per ring, the $\mathbf{\Gamma}$ vector has length $N = 2(n + 1)$. The first and second set of n values correspond to the upper and lower vortex rings respectively; the $(2n + 1)$ and $(2n + 2)$ components correspond to the values of the north and south pole vortices.

Using the SVD method, the general solution for $n \geq 2$ has a null space of 3 and is of the general form

$$
\mathbf{\Gamma} = \Gamma
\begin{pmatrix}
1 \\
\vdots \\
1 \\
-1 \\
\vdots \\
-1 \\
0 \\
0
\end{pmatrix}
+ \Gamma_{north}
\begin{pmatrix}
f(\phi, n) \\
\vdots \\
f(\phi, n) \\
0 \\
\vdots \\
0 \\
1 \\
0
\end{pmatrix}
+ \Gamma_{south}
\begin{pmatrix}
f(\phi, n) \\
\vdots \\
f(\phi, n) \\
0 \\
\vdots \\
0 \\
0 \\
1
\end{pmatrix}.
\tag{5.119}
$$

The solution that interests us is when the poles have equal and opposite strength (i.e., $\Gamma_{north} = -\Gamma_{south}$) since it is the only case that will produce a single von Kármán street with equal and opposite rings. For this selection of pole vortices, the $f(\phi, n)$ terms cancel out, the vortex street will have equal and opposite rings with strength Γ, and the two poles will have an independent equal and opposite strength Γ_p, given by the following:

$$
\mathbf{\Gamma} = \Gamma
\begin{pmatrix}
1 \\
\vdots \\
1 \\
-1 \\
\vdots \\
-1 \\
0 \\
0
\end{pmatrix}
+ \Gamma_p
\begin{pmatrix}
0 \\
\vdots \\
\vdots \\
\vdots \\
\vdots \\
0 \\
1 \\
-1
\end{pmatrix}.
\tag{5.120}
$$

(a) Vortex Street Component   (b) Pole Vortices Component
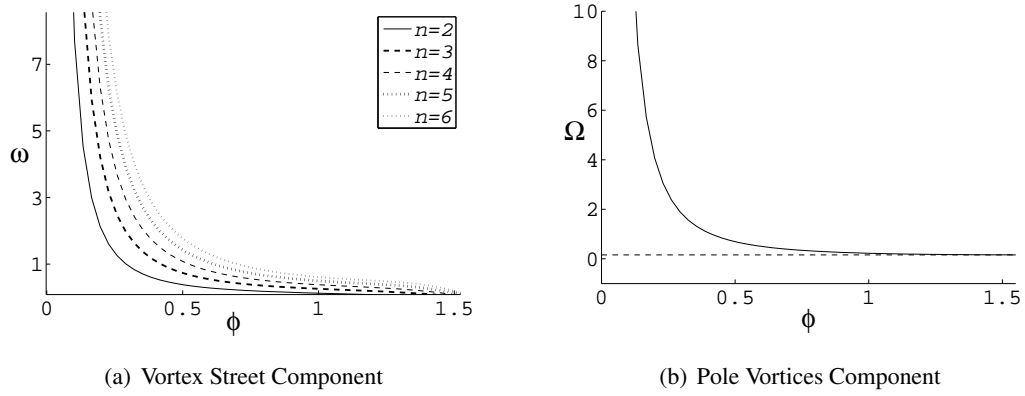
Figure 5.45: (a) Angular velocity ω as a function of vortex street latitude ϕ for $n = 2 \cdots 6$. ω decreases from $+\infty$ to 0 as ϕ is increased from 0 to $\pi/2$. (b) Additional angular velocity Ω for any n from pole vortices $(\pm\Gamma_p)$ with $\Gamma_p = +1$. As ϕ approaches $\pi/2$, Ω asymptotes at $\Gamma_p/(2\pi)$.

Furthermore, from (2.53), the center of vorticity for the single street with poles becomes

$$
\mathbf{J} = 2 \begin{pmatrix} 0 \\ 0 \\ n\Gamma\cos\phi + \Gamma_p \end{pmatrix}, \tag{5.121}
$$

and is parallel to the polar axis. With SVD, the solution to $f(\phi, n)$ is numeric. In the following section, we will build on SVD, and provide analytic solutions to the angular velocity of the street and to $f(\phi, n)$.

5.16 Angular Velocity and Explicit Solutions

From Equations (5.107) and (5.121), the longitude of vortex α, given by θ_α in Section **2.7.2**, rotates rigidly about the polar axis. The angular velocity, therefore, is simply $\dot\theta_\alpha$ for any vortex α such that its latitude $\phi_\alpha \neq 0$. We will solve for the angular velocity of single single streets, and show that this formulation can provide an analytic solution to Equation (5.119), specifically with an explicit expression for $f(\phi, n)$ in that equation.

5.16.1 Without Pole Vortices

For the single vortex street without poles, we require that $\dot{\theta}_1 = \dot{\theta}_2 = \ldots = \dot{\theta}_{2n}$ for relative equilibrium. The two rings are symmetrically skewed (by an angle of π/n). Therefore, the longitudes of the n vortices in the northern ring are: $0, 2\pi(1)/n, 2\pi(2)/n, \cdots, 2\pi(n-1)/n$. The longitudes of the n vortices in the southern ring are $\pi/n, 2\pi(1)/n+\pi/n, 2\pi(2)/n+\pi/n, \cdots, 2\pi(n-1)/n + \pi/n$. The longitudinal spacing between any two vortices α and λ in the same ring (i.e., $0 < \{\alpha, \lambda\} \le n$ or $n < \{\alpha, \lambda\} \le 2n$) is given by

$$\theta_\alpha - \theta_\lambda = \frac{2\pi}{n}(\alpha - \lambda). \tag{5.122}$$

If the two vortices are in different rings, with $0 < \alpha \le n$ and $n < \lambda \le 2n$, the longitudinal spacing is given by

$$
\begin{aligned}
\theta_\alpha - \theta_\lambda &= \frac{2\pi}{n}(\alpha - (\lambda - n)) - \frac{\pi}{n} \\
&\equiv \frac{2\pi}{n}(\alpha - \lambda) - \frac{\pi}{n}
\end{aligned}
\tag{5.123}
$$

As for the latitudes, the first n vortices have a latitude of ϕ, while the second n vortices have a latitude of $(\pi - \phi)$. Note that $\sin(\pi - \phi) = \sin(\phi)$ and $\cos(\pi - \phi) = -\cos(\phi)$. As for the vortex strengths, the rings must have equal and opposite strengths $\pm\Gamma$ from (5.106) for any $n \ne 3$[1]. Evaluating $\gamma_{1\lambda}$ in Eq. (2.56) gives

$$
\cos\gamma_{1\lambda} = \cos^2\phi + \sin^2\phi\cos\left(\frac{2\pi}{n}(\alpha - \lambda)\right), \quad 1 < \lambda \le n, \tag{5.124}
$$

$$
\cos\gamma_{1\lambda} = -\cos^2\phi + \sin^2\phi\cos\left(\frac{2\pi}{n}(\alpha - \lambda) - \frac{\pi}{n}\right), \quad n < \lambda \le 2n. \tag{5.125}
$$

---

[1]We do not solve the angular velocity for configurations with $n = 3$ when the vortex strengths of the streets' rings do not have equal and opposite strengths $\pm\Gamma$, since this system does not evolve as a vortex street (i.e., the polar axis and center of vorticity axis are not aligned). In order to solve for the angular velocity, one must derive the angular coordinates of the system with respect to the center of vorticity axis. For the treatment of a similar problem, see [57].

Substituting these properties into Eq. (2.55) we get

$$\omega \equiv \dot{\theta}_1 \quad = \quad \frac{\Gamma}{4\pi \sin \phi} \sum_{\lambda=2}^{n} \frac{\sin \phi \cos \phi - \cos \phi \sin \phi \cos \left(\frac{2\pi}{n}(1-\lambda)\right)}{1 - \cos \gamma_{1\lambda}} \tag{5.126}$$

$$+ \frac{\Gamma}{4\pi \sin \phi} \sum_{\lambda=n+1}^{2n} \frac{\sin \phi \cos \phi - \cos \phi \sin \phi \cos \left(\frac{2\pi}{n}(1-\lambda) - \frac{\pi}{n}\right)}{1 - \cos \gamma_{1\lambda}} \tag{5.127}$$

$$= \quad \frac{\Gamma \cos \phi}{4\pi} \sum_{\lambda=2}^{n} \frac{1 - \cos \left(\frac{2\pi}{n}(1-\lambda)\right)}{1 + \cos^2 \phi - \sin^2 \phi \cos \left(\frac{2\pi}{n}(1-\lambda)\right)} \tag{5.128}$$

$$+ \frac{\Gamma \cos \phi}{4\pi} \sum_{\lambda=n+1}^{2n} \frac{1 - \cos \left(\frac{2\pi}{n}(1-\lambda) - \frac{\pi}{n}\right)}{1 - \cos^2 \phi - \sin^2 \phi \cos \left(\frac{2\pi}{n}(1-\lambda) - \frac{\pi}{n}\right)}. \tag{5.129}$$

For example, if we have $n = 4$ vortices per ring, the angular velocity of the system becomes

$$\omega = \frac{\Gamma \cos \phi}{4\pi} \frac{\cos^4 \phi - 10 \cos^2 \phi - 15}{\cos^6 \phi + 5 \cos^4 \phi - 5 \cos^2 \phi - 1}. \tag{5.130}$$

5.16.2 With Pole Vortices

From Eq. (2.55), the overall change to the rotational velocity of the single vortex street system from the addition of vortices at the poles with equal and opposite strengths $\pm\Gamma_p \in \mathbb{R}$ is denoted as Ω (see Figure 5.45(b)), and given by

$$\Omega \quad = \quad \frac{\Gamma_p}{4\pi(1 - \cos \phi)} + \frac{\Gamma_p}{4\pi(1 + \cos \phi)} \tag{5.131}$$

$$= \quad \frac{\Gamma_p}{2\pi \sin^2 \phi}. \tag{5.132}$$

Furthermore, we can derive an analytic solution to $f(\phi, n)$ in Equation (5.119) by supplementing the SVD solution with a constraint on Equation (2.55). We contrast the angular velocity of the north and south rings with the addition of north and south pole vortices. Using the solution in (5.119), we will approach the problem by considering a configuration that has a north pole vortex

and no south pole vortex. That is, the selected vortex strengths are $(\Gamma, \Gamma_{north}, \Gamma_{south}) = (1, 1, 0)$, which gives us vortex strengths

$$\mathbf{\Gamma} = \Gamma \begin{pmatrix} 1+f \\ \vdots \\ 1+f \\ -1 \\ \vdots \\ -1 \\ f \\ 0 \end{pmatrix}. \tag{5.133}$$

Plugging (5.133) into (2.55), we derive the angular velocity, ω_1, for the vortices in the northern ring to be

$$
\begin{aligned}
\omega_1 \equiv{} & \dot{\theta}_1 = \dot{\theta}_2 = \ldots = \dot{\theta}_n \\
={} & \frac{1+f}{4\pi \sin\phi} \sum_{\lambda=2}^{n} \frac{\sin\phi \cos\phi_\lambda - \cos\phi \sin\phi_\lambda \cos(\theta_1 - \theta_\lambda)}{1 - \cos\gamma_{1\lambda}} \\
& + \frac{-1}{4\pi \sin\phi} \sum_{\lambda=n+1}^{2n} \frac{\sin\phi \cos\phi_\lambda - \cos\phi \sin\phi_\lambda \cos(\theta_1 - \theta_\lambda)}{1 - \cos\gamma_{1\lambda}} + \frac{f}{4\pi(1 - \cos\phi)},
\end{aligned}
$$

or

$$\omega_1 = \xi_1(1+f) + \xi_2 + \xi_3 f. \tag{5.134}$$

The angular velocity of the vortices in the southern ring, ω_2, is given by

$$
\begin{aligned}
\omega_2 \equiv{} & \dot{\theta}_{n+1} = \dot{\theta}_{n+2} = \ldots = \dot{\theta}_{2n} \\
={} & \frac{1+f}{4\pi \sin\phi} \sum_{\lambda=1}^{n} \frac{\sin\phi \cos\phi_\lambda + \cos\phi \sin\phi_\lambda \cos(\theta_{n+1} - \theta_\lambda)}{1 - \cos\gamma_{(n+1)\lambda}} \\
& + \frac{-1}{4\pi \sin\phi} \sum_{\lambda=n+2}^{2n} \frac{\sin\phi \cos\phi_\lambda + \cos\phi \sin\phi_\lambda \cos(\theta_{n+1} - \theta_\lambda)}{1 - \cos\gamma_{(n+1)\lambda}} + \frac{f}{4\pi((n+1) + \cos\phi)},
\end{aligned}
$$

or

$$\omega_2 = \xi_4(1 + f) + \xi_5 + \xi_6 f. \tag{5.135}$$

For the system to obtain relative equilibrium, we require that $\omega_1 \equiv \omega_2$, which gives us the analytic expression for f:

$$f \equiv f(\phi, n) = \frac{(\xi_4 + \xi_5) - (\xi_1 + \xi_2)}{(\xi_1 + \xi_3) - (\xi_4 + \xi_6)}. \tag{5.136}$$

Note that we have obtained this result by using only a north pole vortex in the formulation. The procedure can be repeated for the selection of vortex strengths in Equation (5.119) to be $(\Gamma, \Gamma_{north}, \Gamma_{south}) = (1, 0, 1)$. That is, the same result for f is derived when adding only a south pole vortex. The conclusion here is that the SVD formulation provides a simple means to solving the structure of the null space (which would be difficult to produce without SVD). The setback is that for large N, the SVD solution is at best numerical. When supplementing the SVD's numerical result with a constraint on the angular velocity of the system, we can fully solve the system analytically.

5.17 Streamline Topology

In this section, we present the fourth main contribution of this thesis. The analysis of the streamline topology of vortex equilibria and the associated bifurcations is greatly facilitated by the methods presented in Chapters **2** and **3**. We will revisit this topic again in the context of double vortex streets, and commence this section by presenting a basic tool in understanding the streamline patterns on the sphere in the index theorem of Poincaré:

Theorem 1. *(PIT): The index $I_f(S)$ of a two-dimensional surface S relative to any C^1 vector field f on S with at most a finite number of critical points, is equal to the Euler-Poincaré characteristic of S, denoted $\chi(S)$, i.e. $I_f(S) = \chi(S)$.*

We know for a sphere, $\chi(S) = 2$. The index for a center is $+1$, while that for a saddle is -1. Hence if c denotes the number of centers present (point vortices plus other centers), and s

(a) Type I   (b) $\Gamma_p^* = 0$ (c) Type II   (d) $\Gamma_p^* = 1.2$

(e) Type I   (f) $\Gamma_p^* = 7.5$ (g) Type III
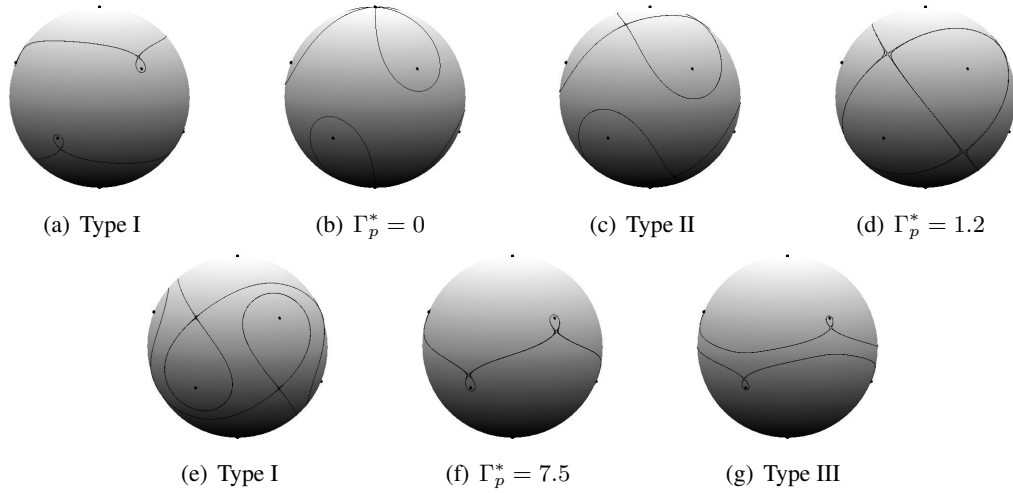
Figure 5.46: Streamlines topologies for a single von Kármán street with 3 vortices per ring and pole vortices of equal and opposite strength. The pole strength increases from -5 to $+10$. A total of three distinct topology types are identified within four different intervals, separated by three bifurcation topologies.

denotes the number of saddles, then one has $c - s = 2$. See [40] for more on applications of the PIT to the understanding of streamline patterns on the sphere.

Consider the case $n = 3$, $\phi = 3\pi/8$ and pole vortices of equal and opposite strength Γ_p. In this case, the VKS vortices are equal and opposite, with the vortices in the northern ring having strength $\Gamma = -1$. We vary Γ_p and study the change in the streamline topology. The sequence of distinct streamline topologies when Γ_p is increased from -5 to 10 is shown in Figure 5.46. For $\Gamma = -5$, one gets three stagnation points of hyperbolic or saddle type in each hemisphere. The streamlines associated with these hyperbolic points are plotted in Figure 5.46(a). These stream-lines are referred to as separatices because they separate regions with different fluid behavior. For example, in a region containing a point vortex and bounded by a separatix, the fluid orbits around the vortex, whereas in the middle region void of point vortices, the fluid is transported globally around the entire sphere. The streamline topology remains the same until Γ_p reaches the critical value $\Gamma_p^* = 0$. At this bifurcation value, the stagnation points collapse to two points of hyperbolic or saddle type at the poles as shown in Figure 5.46(b). As Γ_p becomes positive, three hyperbolic points reappear around each pole as shown in Figure 5.46(c). As Γ_p increases, the three hyperbolic points of the north and southern hemispheres approach each other until the

(a) n=2   (b) n=3
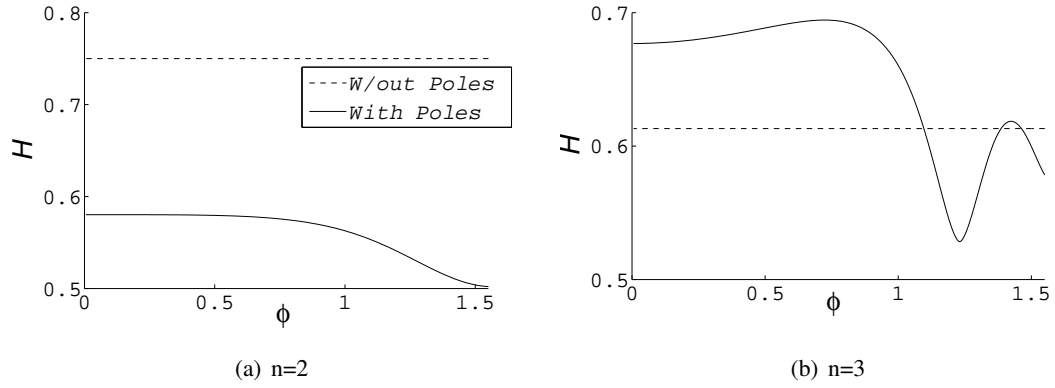
Figure 5.47: Shannon Entropy sweeps for single vortex street with (solid line) and without (dashed line) pole vortices. (a) Two vortices per ring, (b) Three vortices per ring.

associated separatrices coincide at a critical pole strength $\Gamma_p^* \approx 1.2$, see Figure 5.46(d). At this bifurcation value, the overall streamline topology changes and region characterized by global fluid transport disappears. As Γ_p increases beyond $\Gamma_p^* = 1.2$, the separatices detach and the streamline topology changes again with a region of global fluid transport reemerging, see Figure 5.46(e). Here, the separatices of the stagnation points of the northern hemisphere encircle vortices from the southern hemisphere and vice-versa. The streamline topology remains the same until Γ_p reaches another critical value $\Gamma_p^* \approx 7.5$ where the separatrices associated with the hyperbolic points of northern and southern hemispheres coincide and the region of global transport disappears again, see Figure 5.46(f). As Γ_p increases beyond $\Gamma_p^* = 7.5$, the separatrices split again forming three distinct regions characterized by global fluid transport and six regions characterized by fluid orbiting around a local vortex.

5.18 Shannon Entropy: Effect of Adding Pole Vortices

Here we analyze the Shannon Entropy of single vortex streets upon adding pole vortices. Since the total number of vortices in the system changes by two when adding pole vortices, we will use Equation (3.83), which makes it possible to compare systems consisting of different number of vortices.

5.18.1 Number of Vortices Per Ring: $n = 2$

We begin our analysis for streets with two vortices per ring. Recall from (5.104) that the singular values for this configuration are $\sigma = (2\sqrt{2}a_2, 2\sqrt{2}a_2, 2a_2, 0)^T$, where a_2 is given by Equation (5.103). From (3.84), the probabilities (normalized eigenvalues of covariance matrix $A^T A$) are $\vec{P} = (2/5, 2/5, 1/5, 0)^T$, and are independent of $a_2(\phi)$. The Shannon Entropy of this configuration becomes

$$H = \frac{1}{2}\left(\log_4 2 + 2\right) = const. \tag{5.137}$$

Upon adding pole vortices to this system, the singular values are given by (5.118). From Equation (3.84), the probabilities for this system become a non-linear function of ϕ. In Figure 5.47(a), we illustrate the change of Shannon Entropy upon introducing pole vortices to the vortices, and we see that for any latitude ϕ, the configuration *without* pole vortices has a higher entropy.

5.18.2 Number of Vortices Per Ring: $n = 3$

The dimension of the null space for a single vortex street with three vortices per ring, and no pole vortices is three (see section **5.15.1.2**),That is, three of the six singular values are equal to zero. From (5.110), the singular values are $(2a_3, 2a_3, 2a_3, 0, 0, 0)^T$, with $a_3(\phi)$ defined in (5.109). The probabilities for this configuration with Equation (3.84) become $\vec{P} = (1/3, 1/3, 1/3, 0, 0, 0)^T$, and are independent of ϕ. The normalized Shannon Entropy from (3.83) for $n = 3$ becomes

$$H = H = \log_6 3 = const. \tag{5.138}$$

Upon adding pole vortices, the probabilities become a non-linear function of the angle ϕ. In Figure 5.47(b), we compare the normalized Shannon Entropy with and without poles. Interestingly, the two lines cross, which tells us that certain intervals of ϕ have a higher entropy pole vortices are present.

5.18.3   Number of Vortices Per Ring: $n \geq 4$

In Figure 5.48, we contrast the normalized Shannon Entropy of configuration with differerent n, namely for the selections $n = 4, 5, 7, 13, 20$. We repeat the analysis for configurations without (5.48(a)) and with (5.48(b)) pole vortices. We observe that all curves are nonlinear functions of ϕ, and that there exist local maxima and minima on the curves. Values of ϕ which correspond to local maximizers of the Shannon Entropy are deemed to be more robust with respect to their singular value distributions, than those corresponding to local minimizers. Interestingly, the most likely number of vortices n per ring changes with ϕ. That is in Figure (5.48), for any given ϕ, one n curve has the highest entropy.
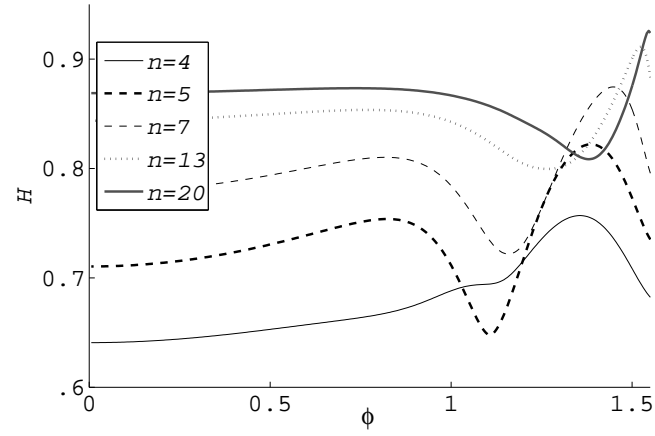
(a) No Poles
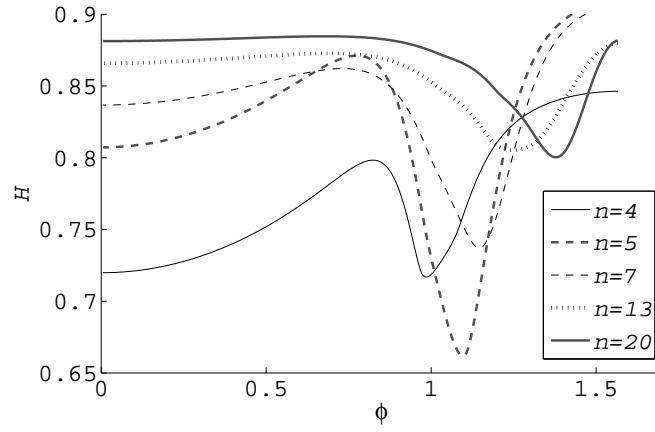
(b) With Poles

Figure 5.48: Normalized Shannon Entropy sweeps for single von Kármán streets on the sphere for (a) $n = 4, 5, 7, 13, 20$ without poles, and (b) $n = 4, 5, 7, 13, 20$ with poles. The intention of these figures to compare the entropy of configurations with different n.

Chapter 6. Double Von Kármán Streets on the Sphere

We now expand on the previous chapter by adding a second vortex street to our model. As shown in Figure 6.49 from [37], two adjacent vortex streets on the surface Jupiter lie in close proximity to one another. In this chapter, we investigate the effects that the additional street has on the equilibrium solution, role of the pole vortices, streamline topology, and Shannon Entropy.
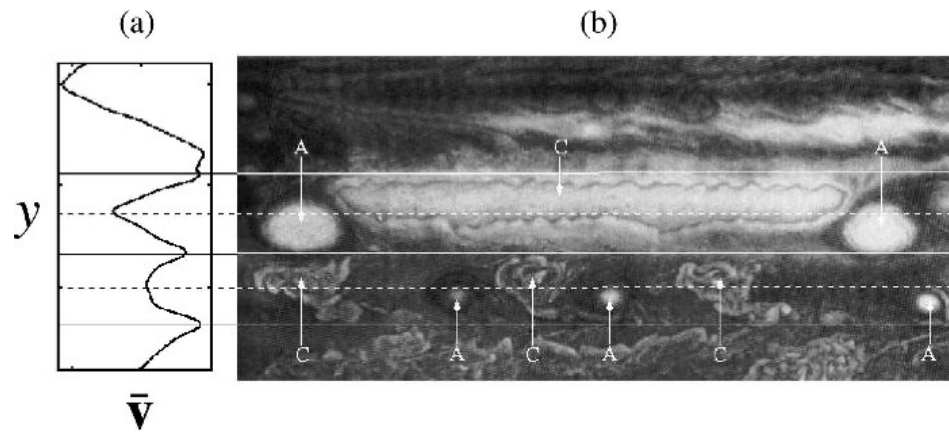
Figure 6.49: Double vortex street on Jupiter. Cyclones (anti-cyclones) are labeled 'C' ('A'). Velocity profiles on the left demonstrate identification of cyclones & anti-cyclones, where the first have a positive slope and the latter have a negative slope in the y vs. v̄ domain. Image from [37].
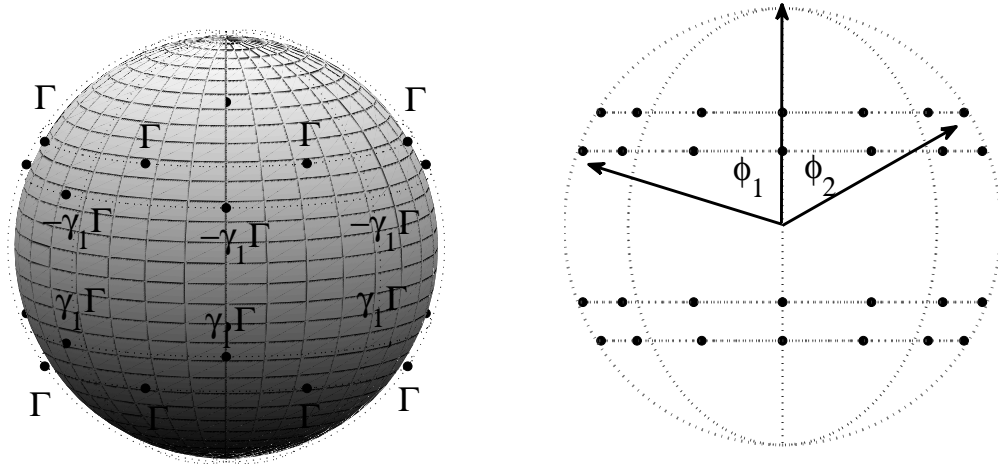
Figure 6.50: Double Von Kármán Street schematic, illustrating SVD solution and ring definition. Dimension of the null space is 1. The angle associated with the two rings are ϕ_1 and ϕ_2 respectively. Note that which latitude is smaller is of no importance. Rather, we identify the different rings by the ordering in the state representation of Equation (6.139).

6.19   Construction and SVD Solution

6.19.1   Without Pole Vortices

The double von Kármán street model used in this chapter consists of one vortex street in the northern hemisphere, and a second in the southern hemisphere, where each street consists of two symmetrically skewed n-vortex rings. One ring in each hemisphere has a latitude of ϕ_1 from its respective hemisphere's pole−these are referred to as the ϕ_1-rings. The second ring in each hemisphere has an angle of ϕ_2, and these are referred to as the ϕ_2-rings. See Figure 6.50 for an illustration. We write (2.60) for a total of $N = 4n$ vortices on the sphere and seek configurations satisfying (2.50). Using the SVD method, it was found that the dimension of the null space for this system is one. The ϕ_2 rings have equal and opposite strengths $\pm\Gamma$, while the ϕ_1-rings have equal and opposite strengths $\pm\gamma_1\Gamma$, where $\gamma_1 = \gamma_1(\phi_1, \phi_2, n) \in \mathbb{R}$. Note that the SVD method can at best provide a numerical result for γ_1. As for the state representation, the first n state variables corresponds to the northern ϕ_2-ring's vortices. The second and third set of n state variables correspond to the northern and southern ϕ_1-ring's vortices respectively. Finally, the

last n state variables correspond to the southern ϕ_2-ring's vortices. In other words, the solution is

$$\boldsymbol{\Gamma} = \Gamma(1, ..., 1, -\gamma_1, ..., -\gamma_1, \gamma_1, ..., \gamma_1, -1, ... -1)^T. \qquad (6.139)$$

Furthermore, the general center of vorticity for this class of configurations from Equation (2.53) is given by

$$\mathbf{J} = 2\Gamma \begin{pmatrix} 0 \\ 0 \\ n(\cos\phi_2 - \gamma_1 \cos\phi_1), \end{pmatrix}, \qquad (6.140)$$

which implies that the center of vorticity is aligned with the polar axis for any choice of parameters.

6.19.2 With Pole Vortices

A double VKS with equal and opposite vortex rings (i.e., $\gamma_1 = 1$) can be achieved by adding vortices at the north and south poles. The dimension of the null space for the system solved using (2.49) is three. The additional dimensionality of the solution comes from the pole vortices that have independent strengths Γ_{north} and Γ_{south}, and the general form is

$$\mathbf{\Gamma} = \Gamma \begin{pmatrix} 1 \\ \vdots \\ 1 \\ -\gamma_1 \\ \vdots \\ -\gamma_1 \\ \gamma_1 \\ \vdots \\ \gamma_1 \\ -1 \\ \vdots \\ -1 \\ 0 \\ 0 \end{pmatrix} + \Gamma_{north} \begin{pmatrix} f_1(\phi_1, \phi_2, n) \\ \vdots \\ f_1(\phi_1, \phi_2, n) \\ f_2(\phi_1, \phi_2, n) \\ \vdots \\ f_2(\phi_1, \phi_2, n) \\ f_3(\phi_1, \phi_2, n) \\ \vdots \\ f_3(\phi_1, \phi_2, n) \\ 0 \\ \vdots \\ 0 \\ 1 \\ 0 \end{pmatrix} + \Gamma_{south} \begin{pmatrix} f_1(\phi_1, \phi_2, n) \\ \vdots \\ f_1(\phi_1, \phi_2, n) \\ g_2(\phi_1, \phi_2, n) \\ \vdots \\ g_2(\phi_1, \phi_2, n) \\ g_3(\phi_1, \phi_2, n) \\ \vdots \\ g_3(\phi_1, \phi_2, n) \\ 0 \\ \vdots \\ 0 \\ 0 \\ 1 \end{pmatrix}, \qquad (6.141)$$

where numerically $(f_2 - g_2) = -(f_3 - g_3) = \Delta_p$. Clearly, the pole vortices affect the strength of the street vortices, and the poles can be chosen so to make the constant γ_1 from Equation (5.106) equal to one, thus achieving the double VKS shown in Figure 6.51. One solution would be to choose the pole strengths to be equal and opposite with $\Gamma_{north} = -\Gamma_{south} = \gamma_2 \Gamma$, where

$$\gamma_2 = \gamma_2(\phi_1, \phi_2, n) = \frac{\gamma_1 - 1}{\Delta_p}. \qquad (6.142)$$
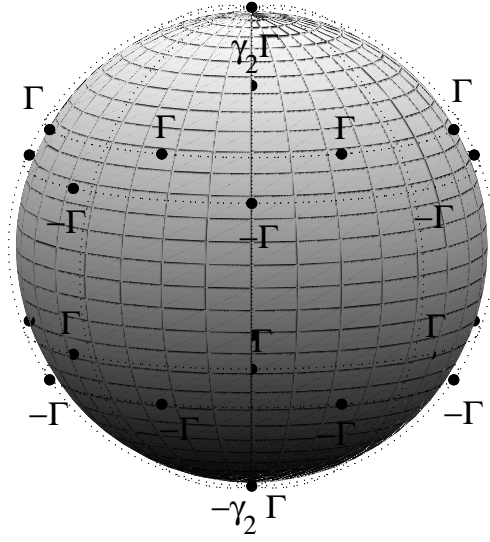
Figure 6.51: Double von Kármán Street with poles schematic, illustrating SVD solution. Dimension of the null space is 3, with the pole vortices having independent strengths of one another. Since the poles vortices affect the street vortices' strength, their strengths are chosen to be $\pm\gamma_2\Gamma, \gamma_2 = \gamma_2(\phi_1, \phi_2, n)$ in order to ensure $\gamma_1 \equiv 1$ in Figure 6.50.

The solution collapses into one dimension with the pole vortices stacked at the end of the state representation vector, such that

$$\mathbf{\Gamma} = \Gamma(1, ..., 1, -1, ..., -1, 1, ..., 1, -1, ... -1, \gamma_2, -\gamma_2)^T \in \mathbb{R}^{4n+2}. \tag{6.143}$$

Note that this solution to γ_2 is numeric. In Section **6.20.1** we will couple this solution with the angular velocity formulation to produce an analytic result. It is also relevant to note that the center of vorticity of the double VKS is

$$\mathbf{J} = 2\Gamma \begin{pmatrix} 0 \\ 0 \\ n(\cos\phi_2 - \cos\phi_1) + \gamma_2 \end{pmatrix}. \tag{6.144}$$

(a) $\phi_1 = 3\pi/8$ (b) $\phi_1 = 5\pi/12$
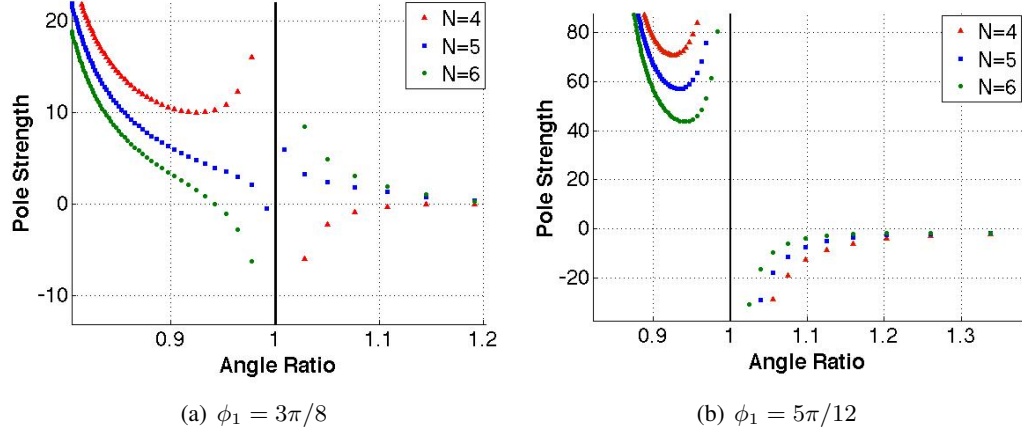
Figure 6.52: Equilibrium curves present for pole strength (γ_2) vs. angle ratio (ϕ_1/ϕ_2) when $n = [4, 5, 6]$. Angle ϕ_1 is held fixed at $3\pi/8$ in (a), and $5\pi/12$ in (b), while ϕ_2 is the control parameter. Recall that $\gamma_2 = \gamma_2(\phi_1, \phi_2, n)$. Recall that the pole strength can be any value for the degenerate case $\phi_1 = \phi_2$ represented by the solid line in the graphs (single VKS).

6.19.3 Equilibrium Curves

Each double street configuration with its unique set of parameters ϕ_1, ϕ_2 and n has a single corresponding pole strength factor $\gamma_2(\phi_1, \phi_2, n)$ associated with its pole vortices. Figures 6.52(a) and 6.52(b) illustrate two sets of equilibrium curves present in the coordinate system γ_2 vs. the angle ratio ϕ_1/ϕ_2. The angle ϕ_1 is kept fixed at $3\pi/8$ in 6.52(a), and $5\pi/12$ in 6.52(b), with a sweep of $0 < \phi_2 < \pi/2$. Three curves are displayed in each of the two subplots corresponding to $n = 4$, 5 and 6 vortices per ring. A degenerate case occurs when $\phi_1 = \phi_2$, which entails the merger of the two rings in each hemisphere−and this results in the collapse of the system into a single vortex street. As was described in the previous section, the configuration will be an equilibrium single VKS for any $\Gamma_{north} = -\Gamma_{south}$ (hence the vertical line in the figure). When ϕ_2 is perturbed by an infinitesimal amount from $\phi_1 = \phi_2$, the magnitude of the pole strength factor γ_2 required to create a double VKS must be infinitely large. It is also relevant to point out that for certain ratio values, the pole strength $\gamma_2 \equiv 0$, which implies that some configurations are double vortex streets only in the absence of pole vortices.

6.20 Angular Velocity and Explicit Solutions

6.20.1 Without Pole Vortices

Using the angular velocity formulation, we will derive an analytic solution to $\gamma_1(\phi_1, \phi_2, n)$ in Equation (6.139). Assuming that the center of vorticity is parallel to the polar axis (i.e., Equation (6.140) applies), we conclude that the rate of change of the vortices' longitudes in Equation (2.55) is equivalent to the angular velocity of the configuration [2]. We begin our analysis by choosing the same vortex strengths found in Equation (6.139), and assume that γ_1 is an unknown parameter to be solved. Next, we derive one expression for the angular velocity of the vortices in the ϕ_1 rings, and a second for the vortices in the ϕ_2 rings. For simplicity in writing, we define

$$\Theta_{\alpha\lambda} \equiv \frac{\sin\phi_\alpha \cos\phi_\lambda - \cos\phi_\alpha \sin\phi_\lambda \cos(\theta_\alpha - \theta_\lambda)}{4\pi \sin\phi_\alpha (1 - \cos\gamma_{\alpha\lambda})}. \tag{6.145}$$

Let ω_1 be the angular velocity of the ϕ_1 rings' vortices. Therefore, it follows that

$$\omega_1 \equiv \dot\theta_{n+1} = \dot\theta_{n+2} = \ldots = \dot\theta_{2n} \tag{6.146}$$

$$= \dot\theta_{2n+1} = \dot\theta_{2n+2} = \ldots = \dot\theta_{3n}.$$

Next, we come up with a general expression for ω_1 from the angular velocity $\dot\theta_{n+1}$ of vortex $n + 1$. From Equations (2.55) and (6.145), we have

$$\dot\theta_{n+1} = \sum_{\lambda=1}^{n}\Gamma_\lambda\Theta_{(n+1)\lambda} + \sum_{\lambda=n+2}^{2n}\Gamma_\lambda\Theta_{(n+1)\lambda} + \sum_{\lambda=2n+1}^{3n}\Gamma_\lambda\Theta_{(n+1)\lambda} + \sum_{\lambda=3n+1}^{4n}\Gamma_\lambda\Theta_{(n+1)\lambda}.$$

---

[2] The longitudes of the vortices in the ϕ_2 rings are $0, 2\pi(1)/n, 2\pi(2)/n, \cdots, 2\pi(n-1)/n$, while those of the ϕ_1 rings are $\pi/n, 2\pi(1)/n + \pi/n, 2\pi(2)/n + \pi/n, \cdots, 2\pi(n-1)/n + \pi/n$.

The four summations correspond to the four vortex rings, with an exclusion of the $n + 1$ term from the 2nd summation. Next, we replace the Γ_λ terms with their values from (6.139) to get

$$
\begin{aligned}
\dot{\theta}_{n+1} &= \Gamma \sum_{\lambda=1}^{n} \Theta_{(n+1)\lambda} - \gamma_1 \Gamma \sum_{\lambda=n+2}^{2n} \Theta_{(n+1)\lambda} + \gamma_1 \Gamma \sum_{\lambda=2n+1}^{3n} \Theta_{(n+1)\lambda} - \Gamma \sum_{\lambda=3n+1}^{4n} \Theta_{(n+1)\lambda} \\
&= \gamma_1 \Gamma \left(\sum_{\lambda=2n+1}^{3n} \Theta_{(n+1)\lambda} - \sum_{\lambda=n+2}^{2n} \Theta_{(n+1)\lambda} \right) + \Gamma \left(\sum_{\lambda=1}^{n} \Theta_{(n+1)\lambda} - \sum_{\lambda=3n+1}^{4n} \Theta_{(n+1)\lambda} \right),
\end{aligned}
$$

or simply that

$$
\omega_1 = \gamma_1 \Gamma \vartheta_1(\phi_1, \phi_2, n) + \Gamma \vartheta_2(\phi_1). \tag{6.147}
$$

We now repeat the process for the vortices on the ϕ_2 of rings by defining ω_2 as their angular velocity. Therefore,

$$
\begin{aligned}
\omega_2 &\equiv \dot{\theta}_1 = \dot{\theta}_2 = \ldots = \dot{\theta}_n \tag{6.148} \\
&= \dot{\theta}_{3n+1} = \dot{\theta}_{3n+2} = \ldots = \dot{\theta}_{4n}.
\end{aligned}
$$

We use the angular velocity $\dot{\theta}_1$ of vortex 1 to form an expression for ω_2. From Equations (2.55) and (6.145),

$$
\dot{\theta}_1 = \sum_{\lambda=2}^{n} \Gamma_\lambda \Theta_{1\lambda} + \sum_{\lambda=n+1}^{2n} \Gamma_\lambda \Theta_{1\lambda} + \sum_{\lambda=2n+1}^{3n} \Gamma_\lambda \Theta_{1\lambda} + \sum_{\lambda=3n+1}^{4n} \Gamma_\lambda \Theta_{1\lambda}.
$$

Note the exclusion of the 1st term in the 1st summation. Again, we replace the Γ_λ terms with their values from (6.139) to get

$$
\begin{aligned}
\dot{\theta}_1 &= \Gamma \sum_{\lambda=2}^{n} \Theta_{1\lambda} - \gamma_1 \Gamma \sum_{\lambda=n+1}^{2n} \Theta_{1\lambda} + \gamma_1 \Gamma \sum_{\lambda=2n+1}^{3n} \Theta_{1\lambda} - \Gamma \sum_{\lambda=3n+1}^{4n} \Theta_{1\lambda} \\
&= \gamma_1 \Gamma \left(\sum_{\lambda=2n+1}^{3n} \Theta_{1\lambda} - \sum_{\lambda=n+1}^{2n} \Theta_{1\lambda} \right) + \Gamma \left(\sum_{\lambda=2}^{n} \Theta_{1\lambda} - \sum_{\lambda=3n+1}^{4n} \Theta_{1\lambda} \right).
\end{aligned}
$$

Therefore,

$$\omega_2 = \gamma_1 \Gamma \vartheta_3(\phi_1, \phi_2, n) + \Gamma \vartheta_4(\phi_2). \tag{6.149}$$

Our condition for relative equilibrium is that the ϕ_1 and ϕ_2 rings have the same angular velocity (i.e., $\omega_1 = \omega_2$). By equating (6.147) and (6.149), we derive an explicit expression for γ_1 of Equation (6.139) to be

$$\gamma_1 = \frac{\vartheta_4 - \vartheta_2}{\vartheta_1 - \vartheta_3}. \tag{6.150}$$

This result can be used to generate analytic curves for the angular velocity, or of γ_1, as a function of the parameters.

6.20.2   With Pole Vortices

Maintaining the state representation in Equation (6.143), the desired vortex strengths of the system are given by

$$\boldsymbol{\Gamma} = (\Gamma, \ldots, \Gamma, -\Gamma, \ldots, -\Gamma, \Gamma, \ldots, \Gamma, \ldots, \Gamma, \Gamma_p, -\Gamma_p)^T, \tag{6.151}$$

where Γ_p is the pole vortex strength that we will solve (to match the solution in (6.143)). We can also assume that Equation (6.144) applies (i.e., the system is rotating rigidly about the polar axis). Therefore, as in Equation (6.146), we define ω_1 to be the angular velocity of the vortices in the ϕ_1 ring. We derive an expression for ω_1 by substituting (5.131), (6.145) and (6.151) into (2.55) to get

$$\begin{aligned}
\dot{\theta}_1 &= \Gamma \left(\sum_{\lambda=1}^{n} \Theta_{(n+1)\lambda} - \sum_{\lambda=n+2}^{2n} \Theta_{(n+1)\lambda} + \sum_{\lambda=2n+1}^{3n} \Theta_{(n+1)\lambda} - \sum_{\lambda=3n+1}^{4n} \Theta_{(n+1)\lambda} \right) \\
&\quad + \frac{\Gamma_p}{2\pi \sin^2 \phi_1},
\end{aligned}$$

or

$$\omega_1 = \Gamma \zeta_1(\phi_1, \phi_2, n) + \Gamma_p \zeta_2(\phi_1). \tag{6.152}$$

Similarly, if define ω_2 to be the angular velocity of the vortices in the ϕ_2 rings, and using the same substitutions in conjunction with the relations of Equation (6.148), we derive that

$$\omega_2 = \zeta_3(\phi_1, \phi_2, n)\Gamma + \zeta_4(\phi_2)\Gamma_p, \tag{6.153}$$

where

$$\zeta_3 = \left(\sum_{\lambda=2}^{n} \Theta_{1\lambda} - \sum_{\lambda=n+1}^{2n} \Theta_{1\lambda} + \sum_{\lambda=2n+1}^{3n} \Theta_{1\lambda} - \sum_{\lambda=3n+1}^{4n} \Theta_{1\lambda} \right),$$

and

$$\zeta_4 = \frac{1}{2\pi \sin^2 \phi_2}.$$

Since the angular velocity of the two rings should be equal for relative equilibrium (i.e., $\omega \equiv \omega_1 \equiv \omega_2$), we derive the analytic expression for the required pole vortex strength to be

$$\Gamma_p = \gamma_2 \Gamma, \quad \gamma_2 = \gamma_2(\phi_1, \phi_2, n) = \frac{\zeta_1 - \zeta_3}{\zeta_4 - \zeta_2}. \tag{6.154}$$

Example 2. *Consider a double vortex street with $n = 2$ per ring. Derive the angular velocity. The angular velocity ω_1 in terms of ϕ_1, ϕ_2. From (6.152), we have*

$$\omega_1 = \zeta_1 \Gamma + \zeta_2 \Gamma_p, \tag{6.155}$$

with

$$\zeta_1 = -\frac{1}{4\pi \cos \phi_1} \left(\frac{1 - \cos^2 \phi_1 \cos^2 \phi_2 + 4\cos^3 \phi_1 \cos \phi_2 - 4\cos \phi_1 \cos \phi_2}{-\cos^2 \phi_1 + \cos^4 \phi_1 \cos^2 \phi_2 + 1 - \cos^2 \phi_1 \cos^2 \phi_2} \right), \tag{6.156}$$

(a) $\phi_1 = 3\pi/8, \quad 0 < \phi_2 < \phi_1$

(b) $\phi_1 = 3\pi/8, \quad \phi_1 < \phi_2 < \pi/2$

(c) $\phi_1 = 5\pi/12, \quad 0 < \phi_2 < \phi_1$

(d) $\phi_1 = 5\pi/12, \quad \phi_1 < \phi_2 < \pi/2$
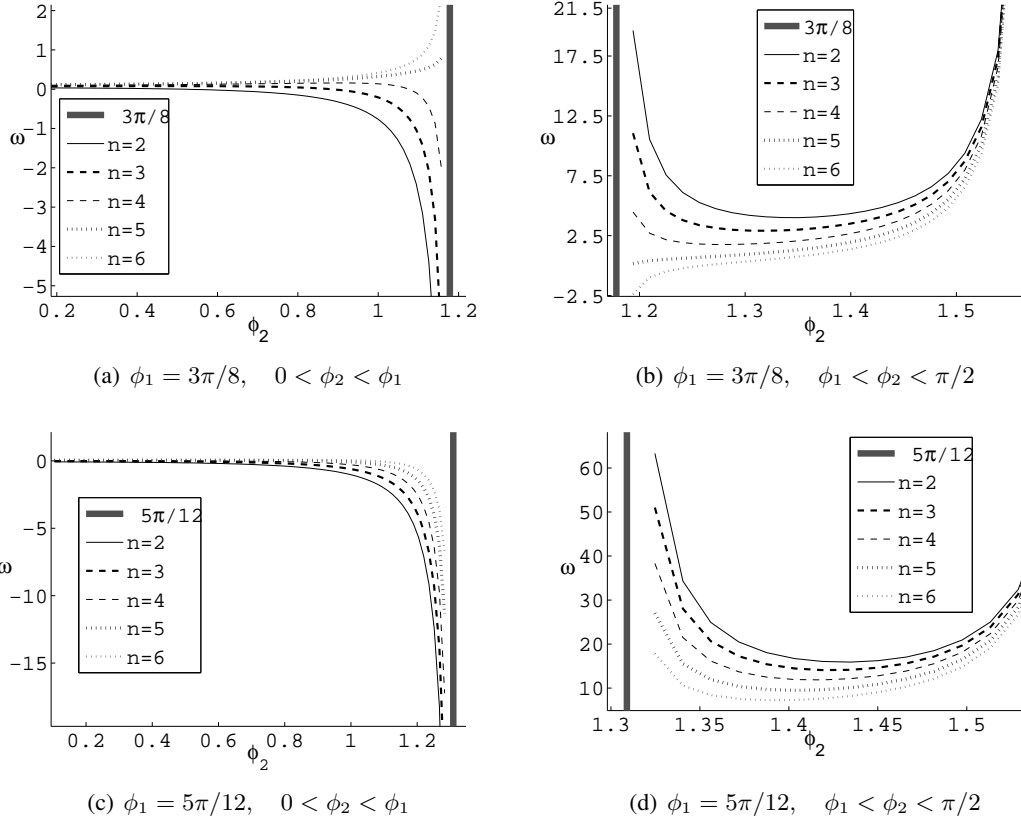
Figure 6.53: Angular velocity ω vs. angle ϕ_2 for $n = 2 \cdots 5$. ϕ_1 held fixed at $3\pi/8$ in (a) and (b), and at $5\pi/12$ in (c) and (d). Singularity occurs since $\Gamma_p \to \pm\infty$ as $\phi_2 \to \phi_1$.

and just as in Equation (5.131),

$$\zeta_2 = \frac{1}{2\pi \sin^2 \phi_1}. \tag{6.157}$$

The angular velocity ω_2 from (6.153) *becomes*

$$\omega_2 = \zeta_3 \Gamma + \zeta_4 \Gamma_p, \tag{6.158}$$

with

$$\zeta_3 = \frac{1}{4\pi \cos \phi_2} \left(\frac{1 - \cos^2 \phi_2 \cos^2 \phi_1 + 4 \cos^3 \phi_2 \cos \phi_1 - 4 \cos \phi_2 \cos \phi_1}{-\cos^2 \phi_2 + \cos^4 \phi_2 \cos^2 \phi_1 + 1 - \cos^2 \phi_2 \cos^2 \phi_1} \right), \tag{6.159}$$

and with Equation (5.131) *we have*

$$\zeta_4 = \frac{1}{2\pi \sin^2 \phi_2}.$$ (6.160)

The required pole vortex strength factor γ_2 to ensure that ω_1 and ω_2 are equivalent can then be solved analytically using Eq. (6.154).

In Figure 6.53, analytic curves for the angular velocity vs. ϕ_2 with constant ϕ_1 are presented for $n = 2 \cdots 6$, and for the two scenarios $\phi_1 = 3\pi/8$ and $\phi_1 = 5\pi/12$. The angular velocity approaches either $+\infty$ or $-\infty$ when $\phi_2 \rightarrow \phi_1$ or $\phi_2 \rightarrow \pi/2$ since the required pole vortex strength factor γ_2 to ensure relative equilibrium also becomes infinite. Note also that the equilibrium curves in Figure 6.52 can be derived analytically. In the next subsection, we address the result of choosing different angular velocities for each set of vortex rings in each hemisphere (i.e., Eq. (6.154) is not satisfied).

6.20.3 Shearing Structures

In Section **1.3.2** of the introduction, we referenced an investigation by Coddington *et al.* in Figure 1.8 from [17]. To recapitulate, small amplitude sinusoidal perturbations resulted from laser-zapping the central vortex site, and effectively modifying its circulation strength. In the context of vortex streets on the sphere, the pole vortices can be interpreted as the 'central' vortex, while the vortex rings can be interpreted as concentric bands. As was discussed in the previous section, the selection of the pole vortices' strengths plays a crucial role in attaining a relative equilibrium. If γ_2 from Eq. (6.154) is not chosen correctly, the different vortex rings will rotate with different angular velocities, resulting in a non-equilibrium *shearing*-like flow. Numerical experiments of vortex street configurations with an incorrect selection of parameter γ_2 demonstrated the existence of periodic and quasi-periodic dynamics with respect to the inter-vortical distances (see Figures 6.54 and 6.55). These types of configurations exhibit periodic and quasi-periodic oscillations, and can be more generally classified as *shearing* vortex lattices.
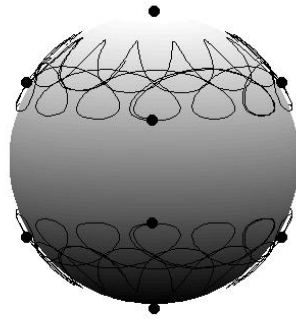
(a) All vortices (side view)
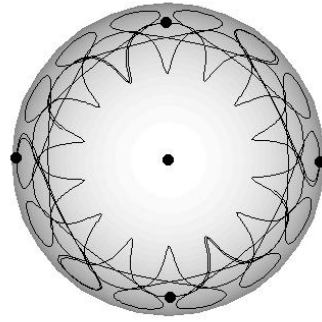
(b) All vortices (top view)
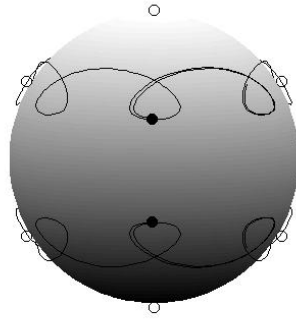
(c) Vortex set I (side view)
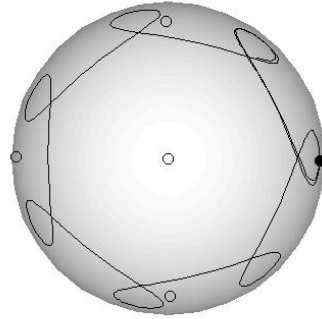
(d) Vortex set I (top view)
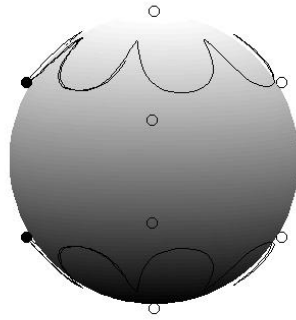
(e) Vortex set II (side view)
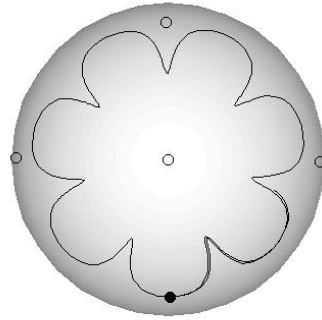
(f) Vortex set II (top view)

Figure 6.54: Time evolution of point vortices of double street with poles given by solid black lines. Pole vortex strengths do not satisfy equilibrium condition given by Equation (6.143). Specifically, pole vortices have strength 0 instead of $\pm\gamma_2\Gamma$. Figures (a) and (b) show evolution of all vortices. Figures (c) and (d) show evolution of one isolated set of vortices marked by filled circles (one from each hemisphere), and demonstrate that the dynamics is periodic. Figures (e) and (f) show the evolution of a second set of vortices, also showing periodic dynamics.
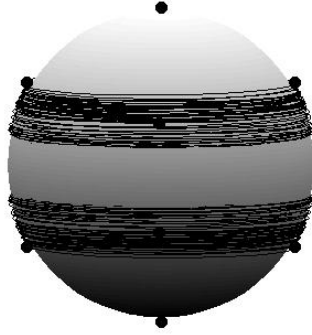
Figure 6.55: Quasi-periodic time evolution of point vortices of double street with poles given by solid black lines. Pole vortex strengths do not satisfy equilibrium condition given by Equation (6.143). Specifically, pole vortices have strength $\pm 2\gamma_2 \Gamma$ instead of $\pm \gamma_2 \Gamma$.

6.21 Streamline Topology

The stagnation points for a double street naturally have a more elaborate structure than those of a single street. Consider the case with $n = 5$, $\phi_1 = 13\pi/40$, pole vortices with equal and opposite strength $\gamma_2 \Gamma$ such as in (6.143), and with ϕ_2 is the control parameter. We distinguish streamline topologies based on the angle ratio $R = \phi_1/\phi_2$. Figures 6.56 and 6.58 contain a sequence of streamline topologies for ratios $R < 1$ and $R > 1$ respectively. Figure 6.57 is a curve of pole vortex strength γ_2 vs. angle ratio R for the configuration at hand, and provides a supplementary insight into the $\gamma_2 - R$ and changes in the streamline topology.

First consider Figure 6.56 in which $R < 1$ (which means that the ϕ_2-rings are closer to the equator). When $R < 0.691$, one gets ten stagnation points of hyperbolic or saddle type in each hemisphere−each of which is aligned longitudinally with one of the street vortices. In addition, there are two sets of separatrices in each hemisphere that separate five different regions of global fluid transport; this is the first topology type and is illustrated in Figure 6.56(a). The streamline topology remains the same until $R^* \approx 0.691$. At this point, the two separatices in each hemisphere collapse into one, and two of the regions associated with global fluid transport disappear−see Figure 6.56(b). Next, as soon as $R > 0.691$, the separatrix in each hemisphere

splits into a set of two, and two regions with global fluid transport reemerge; this marks topology type II illustrated in Figure 6.56(c). As we increase R, the five stagnation points that are aligned with the ϕ_1-rings in each hemisphere approach the equator until they merge at the bifurcation value $R^* \approx 0.755$. At this point, there are five stagnation points at the equator that are aligned with the ϕ_1-rings. In addition, there are still five remaining stagnation points of hyperbolic or saddle type in each hemisphere that are longitudinally aligned with the ϕ_2-rings, see Figure 6.56(d). As soon as $R > 0.755$, each of the stagnation points at the equator splits into two, and they move away from each other as R increases. The topology remains unchanged (labeled type III in Figure 6.56(e)) until the next bifurcation value of $R^* \approx 0.801$ is reached. At this bifurcation, two sets of separatrices in each hemisphere coincide and two regions associated with global fluid transport disappear−see Figure 6.56(f). Note also from Figure 6.57 that $\gamma_2 = 0$ at this bifurcation value.

As soon as $R > 0.801$, the separatrices that had just merged split and the two regions with global fluid transport reemerge; this range of R is identified as topology type IV in Figure 6.56(g). As R increases, the five stagnation points in each hemisphere that are longitudinally aligned with the ϕ_2-rings approach their respective hemisphere's poles. The next bifurcation point is reached when $R^* \approx 0.843$ at which point the ten stagnation points collapse into two of hyperbolic or saddle type at the poles (Figure 6.56(h)). Observe from Figure 6.57 that this bifurcation point corresponds to an inflection point in the $\gamma_2 - R$ relation. As soon as $R > 0.843$, five hyperbolic points reappear around the poles, and begin moving towards the ϕ_1-rings' vortices; this returns us to topology type III shown in Figure 6.56(i). The next bifurcation that occurs results from the ten stagnation points at the equator. As R increases, the stagnation points continue to move on the equator until $R^* \approx 0.893$, at which point they collapse into a total of five stagnation points of hyperbolic or saddle type−with each one longitudinally aligned with one of the vortices from the ϕ_2 rings. See Figure 6.56(j). As soon as $R > 0.893$, the five stagnation points at the equator split, reappear as a total of ten, and as R increases, they begin to move away from the equator and towards the ϕ_2-rings. The range $0.893 < R < 1$ marks the final topology interval (which is back to Type II) for the range $0 < R < 1$, and is illustrated in Figure 6.56(k).

(a) Type I   (b) $R^* = 0.691$ (c) Type II   (d) $R^* = 0.755$

(e) Type III   (f) $R^* = 0.801$ (g) Type IV   (h) $R^* = 0.843$

(i) Type III   (j) $R^* = 0.893$ (k) Type II
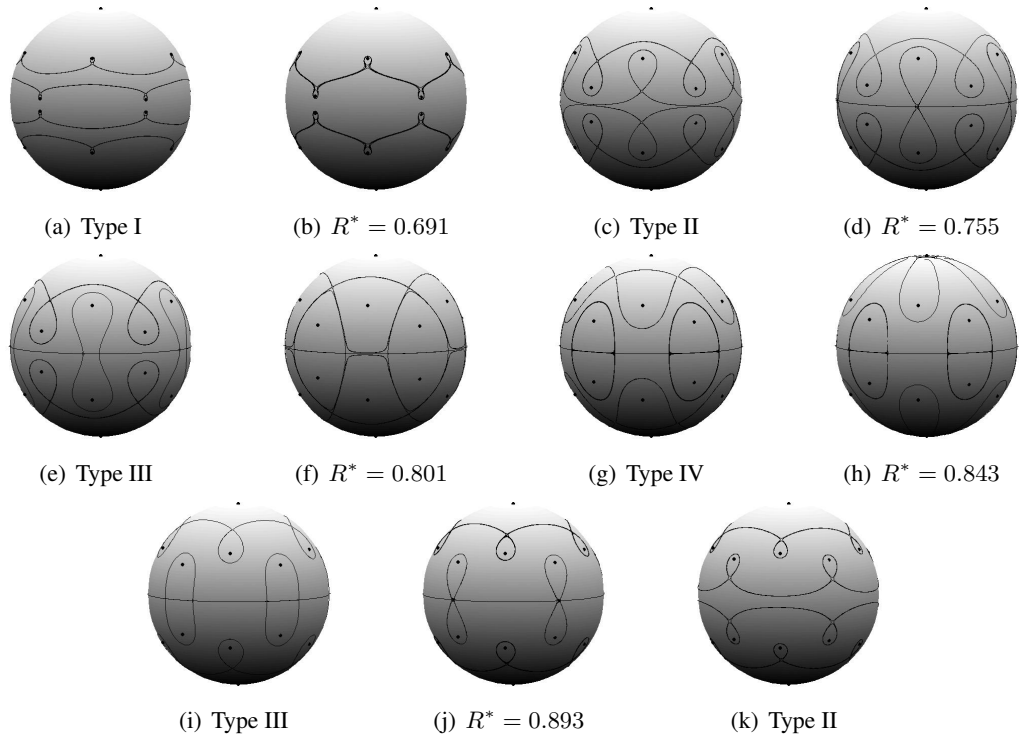
Figure 6.56: Streamline topology sequence for the range of ratios $0.68 < R < 0.95$ in ascending order. Stagnation points move either along constant longitude lines or the equator as the ratio varies. Four different topology types are illustrated (labeled I, II, III, IV), and are separated by five bifurcation scenarios.
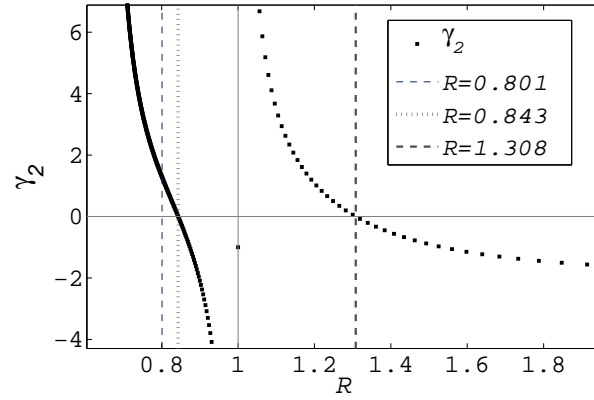
Figure 6.57: Equilibrium curve corresponding to the relation of the pole vortex strength factor γ_2 vs. angle ratio R for $n = 5$, $\phi = 13\pi/40$, and with ϕ_2 as the control parameter. This plot also corresponds to the configurations found in Figures 6.56 and 6.58, and illustrates (with vertical lines) that some of the bifurcation points correspond to either an inflection in the curve or when $\gamma_2 = 0$.
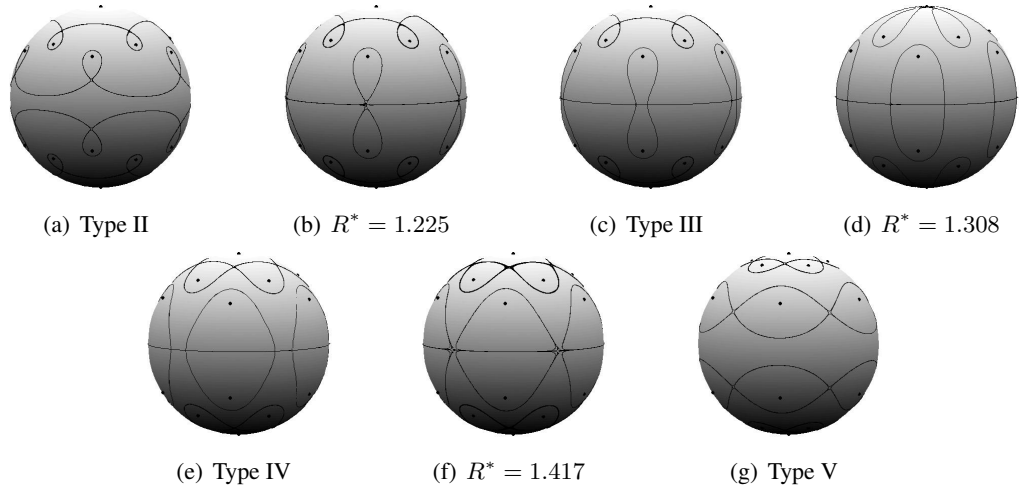
Figure 6.58: Streamline topology sequence for the range of ratios $1.05 < R < 2.25$ in ascending order. Maintaining notation consistency with Figure 6.56, four different topology types are evident, labeled Types II, III, IV, V.

We now describe the results of Figure 6.58 in which $R > 1$ (this means that the ϕ_2 rings are closer to the poles). We start with the first topology interval illustrated in Figure 6.58(a). To be consistent with the notation from Figure 6.56, the first topology interval is Type II. There are ten stagnation points of hyperbolic or saddle type in each hemisphere—each of which is aligned longitudinally with one of the street vortices. In addition, there are two sets of separatrices in each hemisphere that separate five different regions of global fluid transport. As R increases, the stagnation points move away from the street vortices. The first five stagnation points in each hemisphere are longitudinally aligned with the ϕ_1-rings and are approaching the equator; the second five are longitudinally aligned with the ϕ_2-rings and are approaching the poles. The topology remains unchanged until $R^* \approx 1.225$, at which point the first five stagnation points from each hemisphere (total of ten) approach each other, and merge to form five stagnation points of hyperbolic or saddle type at the equator. At this bifurcation value, one of the regions associated with global fluid transport disappears. As soon as $R > 1.225$, each of the five stagnation points at the equator splits into two, giving a total of ten stagnation points of hyperbolic or saddle type at the equator. As R increases, these stagnation points continue to move apart on the equator

towards the longitudes associated with the ϕ_2-rings. This range of R is described by topology type III, and is illustrated in Figure 6.58(c).

Meanwhile, the remaining five stagnation points in each hemisphere are longitudinally aligned with the ϕ_2-rings and are approaching the poles as R is increasing. The next bifurcation occurs when $R^* \approx 1.308$ (see Figure 6.58(d)) when the stagnation points collapse to two points of hyperbolic or saddle type at the poles. Note that from Figure 6.57 that this bifurcation point corresponds to the case when $\gamma_2 = 0$.

As R increases, five stagnation points reappear around the poles and begin moving towards the ϕ_2-rings as shown in Figure 6.58(e), and described as topology type IV. The next bifurcation takes place when $R^* \approx 1.417$ as shown in Figure 6.58(f). At this point, the ten stagnation points at the equator merge (at the longitude associated with the ϕ_2-rings) into five of hyperbolic or saddle type. As soon as $R > 1.417$, we get our last topology type (see Figure 6.58(g)), labeled type V. Each of the five stagnation points at the equator split into two to give a total of ten, and begin to move away from the equator and towards the ϕ_2-rings as R increases.

It can be observed from looking at Figure 6.57 that one can extract information about the streamline topology by looking at the γ_2 vs. R curve. In Figure 6.52, we can see that each set of parameters n and ϕ_1 has a unique γ_2 vs. R curve, and will therefore also have a unique set of streamline topologies over the range R. Therefore, the streamline topologies discussed for Figures 6.56 and 6.58 are specific only to the aforementioned parameters, and cannot be generalized as being the result for any double vortex street.

6.22   Shannon Entropy

In this section, we will illustrate a few results for the normalized Shannon Entropy (from (3.83)) of double vortex streets. In Figure 6.59, we have the Shannon Entropy vs. angle ϕ_2, for $\phi_1 = 3\pi/8$ and $n = 3, 4, 8, 10$. In each subfigure, we illustrate the effect of adding pole vortices to the configurations. The entropy curves for the double vortex street are much richer in structure than were those for the single vortex street. There is a set of local minima and maxima associated with

(a) $n = 3$

(b) $n = 4$

(c) $n = 8$

(d) $n = 10$
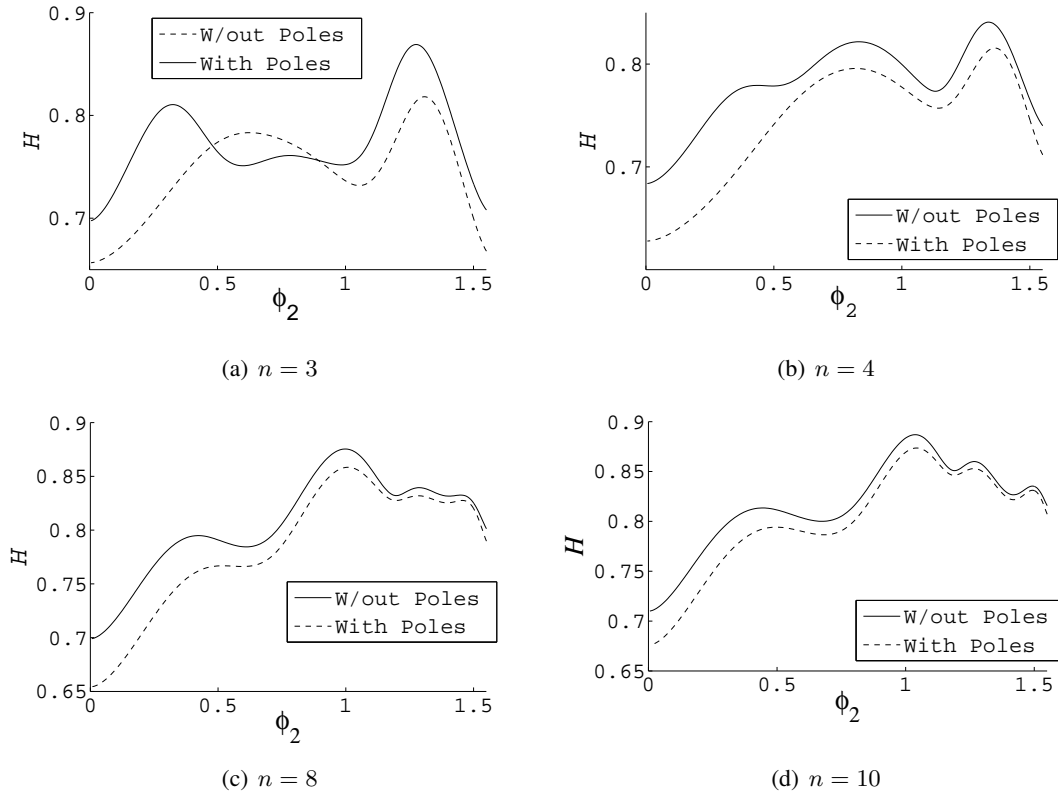
Figure 6.59: Shannon Entropy vs ϕ_2 for $\phi_1 = 3\pi/8$ and $n = 3, 4, 8, 10$. The figures llustrate the effect on entropy upon adding pole vortices to the configuration.

the curves. For the case $n = 3$, the curves with and without pole vortices cross several times, while when $n > 3$ the curves for configurations without pole vortices have a higher entropy than do the curves for configurations that do not for all ϕ_2. We interpret values of ϕ_2 which correspond to local maximizers of the Shannon Entropy as more robust with respect to their singular value distributions, than the remaining values of ϕ_2. In addition, those at local maxima would tend to get 'selected' more often than others in a random search setting as distributions with larger entropy have more combinatorial ways of being chosen at random [56].

Chapter 7. Conclusions

7.23   Summary

This report was a study of several key properties of relative vortex equilbria−or vortex lattices. To recapitulate, we used a condition for relative vortex equilbrium derived from the Hamiltonian point vortex model (Chapter **2**). In Chapter **3**, we introduced three tools from linear algebra to facilitate our analysis. At the starting point of our work, the techniques presented in Chapters **2** and **3** made it possible to find all vortex strengths, given by Γ, for a given configuration that will ensure that the vortices remain in relative equilbrium. The main contributions of this thesis can be classified into four categories:

1. *Asymmetric equilibria:* It was shown that asymmetric lattices with a non-trivial equilibrium cannot be chosen at random (i.e., when the vortex locations are selected at random from a uniform distribution). Instead, it is possible to begin with a general random asymmetric lattice, and converge to an asymmetric geometry that has a non-trivial solution via a 'Brownian ratchet' scheme that mimics the thermal cooling observed in Bose Einstein Condensates ([25], [26]). Via Singular Value Decomposition (SVD), the ratchet scheme utilized the singular values associated with the configuration matrix A (see (2.49)) to converge to a non-trivial equilibrium (i.e., $nullity(A) > 0$). That is, the smallest singular value must be zero. If the convergence scheme is repeated for the same initial configuration, the ratchet converges to a different asymmetric equilibrium with each run. Although non-trivial equilibria lie arbitrarily close to one another, there is a non-zero, finite distance

between a trivial and non-trivial equilibrium configuration, and is given by the Frobenius norm $\| \cdot \|_F$. In other words, the set of non-trivial equilbria is not dense within the set of all possible configurations. For results, see Chapter **4**.

2. *Shannon Entropy:* The Shannon Entropy associated with A was studied, and it was found that geometries that are more prevalent in physical settings have higher entropies than those that are less common. Therefore, we interpret the Shannon Entropy as a scalar measure of the robustness, or likelihood of existence of a given configuration geometry. With the Brownian ratchet scheme, the system tended to converge to an equilibrium configuration whose entropy was within the same neighborhood as the initial configuration. By normalizing the Shannon Entropy, we proposed that we can be compare configurations containing a different number of vortices. In the context of geophysical flows, the Shannon Entropy could be used as a means to predict the most likely parameters of vortex streets (i.e., latitude of the streets, number of vortices in the street, etc.). Shannon Entropy results are present in Chapters **4**, **5** and **6**.

3. *Model of vortex streets of the sphere:* We presented solutions to both single (chapter **5**) and double (Chapter **6**) vortex streets on the sphere. The SVD technique provided a systematic way of solving vortex equilbria for large N. The solution to $\mathbf{\Gamma}$ with this approach was numeric since the dimension of A was large. When coupled with the center of vorticity and angular velocity formulations, it was possible to build on SVD and extract analytic results for the vortex strengths. It was found that non-trivial solutions to symmetric vortex equilibria lie along smooth equilibrium curves within the configuration space, which means that it is possible to modify the inter-vortical geometry smoothly from one configuration with a nontrivial solution that possesses a certain symmetry to a second while maintaining relative equilibrium. This also implies that certain symmetric equilibria solutions lie arbitrarily close. One example of such a smooth transition was for the double

vortex street on the sphere with pole vortices, where the relative strength of the pole vortices γ_2 (in Equation (6.143)) was given by an analytic function of the system geometry, and varied smoothly with the angles of the vortex streets from the poles.

It was found that pole vortices play an important role in *fixing*, or in other words, assuring that the vorticity vector remained constant. That is, pole vortices have a central role in the creation or destruction of vortex streets. Studies in which the strength of the pole vortices was perturbed from equilibrium resulted in shearing, which we define as periodic and quasi-periodic orbits of the inter-vortical distances about the center of vorticity vector. We made the comparison to [17], in which the central vortex of a BEC lattice was blasted by laser. The blast effectively changed the strength of the central vortex, and resulted in small amplitude sinusoidal perturbations.

4. *Streamline topology of vortex streets on the sphere:* With the techniques presented, we demonstrated that the streamline topology bifurcation analysis is greatly facilitated. Streamline topology analysis is a crucial feature of vortex equilibria, as different topologies entail different fluid transport and mixing regimes. For single and double vortex streets, we presented the different topology types, and linked bifurcations to critical points on the equilibrium curves.

7.24   Future Work

Several important results and conclusions were attained in this study. However, with the closing of this thesis, many open questions were discovered along the way, and there is now a rich variety of topics that are ripe for investigation. Several topics include:

1. *Stability of vortex lattices:* In particular, the stability of vortex streets on sphere. A starting point for this investigation would be to follow the work done by [13], in which they examined the nonlinear stability of a single vortex ring with a fixed latitude−both with and without the presence of pole vortices. The general Hessian matrix for the configuration

was solved, and the authors were able to derive a bifurcation diagram that distinguished stable and unstable regimes with respect to the parameters affecting the configuration's geometry and vortices' relative strengths. Since a vortex street consists of two symmetrically skewed rings, stability results could follow from the techniques used in this work.

2. *Vortex lattices interacting with solid boundaries:* This could be incorporated into the aforementioned techniques by modeling boundaries via the method of images. A starting point could be the introduction of symmetric arrays of boundaries and vortices, and developed into cases in which solid boundary breaks the symmetry of lattices.

3. *Viscous vortex lattices:* The Navier Stokes equation can produce a model for a single viscous point vortex (see Appendix **B.2**). Modeling systems with more than one viscous point vortex becomes much more difficult, since the natural radial symmetry associated with the single viscous vortex breaks. It might possible to formulate a model for approximate viscous vortices, and derive whether the types of geometries solved for inviscid point vortices translate as solutions to viscous vortex configurations.

4. *The reverse problem and uniqueness:* The problem in reverse is whether it is possible to derive or estimate a configuration from a configuration matrix. As a numeric solution, it might be possible to do this via a Brownian ratchet, in which the geometry components (inter-vortical distances and orientations) are fluctuated until they converge towards a desired A. In addition, does a given configuration matrix A correspond to a single configuration X, or can multiple configurations with unique geometries possess the same configuration matrix? This problem was introduced in a Section **4.4**, in which the number of independent variables corresponding the positions of a configuration with N points (or vortices) were solved, both in the presence and absence of a coordinate system, and were compared to the number of non-trivial elements in the configuration matrix A for different N. The point to be made was whether the system can be described as undetermined or over-determined for different N.

5. *Biased ratchets:* The Brownian ratchet presented converges with no consideration to the form of the solution. Biased ratchets can be designed that possess constraints on the geometry (for example: an allowable range of distances between the vortices, or bounded domains), or on the solution (example: one might aspire to solve for configurations in which the vortices all have equal strength.)

6. *Shannon Entropy:* In a work to appear by Newton & Sajako, vortex lattices are perturbed from equilibrium, and the Shannon Entropy of A will be tracked as the vortex system evolves dynamically with time. The motivation is to determine the correlation between the dynamics, entropy and evolution of point vortex systems.

Bibliography

[1] J. R. Abo-Shaer, C. Raman, J. M. Vogels, and W. Ketterle. Observation of vortex lattices in bose einstein condensates. *Science*, 292:476–479, 2001.

[2] A. A. Abrikosov. On the magnetic properties of superconductors of the second group. *Sov. Phys. JETP*, 6:1174–1178, 1957.

[3] A. A. Abrikosov. Type ii superconductors and the vortex lattice. *Rev. Mod. Phys.*, 76, 2004.

[4] H. Aref. A note on the energy of relative equilibria of point vortices. *J. Fluid Mech.*, 39:1–79, 2007.

[5] H. Aref. Point vortex dynamics: A classical mathematcs playground. *Jour. Math. Phys.*, 48:065401, 2007.

[6] H. Aref. Vortices and polynomials. *Fluid Dynamics Research*, 39:5–23, 2007.

[7] H. Aref, P. K. Newton, M. A. Stremler, T. Tokieda, and D. L. Vainchtein. Vortex crystals. *Advances in Applied Mechanics*, 39:1–79, 2003.

[8] R. A. Barkley. The kuroshio-oyashio front as a compound vortex street. *J. Mar. Res.*, 26:83–104, 1968.

[9] M. W. Berry, S. T. Dumais, and G. W. O'Brien. Using linear algebra for intelligent information retrieval. *University of Tennessee Preprint*, pages 1–24, 1994.

[10] S. Boatto and H. E. Cabral. Nonlinear stability of a latitudinal ring of point-vortices on a nonrotating sphere. *SIAM J. Appl. Math.*, 64 (1):216–230, 2003.

[11] M. Brons, B. Jakobsen, K. Niss, A. V. Bisgaard, and L. K. Voigt. Streamline topology and vorticity patterns in the near-wake of a circular cylinder at moderate reynolds numbers. *J. Fluid Mech.*, 584:23–43, 2007.

[12] L. F. Burlaga. A heliospheric vortex street. *J. Geophys. Res.*, 95:4333–4336, 1990.

[13] H. E. Cabral, K. R. Meyer, and D. S. Schmidt. Stability and bifurcations for the n+1 vortex problem on the sphere. *Regular and Chaotic Dynamics*, 8:259–282, 2003.

[14] L. J. Campbell and R. Ziff. A catalog of two-dimensional vortex patterns. *Informal Report, Los Alamos Scientific Laboratory*, 7384-MS:1–40, 1978.

[15] G. C. Chamoun, E. Kanso, and P. K. Newton. Von kármán vortex streets on the sphere. *under consideration for publication in J. Fluid. Mech.*, 2008.

[16] J. Y-K. Cho and L. M. Polvani. The emergence of jets and vortices in freely evolving shallow-water turbulence on a sphere. *Physics of Fluids*, 8 (6):1531–1552, June 1996.

[17] I. Coddington, P. Engels, V. Schweikhard, and E. A. Cornell. Observations of tkachenko oscillations in rapidly rotating bose-einstein condensates. *Physical Review Letters*, 91 (10):100402, September 2003.

[18] Y. Couder and C. Baddevent. Experimental and numerical study of vortex couples in two-dimensional flows. *J. Fluid Mech.*, 173:225–251, 1986.

[19] R. Courant and D. Hilbert. *Methods of Mathematical Physics*, volume I,II. Wiley, New York, 1953.

[20] C. Dombrowski, L. Cisneros, S. Chatkaew, R. E. Goldstein, and J. O. Kessler. Self-concentration and large-scale coherence in bacterial dynamics. *Phys. Rev. Lett.*, 93:098103, 2004.

[21] U. Domm. Über dir wirbelstrassen von geringster instabilität. *Z. Angewandte Math. Mech. (ZAMM)*, 36:367–371, 1956.

[22] P. Drineas, A. Frieze, R. Kannan, S. Vempala, and V. Vinay. Clustering large graphs via the singular decomposition. *Machine Learning*, 56:9–33, 2004.

[23] C. F. Driscoll and K. S. Fine. Experiments on vortex dynamics in pure electron plasmas. *Phys. Fluids*, 2:1359–1366, 1990.

[24] J. Dusek, P. Le Gal, and P. Fraunie. A numerical and theoretical study of the first hopf bifurcation in a cylinder wake. *J. Fluid Mech.*, 264:59–80, 1994.

[25] P. Engels, I. Coddington, P. C. Haljan, and E. A. Cornell. Nonequilibrium effects of anisotropic compression applied to vortex lattices in bose-einstein condensates. *Phys. Rev. Lett.*, 89:100403–1–100403–4, 2002.

[26] P. Engels, I. Coddington, P. C. Haljan, V. Schweikhard, and E. A. Cornell. Observation of long-lived vortex aggregates in rapidly rotating bose-einstein condensates. *Phys. Rev. Lett.*, 90:170405–1–170405–4, 2003.

[27] U. Essmann and H. Trauble. The direct observation of individual flux lines in type ii superconductors. *Phys. Lett.*, 24A:256–530, 1967.

[28] D. Etling. On atmospheric vortex streets in the wake of large islands. *Met. Atmos. Phys.*, 41:157–164, 1989.

[29] R. P. Feynman. *Progress in Low Temperature Physics*. D.F. Brewer, North-Holland, 1 edition, 1955.

[30] K. S. Fine, A. C. Cass, and W. G. Flynn C. F. Driscoll. Relaxation of 2d turbulence to vortex crystals. *Phys. Rev. Lett.*, 75:3277, 1995.

[31] A. Friedmann and P. Poloubarinova. Über forschreitende singularitäten der ebenen bewegung einer inkompressiblen flüssigkeit. *Recueil de Géophysique*, V:9–23, 1928.

[32] V. L. Ginzburg and L. D. Landau. On the theory of superconductivity. *Zh. Eksp. Theor. Fiz.*, 20:1064, 1950.

[33] D. Godfrey, G. E. Hunt, and V. E. Suomi. Some dynamical properties of vortex streets in saturn's atmosphere from analysis of voyager missions. *Geo. Res. Lett.*, 10:865–868, Sept 1983.

[34] B. A. Grzybowski, H. A. Stone, and G. M. Whitesides. Dynamic self-assembly of magnetized millimeter-sized objects rotating at a liquid-air interface. *Nature*, 405:1033–1036, 2000.

[35] T. H. Havelock. The stability of motion of rectilinear vortices in ring formation. *Philos. Mag.*, 11:617–633, 1931.

[36] H. F. Hess, R. B. Robinson, R. G. Dynes, J. M. Valles, and J. V. Waszczak Jr. Scanning-tunneling microscope observation of the abrikosov flux lattice and the density of states near and inside a fluxoid. *Phys. Rev. Lett.*, 62:214–216, 1989.

[37] T. Humphreys and P. S. Marcus. Vortex street dynamics: The selection mechanism for the areas and locations of jupiters vortices. *Jour. Atmos. Sci.*, 64:1318–1333, 2007.

[38] C. P. Jackson. A finite-element study of the onset of vortex shedding in flow past variously shaped bodies. *J. Fluid. Mech.*, 182:23–45, 1987.

[39] M. I. Jamaloodeen and P. K. Newton. The N-vortex problem on a rotating sphere: II. heterogeneous platonic solid equilibria. *Proc. Roy. Soc. London Ser. A*, 462:3277–3299, 2006.

[40] R. Kidambi and P. K. Newton. Streamline topologies for integrable vortex motion on a sphere. *Physica D*, 140:95–125, 2000.

[41] M. Kirby. *Geometric Data Analysis: An Empirical Approach to Dimensionality Reduction*. Wiley-Interscience, 1 edition, 2001.

[42] V. C. Klema and A. J. Laub. The singular value decomposition: Computation and some applications. *IEEE Transactions on Automatic Control*, 25 (2):164–176, 1980.

[43] S. Kullback and R. A. Leibler. On information and sufficiency. *Ann. Math. Stats.*, 22:79–86, 1951.

[44] L. G. Kurakin. On nonlinear stability of the regular vortex systems on a sphere. *Chaos*, 14 (3):592–602, 2004.

[45] H. Lamb. *Hydrodynamics*. Cambridge University Press, 6 edition, 1932.

[46] F. Laurent-Polz, J. Montaldi, and M. Roberts. Stability of relative equilibria of point vortices on the sphere. *Preprint*, 0:1–30, 2006.

[47] J. C. Liao, D. N. Beal, G. V. Lauder, and M. S. Triantafyllou. The krmn gait: Novel body kinematics of rainbow trout swimming in a vortex street. *Oceanology*, 1:12–16, 2003.

[48] P. S. Marcus. Vortex dynamics in a zonal shearing flow. *J. Fluid Mech.*, 215:393–430, 1990.

[49] P. S. Marcus. Jupiter's great red spot and other vortices. *Ann. Rev. Astron. Astrophys.*, 31:523–573, 1993.

[50] P. S. Marcus. Prediction of global climate change on jupiter. *Letters to Nature*, 428:828–831, 2004.

[51] A. W. Maue. Zur stabilitot der karmanschen wirbelstrasse. *Z. Angew. Math. Mech.*, 20:129, 1940.

[52] V. V. Meleshko and H. Aref. *A bibliography of Vortex Dynamics 1858-1956*. available online, 2007.

[53] P. K. Newton. *The N-Vortex Problem: Analytical Techniques*. Applied Math. Sci., Springer-Verlag, 2001.

[54] P. K. Newton and G. Chamoun. On regular triangular vortex lattices. *USC preprint*, 2006.

[55] P. K. Newton and G. Chamoun. Construction of point vortex equilibria via brownian ratchets. *Proc. Roy. Soc. London Ser. A*, 463:1525–1540, 2007.

[56] P. K. Newton and G. Chamoun. Vortex lattice theory: Harnessing thermal fluctuations to produce patterns. *SIAM Review*, 2008 (in press).

[57] P. K. Newton and H. Shokraneh. The N-vortex problem on a rotating sphere: I. multi-frequency configurations. *Proc. Roy. Soc. London Ser. A*, 462:149–169, 2006.

[58] B. R. Noack and H. Eckelmann. A global stability analysis of the steady and periodic cylinder wake. *J. Fluid Mech.*, 270:297–330, 1994.

[59] B. R. Noack and H. Eckelmann. A low-dimensional galerkin method for the three-dimensional flow around a circular cylinder. *Phys. Fluids*, 6:124–143, 1994.

[60] C. C. Paige and M. A. Saunder. Towards a generalized singular value decomposition. *SIAM Journal on Numerical Analysis*, 18 (3):398–405, 1981.

[61] S. Pekarsky and J. E. Marsden. Point vortices on a sphere: Stability of relative equilibria. *J. Math. Phys.*, 39 (11):5894–5907, 1998.

[62] F. L. Ponta and H. Aref. The strouhal-reynolds number relationship for vortex streets. *Phys. Rev. Lett.*, 93:84501, 2004.

[63] F. L. Ponta and H. Aref. Vortex synchronization regions in shedding from an oscillating cylinder. *Phys. Fluids*, 17:011703, 2005.

[64] M. Provansal, C. Mathis, and L. Boyler. Benard-von kármán instability: Transient and forced regimes. *J. Fluid Mech.*, 182:1–22, 1987.

[65] A. Roshko. Experiments on the flow past a circular cylinder at very high reynolds number. *Journal of Fluid Mechanics*, 10:345–356, 1961.

[66] P. G. Saffman and J. C. Schatzman. Stability of a vortex street of finite vortices. *J. Fluid Mech.*, 117:171–185, 1982.

[67] C. E. Shannon. A mathematical theory of communication. *Bell. Sys. Tech. J.*, 27:379–423, 1948.

[68] P. R. Shukla, G. T. Birk, and R. Bingham. Vortex streets driven by sheared flow and applications to black aurora. *J. Geophys. Res. Lett.*, 22:671–674, 1985.

[69] M. A. Stremler. Relative equilibria of singly periodic point vortex arrays. *Phys. Fluids*, 15:3765–3775, 2003.

[70] L. N. Trefethen and D. Bau III. *Numerical Linear Algebra*. SIAM, Philidelphia, 1 edition, 1997.

[71] S. Umeyama. Least-squares estimation of transformation between two point patterns. *IEEE Transactions on Pattern Analysis and Machine Intelligence*, 4 (3):376–380, 1991.

[72] C. H. K. Williamson. Vortex dynamics in the cylinder wake. *Ann. Rev. Fluid Mech.*, 28:477–539, 1996.

[73] C. H. K. Williamson and A. Roshko. Vortex formation in the wake of an oscillating cylinder. *J Fluids Struct.*, 2:355–381, 1988.

[74] E. J. Yarmchuck, M. J. V. Gordon, and R. Packard. Observation of stationary vortex arrays in rotating superfluid helium. *Phys. Rev. Lett.*, 43:214–217, 1979.

[75] S. Yoden and M. Yamada. A numerical experiment on two-dimensional decaying turbulence on a rotating sphere. *J. Atmos. Sci.*, 50 (4):631–643, 15 Feb. 1993.

[76] A. Youssef and P. S. Marcus. The dynamics of jovian white ovals from formation to merger. *Icarus*, 162 (1):74–93, March 2003.

[77] A. Zebib. Stability of viscous flow past a circular cylinder. *J Engng Maths*, 21:155–165, 1987.

Appendices

Appendix A. Examples of Symmetric Lattices

Figures A.60, A.61 and A.62 are a compact catalogue of various configurations that possess symmetries in addition to and their solutions (which is listed in the captions).

(a) $N = 8$, hollow contour

(b) $N = 9$

(c) $N = 25$
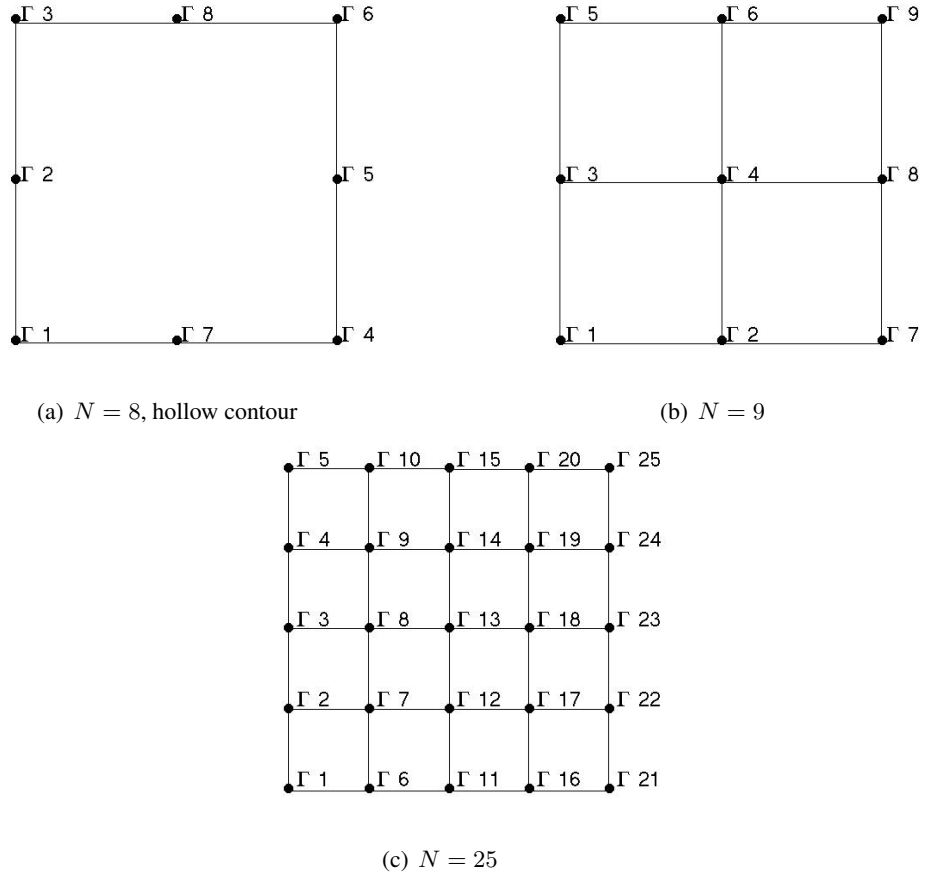
Figure A.60: Square lattices. Solutions are (a) null space of 1 with $\Gamma = (2, 1, 2, 2, 1, 2, 1, 1)^T$, (b) null space of two $\Gamma = \alpha(0, 1, 1, 0.2, 0, 1, 0, 1, 0)^T + \beta(1, 0, 0, -0.1, 1, 0, 1, 0, 1)^T$. (c) has null space of one with $\Gamma = (1, 76/327, 1, -76/327, 1, -76/327, -37/218, -69/295, -37/218, -76/327, 1, -69/295, 1, -69/295, 1, -76/327, 37/218, -69/295, -37/218, -76/327, 1, -76/327, 1, -76/327, 1)^T$. Fractions represent numerical approximations.
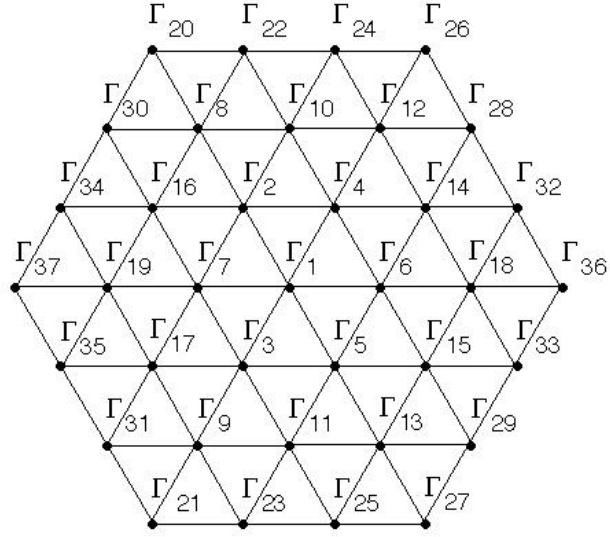
(a) $N = 37$, Triple Hexagon
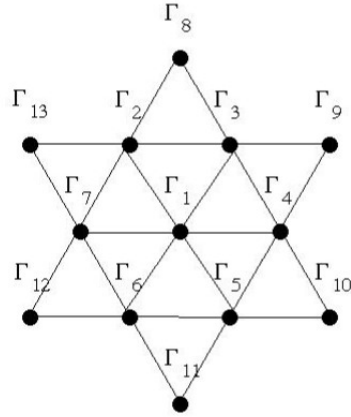
(b) $N = 13$, Star
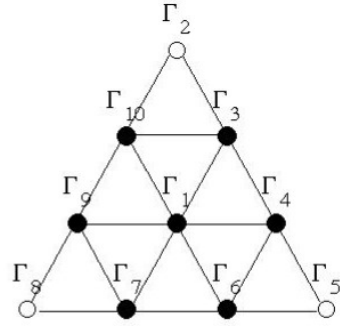
(c) $N = 10$, Triangle

Figure A.61: Triangular lattices: (a) null space of 1, solution is Γ = (-11/9, - 3/2, -3/2, -3/2, -3/2, -3/2, -3/2, -34/9, -34/9, 1, 1, -34/9, -34/9, 1, 1, 1, 1, -34/9, -34/9, 1, 1, -14/9, -14/9, -14/9, -14/9, 1, 1, -14/9, -14/9, -14/9, -14/9, -14/9, -14/9, -14/9, -14/9, 1, 1)^T, (b) null space of two, solution is $\Gamma = \alpha$(-6/7, 1, 1, 1, 1, 1, 1, 0, 0, 0, 0, 0, 0)^T + β(13/14, 0, 0, 0, 0, 0, 0, 1, 1, 1, 1, 1, 1)^T, (c) null space of 1, solution is Γ = (-6/7, 0, 1, 1, 0, 1, 1, 0, 1, 1)^T. Fractions represent numerical approximations.

(a) $N = 7$, Two branches

(b) $N = 10$, Three branches

(c) $N = 13$, Four branches

(d) $N = 16$, Five branches
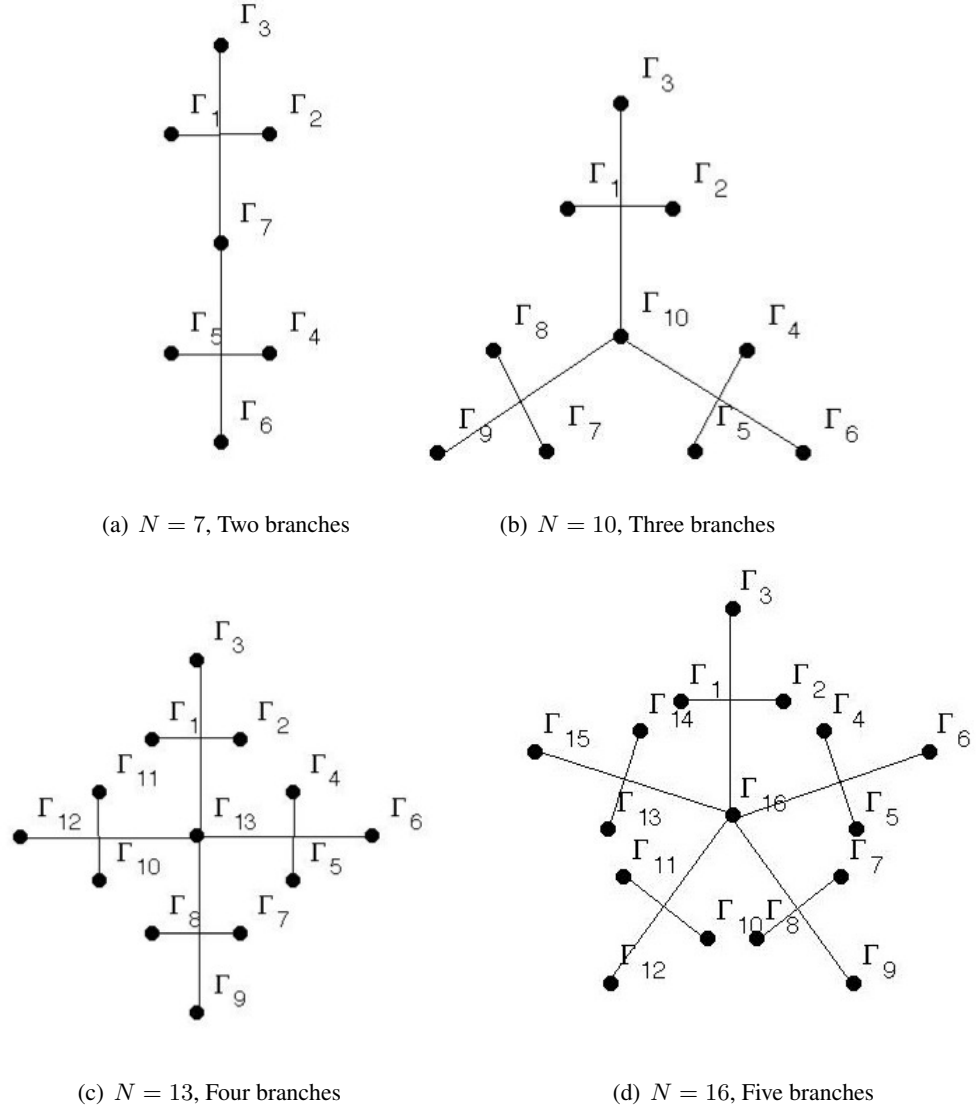
Figure A.62: Snowflake lattices. Characterized by concentric, rotational symmetry. The lattices above have a null space of one, with vortices that possess the same distance from the center having the same strength. (a) $\boldsymbol{\Gamma} \approx$ $(0.1517, 0.1517, -0.1572, 0.1517, 0.1517, -0.1572, -0.0787)^T$, (b) $\boldsymbol{\Gamma} \approx (0.1134, 0.1134, -0.0741, 0.1134, 0.1134,$ $-0.0741, 0.1134, 0.1134, -0.0741, -0.0973)^T$, (c) $\boldsymbol{\Gamma} \approx (0.0918, 0.0918, 0.0500, 0.0918, 0.0918, 0.0500, 0.0918,$ $0.0918, 0.0500, 0.0918, 0.0918, 0.0500, -0.0657)^T$, (d) $\boldsymbol{\Gamma} \approx (0.0265, 0.0265, 0.1341, 0.0265, 0.0265, 0.1341, 0.0265,$ $0.0265, 0.1341, 0.0265, 0.0265, 0.1341, 0.0265, 0.0265, 0.1341, 0.0640)^T$

Appendix B. Structure of the Configuration Matrix: Single Vortex Street

We now comment on the structure of the configuration matrix corresponding to single vortex streets on the sphere for the case of a single vortex street with 3 vortices per ring. The configuration matrix takes the following form

From the structure of the configuration matrix found in (5.108) for $n = 3$, one can readily conclude that $A\mathbf{\Gamma} = 0$ gives rise to a total of fifteen equations: six equations that link exactly one vortex in the northern ring to one in the southern ring and nine equations that are identically zero. This information can be represented pictorially as done in Figure B.63.

The number of filled vortices per ring is either 1 or 0 which means that one has 2 or 0 non-trivial entries in a given row of the configuration matrix A. In the case of 2 non-trivial entries, one entry is associated with a vortex from the northern hemisphere and the second is associated with a vortex from the southern hemisphere.

For vortex streets with $n > 3$ vortices per ring, two distinct patterns emerge in the configuration matrix: one pattern for n odd and another pattern for n even. These patterns share some properties. The first similarity is that if, in a given row of A, there are $m \leq n$ non-trivial entries associated with vortices from the northern hemisphere, there is an equal number of non-trivial entries associated with vortices from the southern hemisphere in that row. The second similarity

(a) 0/3 Filled, 9 eqs.   (b) 1/3 Filled, 6 eqs.
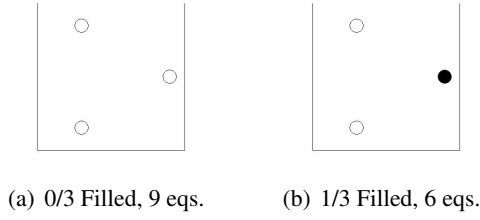
Figure B.63: Combinations found in the configuration matrix of a single Von Kármán Street on the Sphere with $n = 3$ vortices per ring. Image shows top view of one ring (either northern or southern). There are six equations in the configuration matrix with 0 non-trivial terms per ring, and another nine with 1 vortex from each ring a with non-trivial coefficient

(a) N=7 Allowed   (b) N=7 Not Allowed   (c) N=8 Allowed   (d) N=8 Not Allowed
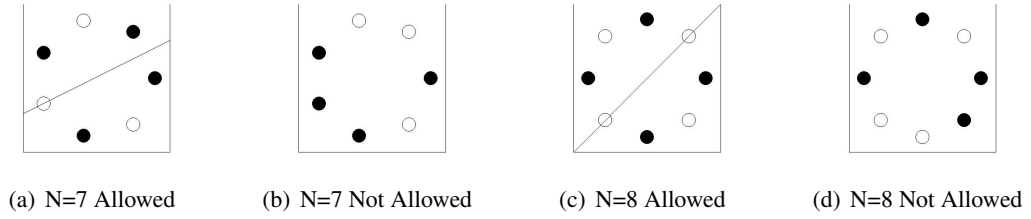
Figure B.64: Contrasting allowable and unallowable configurations for $N = [7, 8]$. Allowable configuration all have even symmetry with respect to a planar axis, while unallowable ones visibly do not have any symmetries.

is that if there are $m < n$ non-trivial entries in a given row of A associated with vortices from the northern hemisphere, the ordering of these entries must possess a certain symmetry. For example, consider the configuration matrix A associated with $n = 7$ and say that one row of A has 4 non-trivial entries associated with vortices from the northern hemisphere, these 4 entries can be ordered as shown in Figure B.64(a) but cannot appear in the order shown in Figure B.64(b).

B.1   Odd Number of Vortices per Ring

For $n \geq 5$, the number of vortices per ring corresponding to non-trivial entries in the configuration matrix is $(n - 2)$, $(n - 3)$ and $(n - n)$. For example, for $n = 9$, the number of filled vortices per ring is either 7, 6 or 0 as shown in Figure B.65, which means that one has 14, 12 or 0 non-trivial entries in a given row of the configuration matrix A. In the case of 14 non-trivial

Table B.4: Odd n Combination Distribution			
# Filled per ring	# Equations per combination	# of combinations	Total # of equations
$n-2$	$2n$	$(n-1)/2$	$n(n-1)$
$n-3$	$2n$	$(n-1)/2$	$n(n-1)$
$n-n$	n	1	n

entries, 7 entries are associated with vortices from the northern hemisphere and 7 are associated with vortices from the southern hemisphere – similarly in the case of 12 non-trivial entries. Rows for which the entries $A_{\cdot 1}$, $A_{\cdot 2}$, $A_{\cdot 4}$, $A_{\cdot 5}$, $A_{\cdot 7}$, $A_{\cdot 8}$ are non-trivial correspond to the vortices $[1, 2, 4, 5, 7, 8]$ being filled which is shown in Figure B.65(b). Note that the pattern of the configuration matrix is independent of the labeling of the point vortices. For example, one could choose to relabel vortices $[1, 2, 4, 5, 7, 8]$ as $[2, 3, 5, 6, 8, 9]$ or $[3, 4, 6, 7, 9, 1]$, that is, to rotating the label about the polar axis – this does not affect the pattern of the configuration matrix.

There are $(n-1)/2$ distinct combinations in the case of $(n-2)$ or $(n-3)$ filled vortices per ring. For example, when $n = 9$, there are $(9-1)/2 = 4$ different combinations that contain six filled vortices per ring as depicted in Figures B.65(b-e), which means that one has 4 distinct rows of A containing 12 non-trivial entries.

Each combination pattern containing either $n-2$ or $n-3$ filled vortices is present $2n$ times (note in the labeling of Figure B.65 that any pattern with 7 or 6 filled vortices is repeated $2(9) = 18$ times). Next, each non-trivial equation type in the configuration matrix is repeated exactly twice. This means that there are exactly two different equations containing non-trivial coefficients for, say, the case when [1,2,4,5,7,8] are filled vortices. Finally, there are n trivial equations present (i.e., $n-n$ filled vortices, or zero vectors in the configuration matrix). The generalized description is tabulated in B.65.

B.2 Even Number of Vortices per Ring

The pattern present for even n (with $n \geq 4$) is more elaborate. The possible number of vortices per ring with non-trivial entries in the configuration matrix are n, $(n-1)$, $(n-2)$ and $(n-4)$.

(a) 1/9, 9x   (b) 6/9, 18x   (c) 6/9, 18x   (d) 6/9, 18x

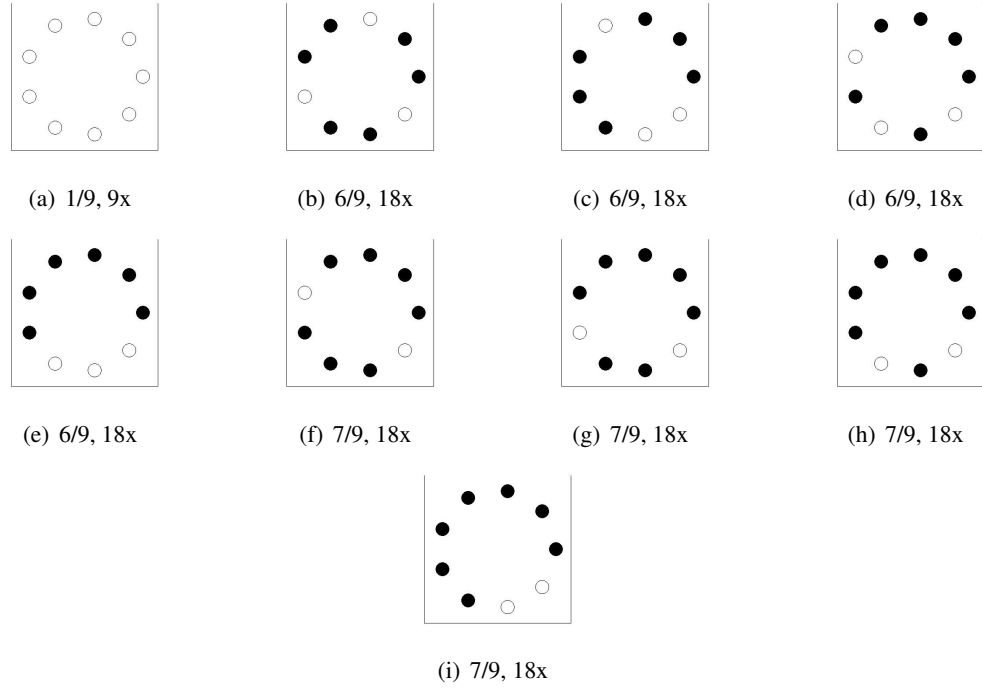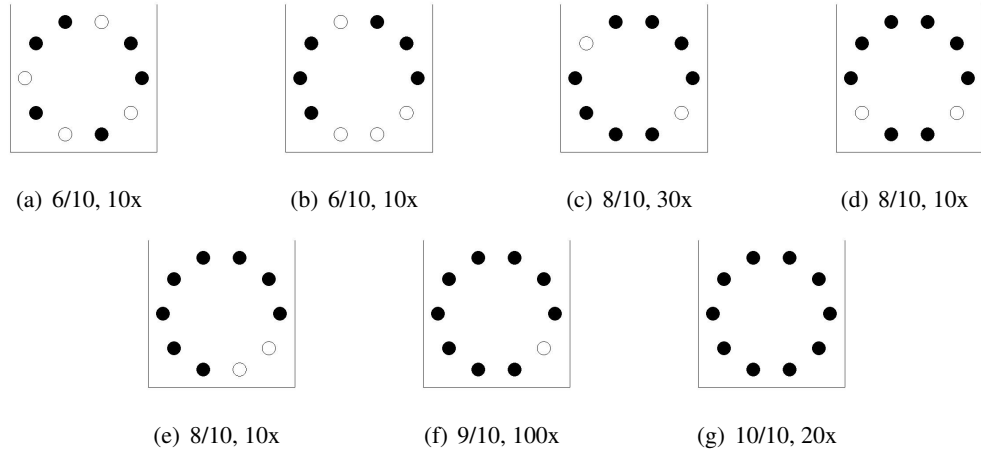(e) 6/9, 18x   (f) 7/9, 18x   (g) 7/9, 18x   (h) 7/9, 18x

(i) 7/9, 18x

Figure B.65: Combination types present in the configuration matrix for $n = 9$ vortices per ring. Number of filled vortices per ring are 7, 6 and 0. Each non-trivial combination type is present 18 times, in addition to 9 trivial ones.

For example, if $n = 10$, the number of filled vortices per ring is either 10, 9, 8 or 6. For the first case of n non-trivial entries per ring, there are $(\sum_{\alpha=1}^{(n/2)-1} 2\alpha)$ corresponding rows in the configuration that have this structure, and this applies to the cases $n \geq 4$. For example, in Figure B.66(g) when $n = 10$, there are 20 rows in the configuration matrix that contain 10 non-trivial entries per ring. Second, there are $(\sum_{\alpha=0}^{(n/2)-1} 4 + 8\alpha)$ rows with $n - 1$ filled vortices per ring, and this applies to the cases $n \geq 2$. For instance, in Figure B.66(f) when $n = 10$, there are 100 equations that contain 9 non-trivial entries from each ring. Third, there are $(\sum_{\alpha=0}^{(n/2)} (4\alpha - 2))$ rows in the configuration matrix with $n - 2$ non-trivial entries per ring, and this applies when $n \geq 2$. However, the difference between the $n - 2$ case and the previous ones is that there is only one unique kind of combination possible for n or $n - 1$ filled vortices, while there are more than one different combinations found for $n - 2$ (and $n - 4$) filled vortices, and the total number of rows containing $n - 2$ non-trivial entries per ring is distributed amongst the different possible combination types according to a second sub-pattern. Figures B.66(c-e) show three different

133

Table B.5: Even n Combination Distribution

#Filled	#Equations
n	$\sum_{\alpha=1}^{(n/2)-1} 2\alpha, n \geq 4$
$n-1$	$\sum_{\alpha=0}^{(n/2)-1} 4 + 8\alpha, n \geq 2$
$n-2$	$\sum_{\alpha=1}^{(n/2)} 4\alpha - 2, n \geq 2$
$n-4$	$\sum_{\alpha=1}^{(n/2)} 2\alpha - 2, n \geq 4$

(a) 6/10, 10x   (b) 6/10, 10x   (c) 8/10, 30x   (d) 8/10, 10x

(e) 8/10, 10x   (f) 9/10, 100x   (g) 10/10, 20x

Figure B.66: Combination types present for $N = 10$. Number of filled vortices per ring are $10, 9, 8$ and 6, repeated a total of $20, 100, 50$ and 20 times respectively.

types of combinations that have 8 filled vortices per ring, and these patterns are repeated in the configuration matrix 30, 10 and 10 times respectively, giving us a total of 50 rows in the configuration matrix that have 8 filled vortices per ring. Lastly, there are $\left(\sum_{\alpha=1}^{(n/2)}(2\alpha - 2)\right)$ rows that contain $n - 4$ non-trivial entries per ring, and this applies to the cases $n \geq 4$. Table B.2 contains the generalized description for even n.

Appendix C. Viscous Point Vortex Model

This thesis has dealt exclusively with invcisid point vortices. As a supplemental reference, we now describe the incompressible viscous point vortex model as a starting point for the investigation of viscous lattices. An expression for a viscous point vortex can be derived by looking at the Navier Stokes equations in cylindrical coordinates, where the velocity field $\mathbf{u}(r, t) = (u_r, u_\theta, u_z) \equiv (0, u_\theta, 0)$. We consider the Navier Stokes equation corresponding to θ the component, with the LHS and RHS of the equation being

$$
LHS = \frac{\partial u_\theta}{\partial t} + u_r \frac{\partial u_\theta}{\partial r} + \frac{u_\theta}{r} \frac{\partial u_\theta}{\partial \theta} + u_z \frac{\partial u_\theta}{\partial z} + \frac{u_r u_\theta}{r}, \tag{C.161}
$$

$$
RHS = \frac{1}{r} \frac{\partial p}{\partial \theta} + \nu \left(\frac{1}{r} \frac{\partial}{\partial r} \left(r \frac{\partial u_\theta}{\partial r} \right) + \frac{1}{r^2} \frac{\partial^2 u_\theta}{\partial \theta^2} + \frac{\partial^2 u_\theta}{\partial z^2} + \frac{2}{r^2} \frac{\partial u_r}{\partial \theta} - \frac{u_\theta}{r^2} \right) + f_\theta \tag{C.162}
$$

Assumptions made about the system include:

1. The flow is axisymmetric: $\partial/\partial\theta = \partial^2/\partial\theta^2 = 0$.

2. Two-dimensional: $\partial/\partial z = \partial^2/\partial z^2 = 0$ & $u_z = 0$.

3. No pressure gradient: $\partial p/\partial\theta = 0$.

4. No body forces: $f_\theta = 0$.

Plugging these assumptions into our the NV equation we get

$$\begin{aligned} LHS &= \frac{\partial u_\theta}{\partial t}, \\ RHS &= \nu \frac{1}{r}\frac{\partial}{\partial r}\left(r\frac{\partial u_\theta}{\partial r}\right). \end{aligned}$$

Therefore, our governing equation becomes

$$\frac{\partial u_\theta}{\partial t} = \nu \frac{1}{r}\frac{\partial}{\partial r}\left(r\frac{\partial u_\theta}{\partial r}\right). \tag{C.163}$$

The assigned boundary conditions for our problem are:

1. At $t = t_0$, the point vortex has the same velocity field as an inviscid point vortex: $u_\theta(r, t_0) = \Gamma/2\pi r$.

2. As $r \to \infty$, the inviscid point vortex resembles the inviscid point vortex $\forall t : u_\theta(r \to \infty, t) = \Gamma/2\pi r$.

3. The angular velocity at the center of the inviscid point vortex is zero: $u_\theta(0, t) = 0$.

Plugging the assumptions above into the continuity equation in cylindrical coordinates (see Equation (2.10)), we have

$$\begin{aligned} \nabla \cdot \mathbf{u} &\equiv 0 \\ &= \frac{1}{r}\frac{\partial}{\partial r}(ru_r) + \frac{1}{r}\frac{\partial u_\theta}{\partial \theta} + \frac{\partial u_z}{\partial z} \\ &= 0 + 0 + 0 \equiv 0. \end{aligned}$$

Note that this is also the heat equation in cylindrical coordinates. One of way solving this equation is by considering a similarity solution. We proceed by non-dimensionalizing the velocity in Equation (C.163) by defining

$$\hat{u} = u_\theta \frac{2\pi r}{\Gamma}. \tag{C.164}$$

With the chain rule, Equation (C.163) becomes

$$\frac{\partial \hat{u}}{\partial t} = \nu \frac{1}{r} \left(-\frac{1}{r} \frac{\partial \hat{u}}{\partial r} + \frac{\partial^2 \hat{u}}{\partial r^2} \right). \tag{C.165}$$

The boundary conditions in terms of the non-dimensional velocity are

1. $\hat{u}(r, t_0) = 1$,

2. $\hat{u}(r \to \infty, t) = 1$,

3. $\hat{u}(0, t) = 0$.

Defining the variable $\eta = \eta(r, t, \nu)$ as

$$\eta = \frac{r^2}{4\nu t}, \tag{C.166}$$

we can find a similarity solution $\hat{u}(\eta)$ when plugging Equation (C.166) into Equation (C.165)

$$\hat{u}''(\eta) + \hat{u}'(\eta) = 0. \tag{C.167}$$

Setting $t_0 = 0$, the new boundary conditions

1. $\hat{u}(\eta = 0) = 1$,

2. $\hat{u}(\eta \to \infty) = 0$,

Our solution becomes

$$\hat{u}(\eta) = 1 - e^{-\eta},$$

or

$$\hat{u}(r,t) = 1 - \exp\left(-\frac{r^2}{4\nu t},\right)$$

or

$$u_\theta(r,t) = \frac{\Gamma}{2\pi r}\left(1 - \exp\left(-\frac{r^2}{4\nu t}\right)\right). \tag{C.168}$$

The solution, therefore, coincides with a point vortex whose overall vorticity is preserved, but is advected outward away from the center of vorticity. The above construct for a visous point vortex contains radial symmetry reminiscent of the inviscid vortex model due to the face that there are no other sources of rotation in the flow. Introducing a second viscous vortex into the flow would break this symmetry, and make a clean formulation such as that in Equation (C.168) impossible. Therefore, in order to approximate viscous point vortex systems, restrictions on the inter-vortical viscous effects would have to be introduced. Although viscous vortex lattices will not be addressed in this thesis, the problem has been introduced and discussed briefly since it is an open topic worthy of notice and investigation.